

MEMS tunable infrared metamaterial and mechanical sensors

by

Qiugu Wang

A dissertation submitted to the graduate faculty
in partial fulfillment of the requirements for the degree of

DOCTOR OF PHILOSOPHY

Major: Electrical Engineering

Program of Study Committee:

Liang Dong, Major Professor

Meng Lu

Jaeyoun Kim

Timothy Bigelow

Jiming Song

The student author, whose presentation of the scholarship herein was approved by the program of study committee, is solely responsible for the content of this dissertation. The Graduate College will ensure this dissertation is globally accessible and will not permit alterations after a degree is conferred.

Iowa State University

Ames, Iowa

2017

Copyright © Qiugu Wang, 2017. All rights reserved.

TABLE OF CONTENTS

NOMENCLATURE	iv
ACKNOWLEDGEMENTS.....	v
ABSTRACT.....	vi
CHAPTER 1 GENERAL INTRODUCTION.....	1
1.1 Background	1
1.2 Introduction	3
1.2.1 Active Media Enabled Tunable Plasmonics	3
1.2.2 MEMS/NEMS Enabled Tunable Plasmonics	7
1.2.3 Graphene-Based MEMS Sensors.....	10
1.2.4 Nanotransfer Printing Technologies	14
1.3 Problem Statement	16
1.4 Thesis Organizations	19
1.5 References	21
CHAPTER 2 ELECTRICALLY TUNABLE QUASI-3D MUSHROOM PLASMONIC CRYSTAL	26
2.1 Abstract	26
2.2 Introduction	26
2.3 Methods and Experimental Details	29
2.4 Results and Discussion.....	32
2.5 Conclusions	38
2.6 Acknowledgment.....	38
2.7 References	39
CHAPTER 3 TUNABLE OPTICAL NANOANTENNAS INCORPORATING BOWTIE NANOANTENNA ARRAYS WITH STIMULI-RESPONSIVE POLYMER	44
3.1 Abstract	44
3.2 Introduction	45
3.3 Results and Discussion.....	46
3.4 Methods and Experimental Details	55
3.5 Conclusions	57
3.6 Acknowledgement.....	58
3.7 References	58
CHAPTER 4 NEMS-BASED INFRARED METAMATERIAL VIA TUNING NANOCANTILEVERS WITHIN COMPLEMENTARY SPLIT RING RESONATORS.....	63
4.1 Abstract	63
4.2 Introduction	63
4.3 Device Structure and Principle.....	65
4.4 Methods.....	66
4.5 Results and Discussion.....	68
4.6 Conclusions	81
4.7 Acknowledgement.....	81
4.8 References	81

CHAPTER 5 THERMO-MECHANICALLY TUNABLE ASYMMETRIC SPLIT RING RESONATORS FOR NEMS-BASED INFRARED METAMATERIALS	88
5.1 Abstract	88
5.2 Introduction	88
5.3 Methods	90
5.4 Results and Discussion	90
5.5 Conclusions	94
5.6 Acknowledgement	95
5.7 References	95
CHAPTER 6 GRAPHENE “MICRODRUMS” ON FREESTANDING PERFORATED THIN MEMBRANE FOR HIGH SENSITIVITY MEMS PRESSURE SENSOR	97
6.1 Abstract	97
6.2 Introduction	97
6.3 Results and Discussion	104
6.4 Methods and Experimental Details	112
6.5 Conclusions	115
6.6 Acknowledgement	115
6.7 References	116
CHAPTER 7 A MEMS FLOW SENSOR USING PERFORATED GRAPHENE MEMBRANE	122
7.1 Abstract	122
7.2 Introduction	122
7.3 Results and Discussion	123
7.4 Conclusion	127
7.5 References	127
CHAPTER 8 TAPE-BASED FLEXIBLE METALLIC AND DIELECTRIC NANPHOTONIC DEVICES AND METAMATERIALS	129
8.1 Abstract	129
8.2 Introduction	129
8.3 Methods	131
8.4 Results and Discussion	132
8.5 Conclusions	141
8.6 Acknowledgement	141
8.7 References	141
CHAPTER 9 CONCLUSIONS AND OUTLOOK	144
9.1 Conclusions	144
9.2 Outlook	146
APPENDIX LIST OF PEER REVIEWED JOURNALS	147

NOMENCLATURE

BNA	Bowtie Nanoantenna Array
CMOS	Complementary Metal-Oxide-Semiconductor
c-SRR	complementary Split Ring Resonator
CVD	Chemical Vapor Deposition
EM	ElectroMagnetic
FP	Fabry–Pérot
ITO	Indium Tin Oxide
LC	Liquid Crystal
LSPR	Localized Surface Plasmon Resonance
MEMS	MicroElectroMechanical Systems
NEMS	NanoElectroMechanical Systems
nTP	nanotransfer Printing
PDMS	Poly-dimethylsiloxane
RA	Rayleigh Anomaly
SAM	Self-Assembled Monolayer
SERS	Surface Enhanced Raman Spectroscopy
SEM	Scanning Electron Microscopy
SOI	Silicon On Insulator
SP	Surface Plasmon
SPP	Surface Plasmon Polariton
SRR	Split Ring Resonator
VPTT	Volume Phase Transition Temperature

ACKNOWLEDGEMENTS

It has been fortunate to meet so many loving people at Iowa State and I would like to thank all of the people who have supported me during my thesis work and beyond.

Most of all, I want to express my sincere gratitude to my advisor Professor Liang Dong for his constant guidance and encouragement. He is full of enthusiasm, ideas and inspirations. I am grateful for what I have learned both in research and personally, which are immeasurable values for me.

Thanks to all members of my thesis committee for the guidance and suggestions. Thanks to Professor Jiming Song for valuable discussions in simulations of tunable asymmetric split-ring resonator metamaterial. Thanks to Professor Meng Lu for insightful discussions on tapered-based metallic and dielectric nanophotonic devices. Thanks to Professors Jaeyoun Kim and Timothy Bigelow for discussing my thesis work and providing excellent feedback.

Thanks to Dr. Wai Leung in Microelectronics Research Center for his trainings on electron beam lithography and evaporator. It is a pleasure to work with a great group of fellow students: Dr. Depeng Mao, Dr. Huawei Jiang, Dr. Peng Liu, Zhen Xu, Yifei Wang, Yuncong Chen, Xinran Wang, Xuan Qiao, Yueyi Jiao, Junhao Zhu, Dr. Md Azahar Ali, Shawana Tabassum, and Seval Oren, who made the lab an enjoyable and inspiring environment. Thanks to Longju Liu for the helps in nanofabrications and Siming Yang for the helps in electromagnetic simulations.

I would like to acknowledge the funding support from the U.S. National Science Foundation under Grants # ECCS-0954765, ECCS-1711839 and the Plant Sciences Institute at Iowa State University.

Finally, I wish to thank my parents for their unconditional love and support during my twenty-two-year-long journey of study in school.

ABSTRACT

Sub-wavelength resonant structures open the path for fine controlling the near-field at the nanoscale dimension. They constitute into macroscopic “metamaterials” with macroscale properties such as transmission, reflection, and absorption being tailored to exhibit a particular electromagnetic response. The properties of the resonators are often fixed at the time of fabrication wherein the tunability is demanding to overcome fabrication tolerances and afford fast signal processing. Hybridizing dynamic components such as optically active medium into the device makes tunable devices. Microelectromechanical systems (MEMS) compatible integrated circuit fabrication process is a promising platform that can be merged with photonics or novel 2D materials. The prospect of enormous freedom in integrating nanophotonics, MEMS actuators and sensors, and microelectronics into a single platform has driven the rapid development of MEMS-based sensing devices. This thesis describes the design and development of four tunable plasmonic structures based on active media or MEMS, two graphene-based MEMS sensors and a novel tape-based cost-effective nanotransfer printing techniques.

First of all, we present two tunable plasmonic devices with the use of two active medium, which are electrically controlled liquid crystals and temperature-responsive hydrogels, respectively. By incorporating a nematic liquid crystal layer into quasi-3D mushroom plasmonic nanostructures and thanks to the unique coupling between surface plasmon polariton and Rayleigh anomaly, we have achieved the electrical tuning of the properties of plasmonic crystal at a low operating electric field. We also present another tunable plasmonic device with the capability to sense environmental temperature variations. The device is bowtie nanoantenna arrays coated with a submicron-thick, thermos-responsive hydrogel. The favorable scaling of

plasmonic dimers at the nanometer scale and ionic diffusion at the submicron scale is leveraged to achieve strong optical resonance and rapid hydrogel response, respectively.

Secondly, we present two MEMS -based tunable near-to-mid infrared metamaterials on a silicon-on-insulator wafer via electrically and thermally actuating the freestanding nanocantilevers. The two devices are developed on the basis of the same fabrication process and are easy-to-implement. The electrostatically driven metamaterial affords ultrahigh mechanical modulation (several tens of MHz) of an optical signal while the thermo-mechanically tunable metamaterial provides up to 90% optical signal modulation at a wavelength of 3.6 μm .

Next, we present MEMS graphene-based pressure and gas flow sensors realized by transferring a large area and few-layered graphene onto a suspended silicon nitride thin membrane perforated with micro-through-holes. Due to the increased strain in the through-holes, the pressure sensor exhibits a very high sensitivity outperformed than most existing MEMS-based pressure sensors using graphene, silicon, and carbon nanotubes. An air flow sensor is also demonstrated via patterning graphene sheets with flow-through microholes. The flow rate of the air is measured by converting the mechanical deflection of the membrane into the electrical readout due to the graphene piezoresistors.

Finally, we present a tape-based multifunctional nanotransfer printing process based on a simple stick-and-peel procedure. It affords fast production of large-area metallic and dielectric nanophotonic sensing devices and metamaterials using Scotch tape.

CHAPTER 1

GENERAL INTRODUCTION

1.1 Background

Controlling the properties of light at the sub-wavelength scale precision has been an intense subject over the past two decades. Plasmonics is such a branch of nanophotonics that explores the study and application of surface plasmon (SPs) bound to a metal surface over a dimension of much smaller than the wavelength of light. In essence, SPs are electromagnetic (EM) field coupled collective oscillations of free electrons in a metal. They squeeze light into a very tiny volume of charge density with spatial variation and generate extremely intense and concentrated optical fields. Hence, one key advantage of SPs is their capability of confining optical fields in sub-wavelength scale to overcome the diffraction limit of light. This has led to many applications in sub-diffraction limited imaging [1, 2] and integrated electro-opto circuits [3]. On the other hand, the huge enhancement of local optical fields is very useful in enhancing interactions between light and matters at the nanoscale and has found vast applications in biosensors [4, 5], surface enhanced Raman spectroscopy (SERS) [6], medicine (cancer therapy [7], drug delivery [8]), nanolasers [9, 10].

The properties of SPs are very sensitive to the geometrical shapes of nanostructures. Tremendous plasmonic structures with varied shapes are studied to achieve increasing confinement and enhancement of light, or peculiar optical phenomena. Among them, coupled nanoparticles [11, 12] and plasmonic metamaterials [13, 14] are most notable structures. The former often with dimer configuration provides coupled and thus extremely enhanced optical fields in the nanoscale gaps compared to the individual nanoparticle system while the latter made

of arrays of resonant elements and can be engineered to exhibit negative refractive index and to steer wavefronts of light.

However, plasmonic devices are not practical unless they can overcome fabrication limitations and tolerances and meet the increasing demand for strong and fast nonlinearities for switching light and precise control of the EM properties of devices at nanoscale footprints. Adding tunability to the passive plasmonic devices has the great promise to enhance the functionalities of the devices. To date, this tunability is mainly achieved through hybridizing nonlinear materials into the device or mechanically altering the shape of resonant elements [15, 16].

Microelectromechanical systems (MEMS), also named “microsystem technology” in Europe or “micromachines” in Japan is a microscopic technology, in general, referred to as miniaturized mechanical and electro-mechanical devices or structures made using microfabrication techniques. The MEMS devices are often made up of arrays of components with physical dimensions ranging from one micron to a hundred microns. Basically, there are four types of components for MEMS: microsensors, microactuators, microelectronics and microstructures. Among these components, microsensors and microactuators are defined as transducers that can convert energy from one to another. MEMS actuators usually convert electrical, optical, or thermal energy into mechanical motions while MEMS sensors are mostly designed for the conversion of mechanical signal to electric or optical signals. Some common MEMS actuating methods are electrostatic, piezoelectric, thermal types. Optical MEMS as an emerging field is of particular interest. Conventional optical MEMS are mainly used to steer and direct optical rays with applications in portable digital displays (e.g., digital micromirror device [16]), adaptive optics [18] (e.g., wavefront correction), and optical switches [19].

The potential of combining MEMS with near-field based plasmonics are gradually recognized with the advancement of nano/micro-fabrication techniques. In fact, both MEMS and plasmonic devices are often manufactured using modified complementary metal-oxide-semiconductor (CMOS) processes, which are the same batch fabrication techniques used to create integrated circuits (ICs) in industry and many commercial MEMS products are actually integrated and packaged together with ICs. There is enormous design freedom by merging plasmonics, MEMS sensors and actuators with microelectronics onto a single substrate.

Aside from the lithography-based CMOS processes for MEMS and plasmonics, nanotransfer printing (nTP) is another technique widely adopted to fabricate large-area and affordable plasmonic devices [20]. With nanolithographically created structures or stamp, the nTP utilizes chemically modified surfaces as release or glue layers to assist the transfer of nanopatterns. The nTP is cost-effective and high-throughput yet high-resolution technology, which allows the manufacturing of large-area nanopatterns.

1.2 Introduction

In last section, the concepts of tunable SPs and MEMS and the prospect of integrating the two technologies are introduced. This section will detail relevant work including: 1. Tunable plasmonics using active media, 2. Tunable plasmonics using MEMS or nanoelectromechanical systems (NEMS) technologies, 3. Graphene-based MEMS sensors, 4. Nanotransfer printing technologies.

1.2.1 Active Media Enabled Tunable Plasmonics

Here active media are defined as the materials that in response to an external stimulus (i.e., electrical field, heat, light, chemical compounds, etc.) their optical properties are variable and controllable. By hybridizing these functional materials into the plasmonic nanostructures, it

is possible to realize real-time control of the plasmonic properties. To date, commonly used materials are liquid crystals (LCs) [21], semiconductor [22], phase-change media [23] (i.e., vanadium dioxide, gallium), hydrogels [24] etc. In the following, LCs and hydrogels based devices will be the main topics of this section due to their versatile driven methods and wide application range.

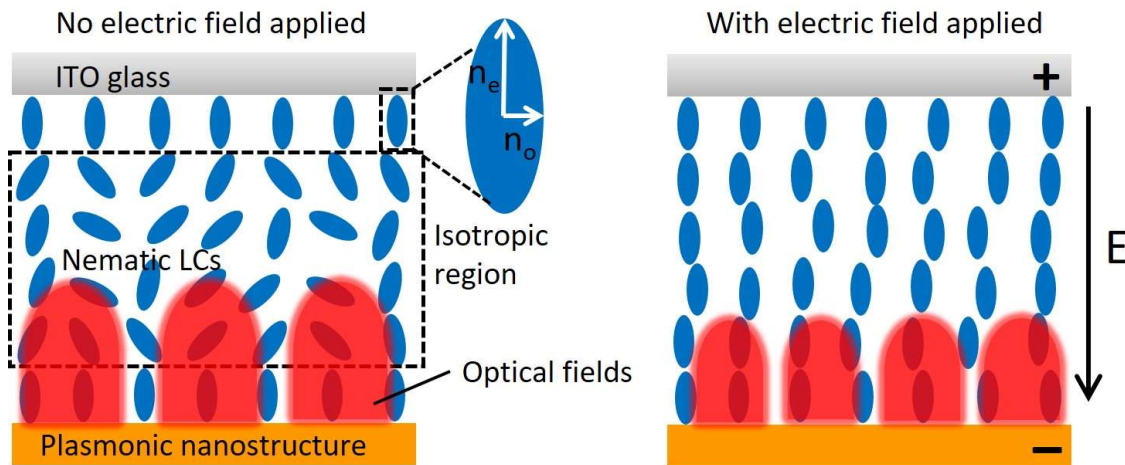


Figure 1.1 A schematic configuration of tuning near-field properties of plasmonic nanostructures via external electric field. The LCs are birefringent and uniaxial materials with extraordinary refractive index (n_e) and ordinary refractive index (n_o). The reorientation of LCs molecules caused by external electric field tunes the refractive index and influence the optical fields surrounding the plasmonic structures.

LCs are well-known for their applications in electronic display technologies. The most common LC phase is the nematic, which in its phase the rod-shape molecules has no positional order but are in long-range directional order along their long axes. There are a variety of ways to drive the phase of LCs. For example, all nematic LCs will eventually transit from anisotropic into isotropic states after ambient temperature increases to a certain point. This phase transition leads to the macroscopic optical property variations of LCs (i.e., refractive index). Take the 6CHBT LCs for example, in its initial phase, they are birefringent with extraordinary refractive index of 1.71 and ordinary refractive index of 1.53 [25], but are isotropic with effective

refractive index of 1.59 at the temperature of 33 °C. Thus, the ambient refractive index variation causes SP resonance shifts if LCs are infiltrated into the plasmonic nanostructures. In addition to the temperature stimulus, the nematic LCs can also be easily aligned by applying an external magnetic or electric field. Fig. 1.1 schematically presents a configuration of LCs based plasmonic structure with electrically controllable optical properties. LCs are sandwiched between the top electrode (e.g., indium tin oxide (ITO) glass) and bottom metallic nanostructure. The surface of the two electrode surfaces are often pre-treated with mechanical method or saline to anchor the LCs molecules near the electrodes. When an external electric field is applied, the long axis of LC molecules in those isotropic regions tend to align along the direction of the electric field which in turn tunes the near-field properties of the nanostructure.

Because many LCs have relative low phase transition temperatures (6CB: 29 °C; EBBA: 77 °C, used for industrial LC display) and response relaxation time is in the order of millisecond, LCs are effective and affordable materials for controlling plasmonic devices if ambient temperatures and speed of operations are not critical issues.

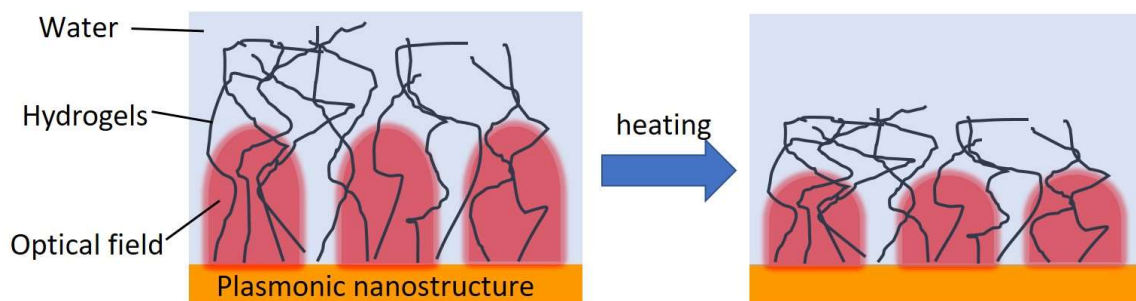


Figure 1.2 Schematic of the temperature-responsive hydrogels on plasmonic nanostructures. In reaction to a temperature increase, hydrogels undergo volumetric changes from swollen to collapsed state. Their refractive index increases as they collapsed and influences the near-field of plasmonic structures.

Stimuli-hydrogels are well-known in autonomous microfluidics playing the role of both sensors and actuators [26, 27]. The hydrogels are crosslinked polymers usually working in

aqueous environment with the ability to absorb and expel water and they undergo abrupt volumetric changes in response to various environmental stimuli (e.g., temperature, pH, glucose, light, electric field, etc). Take temperature-responsive hydrogels for example, their wetting behaviors below and above the volume phase transition temperature (VPTT) (~ 32 °C for most hydrogels) are totally opposite. As shown in Fig. 1.2, the hydrogels are initially in swollen state (i.e., absorb water; large volume) at room temperature but becoming collapsed (i.e., repel water; smaller volume) as the temperature is beyond the VPTT. These reversible volumetric variations lead to the refractive index changes of the hydrogels. Hence, hydrogels can be used to convert various stimuli signals into optical signals by utilizing the exceptional refractive index sensing capability from a plasmonic nanostructure.

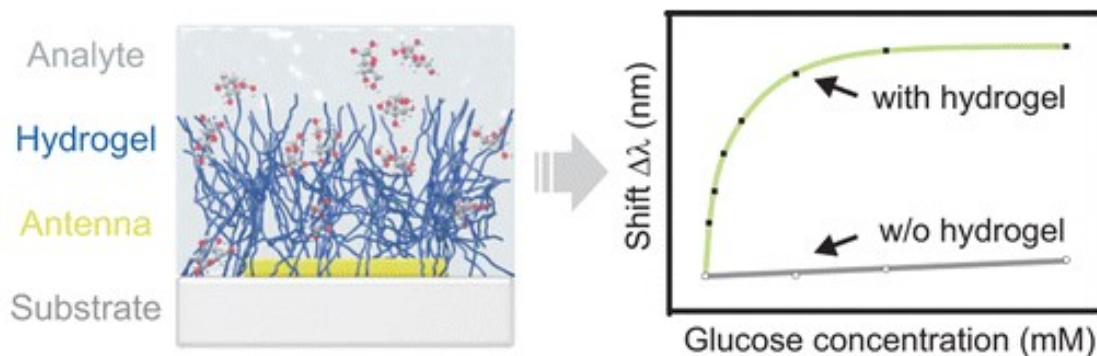


Figure 1.3 Hydrogel coated plasmonic antenna for noninvasive glucose sensing [28].

Fig. 1.3 presents a plasmonic antenna coated with a boronic acid functionalized hydrogel which is highly specific to glucose and large molecules [28]. The hydrogel films reversibly swell in the presence of glucose and blocks the large size protein from the plasmonic sensing range. It thus allows for low glucose concentration measurement in the physiological millimolar range.

Due to the ‘smart’ feature, the hydrogels have been applied in a diverse field, such as drug delivery, diagnostics, tissue engineering and smart optical systems, as well as biosensors, MEMS, coatings and textiles [27].

1.2.2 MEMS/NEMS Enabled Tunable Plasmonics

In addition to the use of active media to control the optical properties of nanostructures, as mentioned in Section 1.1, MEMS or NEMS is very suitable and promising platform for mechanically tuning plasmonic structures because of the enormous freedom of the integration with current IC batch fabrication techniques. The thermal, MEMS actuator, electrostatic actuating methods are commonly used techniques. Earlier tunable metamaterials devices operate at THz range with feature size of tens of micrometers as these devices are relatively easy to fabricate and tune.

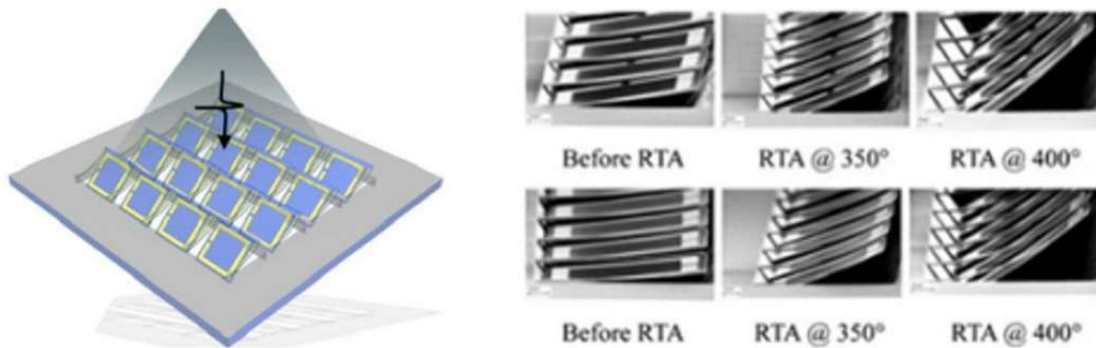


Figure 1.4 THz reconfigurable planar split ring resonator arrays on bimaterial cantilevers. The resonator arrays bent out of plane in response to a thermal stimulus [29].

Fig. 1.4 exhibits a first demonstration of thermally reconfigurable split ring resonator (SRR) metamaterial device working at THz [29]. The SRRs are sitting on a bimorph actuator consisting of gold and silicon nitride bilayer materials. Because of the different thermal expansion coefficient, thermal stimulus causes the deflection of the bimorph and tilts SRR arrays and thus modulates the transmission/reflection properties of the metamaterial.

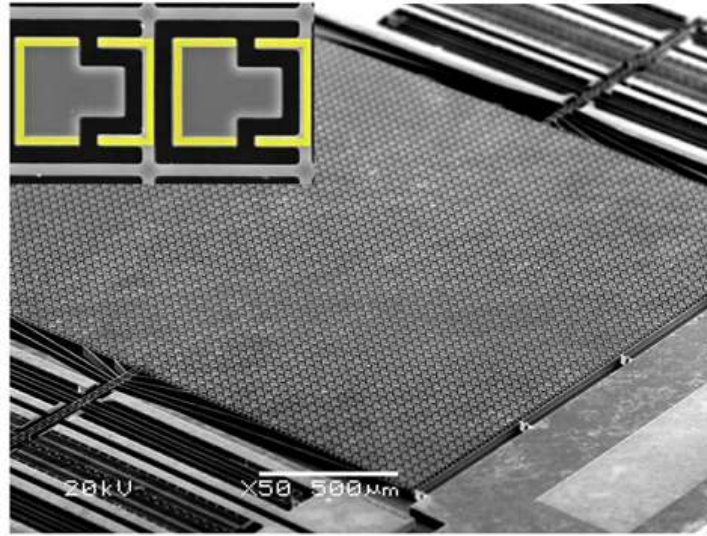


Figure 1.5 THz switchable magnetic metamaterials using combo-drive actuators. The resonant element consists of two semi-square split ring (Marked as yellow lines in the figure). The left one is fixed to the substrate while the right one is laterally movable controlled by the combo-drive actuator [30].

Another way to tune EM properties of metamaterials is to take the advantage of existing MEMS actuators, such as combo-drive actuators as shown in Fig. 1.5. The metamaterial working at 2 THz made of arrays paired semi-square SRR with one anchored and another movable controlled by the integrated MEMS combo-drive [30]. Thus, it allows precise control of the lateral gap between the two semi-square SRR and therefore, their coupling strength. The described tuning method can switch the effective permittivity of the metamaterials from negative to positive providing an exceptional large tunability. However, due to the large size MEMS combo-drive, it is hard to further reduce the metamaterial structure to shrink the working wavelength.

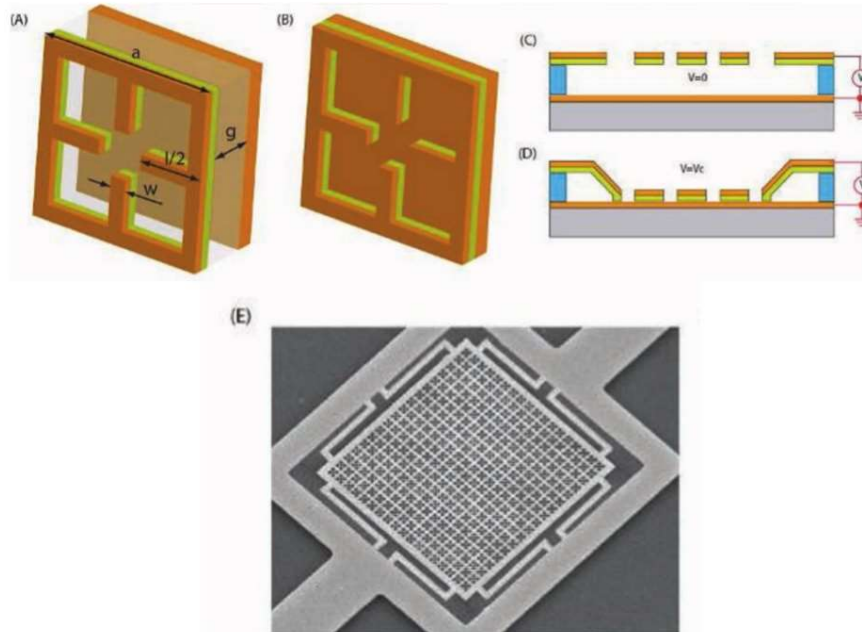


Figure 1.6 Mid-infrared electrical force enabled tunable metamaterial. The metamaterials are nanopatterned diaphragm ($100 \times 100 \mu\text{m}^2$) suspended over a grounding plane with a separation of $1.2 \mu\text{m}$ [31].

In order to scale down the working wavelength of the metamaterial device while retaining a compactness structure, main challenges are effective modulation schemes to tune the optical properties of the device. One of the schemes that enables the device to work at infrared even optical regime with high contrast switching is electrostatic force actuated diaphragm-based metamaterial device. Fig. 1.6 schematically exhibits the configuration of such a device that the nanopatterned membrane are suspended over a grounding substrate with a separation of $1.2 \mu\text{m}$ [31]. Upon an electric field is applied between the top metamaterial membrane and bottom grounding plane, electrostatic force drives the metamaterial downward and the reflection spectrum is greatly modulated due to the coupling of metamaterial and bottom reflecting layer. A modulation depth of 56% is attained at the wavelength of $6.2 \mu\text{m}$ when the top metamaterials is snapped down as shown in Fig. 1.6(b). However, to drive macroscopic displacement of the large area membrane, the mechanical modulation frequency of the device is $\sim 30 \text{ kHz}$.

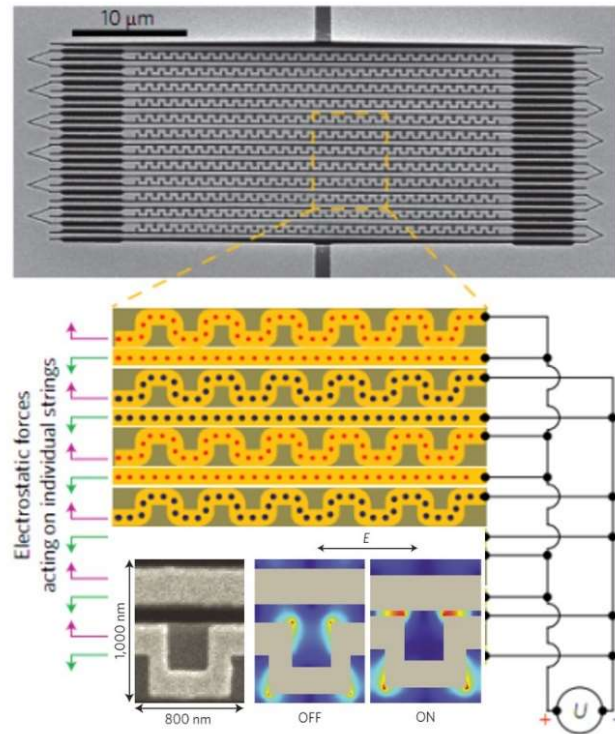


Figure 1.7 Near-infrared electrically tunable metamaterials with mechanical modulation frequency up to 1.3 MHz. The metamaterial consists of pairs of parallel microstrings. A DC voltage is applied between neighboring metal strings to control their gap distance [32].

Another scheme to achieve much higher mechanical modulation frequency is to reduce the size of the actuating unit. Fig. 1.7 shows an electrically tunable metamaterial device consisting of pairs of parallel microstrings [32]. By applying a voltage between the neighboring metallic strings, electrostatic forces will change the distance between the strings, and thus modulate the optical fields confined between the strings. At the wavelength of 1.3 μm , a maximal modulation depth is measured to be 8% with an applied voltage of 3 V. Although this is much smaller than 56% from diaphragm based metamaterial device, the mechanical modulation depth reaches 1.3 MHz benefited from the picogram weighted microstrings.

1.2.3 Graphene-Based MEMS Sensors

Graphene is a two-dimensional (2D) atomic thick (~ 0.345 nm) material with hexagonal lattice made of carbon atoms. It exhibits fast electron mobility in excess of $15000 \text{ cm}^2 \cdot \text{V}^{-1} \cdot \text{s}^{-1}$ at room temperature and is the strongest material ever tested with an intrinsic tensile strength of 130.5 GPa and a Young's modulus of 1 TPa.

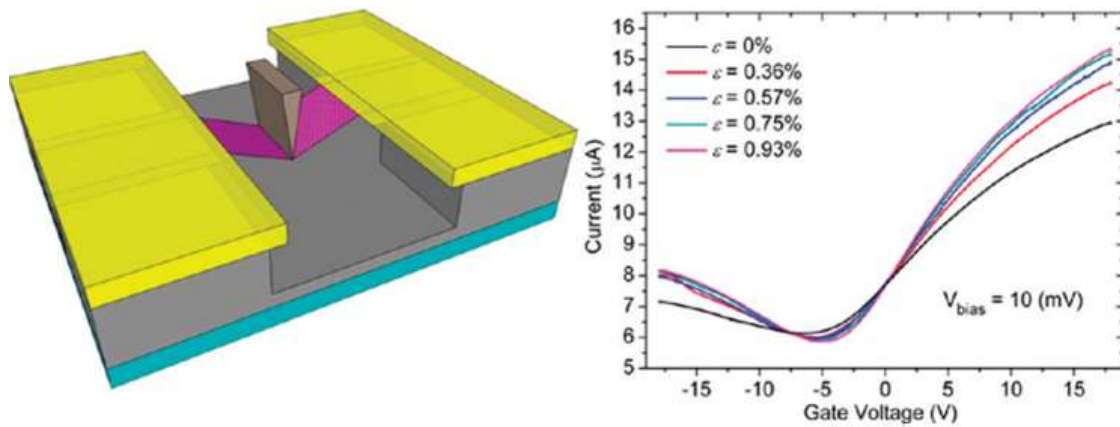


Figure 1.8 In situ nanoindentation experiments performed on suspended graphene ribbon (purple color) devices to measure electrical resistance while introducing homogenous tensile strain [32].

In addition to its excellent mechanical and electrical properties, impermeability for gases and ultra-strong adhesion to many materials (e.g., SiO_2) makes graphene very suitable for pressurized MEMS applications. There has been intensive work reporting the graphene based piezoresistive sensing devices. For example, the work in Fig. 1.8 studies the electro-mechanical coupling in graphene through in-situ nanoindentation experiments by applying a uniaxial tensile strain [33]. It is found that the resistance has increased is $\sim 2\%$ with 1% strain. The extracted gauge factor of graphene piezoresistor is 1.9 which is close to the theoretical prediction of 2.4.

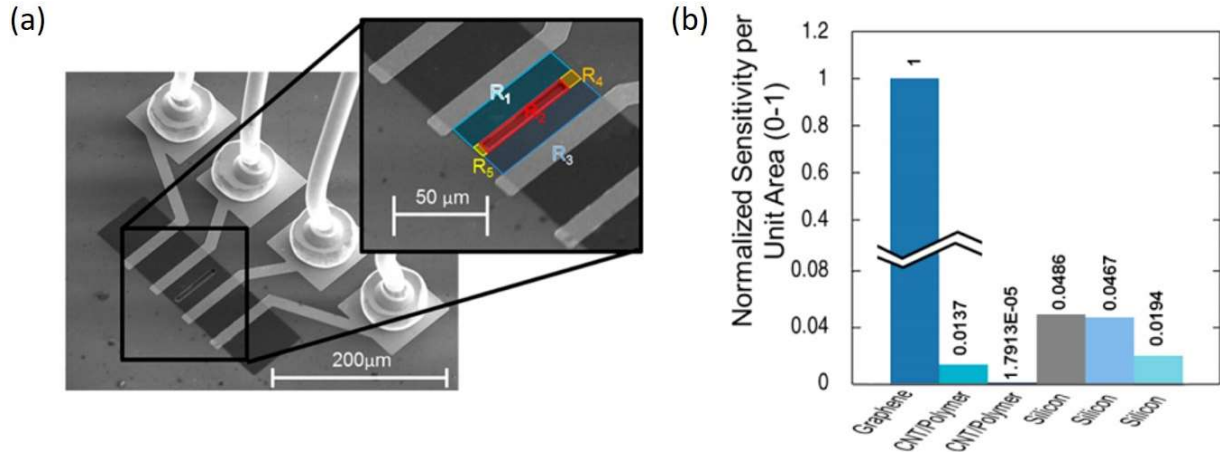


Figure 1.9 (a) A wire bonded graphene pressure sensor. A part of graphene is suspended over a rectangular cavity with an area of $6 \times 64 \mu\text{m}^2$. (b) Normalized sensitivity per unit area compared to carbon nanotube and silicon based sensors [34].

However, at present only several graphene based piezoresistive pressure sensors have been developed. Fig. 1.9 presents the study of a piezoresistive pressure sensing properties of suspended graphene membranes [34]. The membrane is sitting on a SiO_2 substrate etched with a square cavity. Thus, with the graphene suspended over the cavity, when the cavity is filled with argon, the pressure difference inside and outside the cavity causes the deflection of the graphene membrane and turns into the electrical readout. The sensitivity per unit area of the sensor is orders of magnitude higher than conventional silicon and nanotube based pressure sensors. The results also show that suspended graphene membrane exhibits a strain gauge independent of crystallographic orientation allowing for aggressive size scalability.

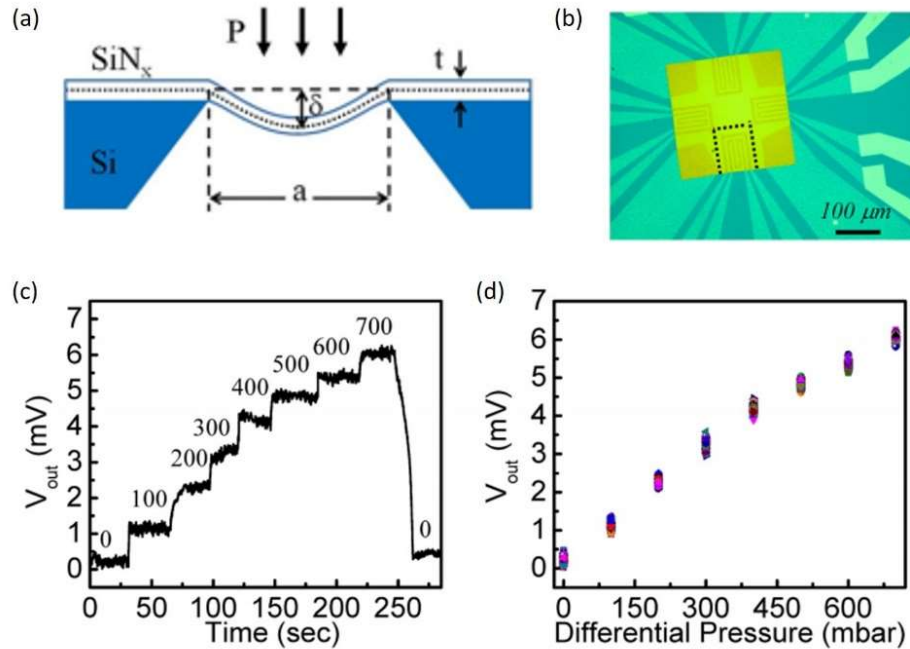


Figure 1.10 (a) Schematic of a MEMS pressure sensor with graphene meander on suspended silicon nitride (SiN_x) membrane. (b) The photograph of the device. The square SiN_x is $280 \mu\text{m}$ wide and graphene is located within the regions (dashed area) with highest tensile strain. (c) Dynamic electrical readout versus time with differential pressure increasing from 0 to 700 mbar. (d) Electrical readout versus differential pressure [35].

Chemical vapor deposition (CVD) has allowed large-area uniform growth of graphene sheets on various substrates [36, 37]. With the advent of transferring techniques, graphene has the promise to be merged into micromachined MEMS sensors and actuators. Fig. 1.10 exhibits the monolithic integration of graphene into suspended silicon nitride (SiN_x) membrane [35]. The CVD grown graphene is first transferred onto SiN_x membrane suspended over a micromachined silicon base. To increase the effective length and resistance, graphene sheet is patterned into meander shape. Strain is applied on graphene meander through the deflection of the SiN_x membrane when applying a differential pressure. The device exhibits a high performance with the observation of a 0.4% resistance change in response to a differential pressure change of 600

mbar. A good linear response is seen in Fig. 1.10(d) with the pressure detection limit ~ 100 mbar.

1.2.4 Nanotransfer Printing Technologies

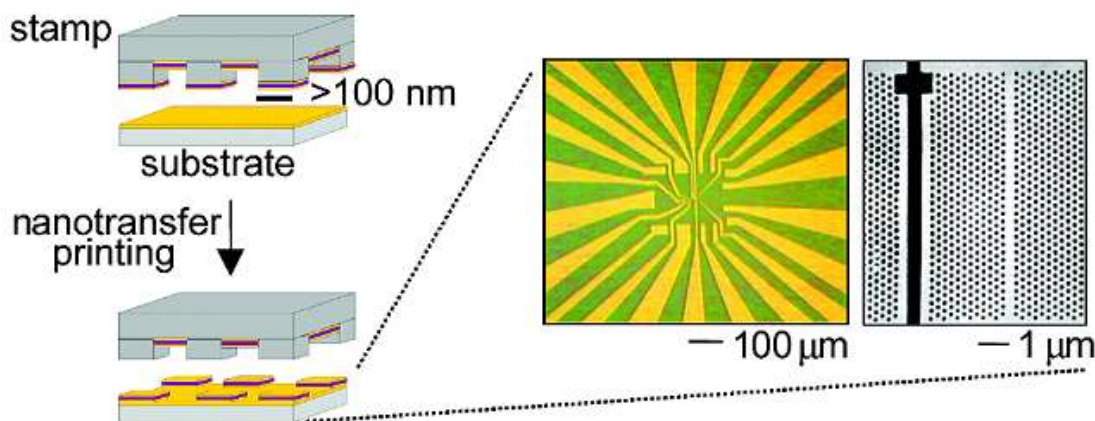


Figure 1.11 A nanoimprint technique to transfer of material from relief nanofeatures on a stamp to a substrate. The presented process uses self-assembled monolayer chemical as covalent glues and release layers [38].

The nTP process transfers a metal pattern from the template, usually made of silicon or poly-dimethylsiloxane (PDMS), to a backing layer through physical contact. It uses interfacial chemistries to modify the bonding strength between the two different surfaces. Fig. 1.11 presents a nTP process with the use of self-assembled monolayer (SAM) chemical to print gold nanopatterns from a PDMS substrate onto silicon substrate [38]. As we know, many metal, such as gold or silver, naturally do not adhere to silicon or PDMS substrates which requires the surface treatment on silicon wafer in order to transfer gold nanopatterns. The chemical modification process is briefly as follow: first, silicon wafer is soaked in a mixture of distilled water, H_2O_2 , and HCl to generate surface hydroxyl (-OH) groups; second, a vapor deposit of SAM (3-mercaptopropyltrimethoxysilane) on the silicon wafer allows the co-condensation of the methoxy groups with the hydroxyl groups on the surface; last, the PDMS stamp with gold

nanopattern will adhere to the silicon wafer due to the formation of sulfur-gold bonds when the stamp is brought into physical contact with the wafer.

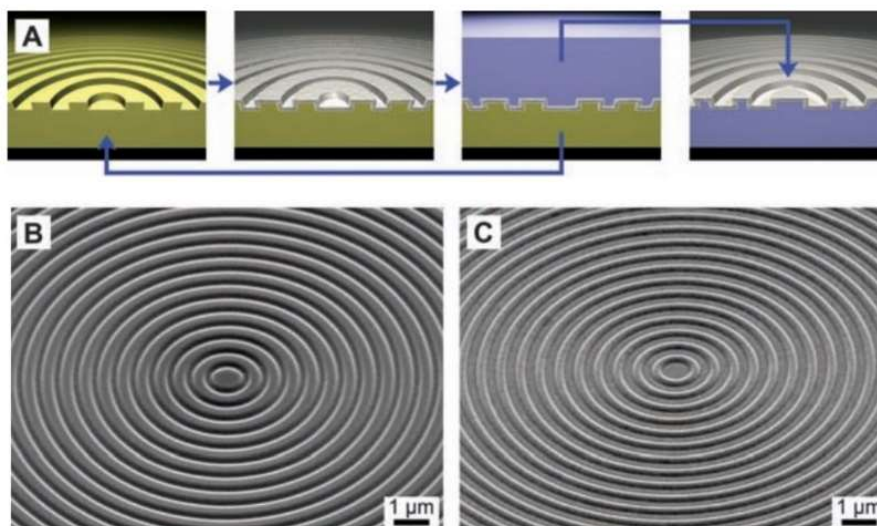


Figure 1.12 Template stripping technique to generate ultrasmooth nanopatterned metal. (a) Stripping process of silver circular concentric grooves from silicon wafer. (b), (c) SEM images of the device at glancing incidence [39].

Template stripping technique is another nTP process without the need of SAM. It is very straightforward in directly peeling off the metal from silicon or PDMS using a much adhesive substrate, such as adhesive tape, epoxy. Fig. 1.12 presents the use of such template stripping method to create ultrasmooth metallic nanopatterns [39]. In nanoimprint techniques, patterned polymeric stamp deposited with metal often induces serious surface roughness. Stamps with other materials suffer from low efficiency due to an additional etching process to release the metal pattern. This template stripping simply makes use of poor adhesion and good wettability of noble metals on silicon. Basically, the silicon wafer is first patterned, coated with silver and a thick layer of epoxy. The silver patterns can be ultraflat due to its good wettability on silicon. Because the silver does not adhere to silicon but is very much adhesive to epoxy, the epoxy-

metal bilayer can then be directly peeled off from the substrate. The patterned structure on epoxy substrate will be ultraflat with a surface roughness mainly determined by the wafer stamp.

1.3 Problem Statement

So far, we have discussed tunable optical sensors based on active media and MEMS methods, graphene based MEMS sensors and nTP technologies for low-cost nanofabrications. The main challenges are sensitivity improvement, cost reduction, increased functionalities, and the fusion of above technologies. Take MEMS-based tunable optical devices for example, the challenges are the development of efficient and new actuating mechanism at nanoscale, fast modulation speed, low power consumption and the integration with IC platform. It is impossible to discuss the challenges solely without considering their applications. Depending on the feature of each optical or MEMS sensor, challenges and approaches will be discussed separately from the application perspective.

1.3.1 Liquid Crystal based Tunable Plasmonics

In general, the resonance wavelength shift and modulation amplitude are two measures of LCs based plasmonic devices. However, it is hard to achieve the best of them simultaneously. For example, regarding LC display applications wherein high contrast switching is necessary, V-shape metamaterials are proposed to have a modulation amplitude $\sim 82\%$ although the device exhibits nearly zero resonance shift [40]. To achieve better refractive index sensing ability, a larger resonance shift up to 24 nm is obtained using plasmonic nanorods with large anisotropic optical properties but only showing a 4% modulation amplitude [41]. In the meantime, another rarely mentioned characterization for electronic devices is the power consumption. Most of existing electrical LCs based plasmonic devices using LSPR modes are in the range of 2-5 V/ μm for the applied electric field. However, some SPP based plasmonic devices are demanding a weaker value around 1.5 V/ μm . The key to lower the operating electric field is reducing the

degree of reorientation of LCs molecules which means smaller refractive index changes. My work will design such a new LCs alignment method while to sense the small refractive variation, we adopt quasi-3D nanostructure wherein its strongly coupled plasmonic mode is sensitive to the reorientation of LCs molecules.

1.3.2 Stimuli-responsive Hydrogels Based Tunable Plasmonics

Among many hydrogels-based tunable optical devices, nonlithographically made nanoparticles often exhibit relatively poor control over uniformity, i.e., their shape and size and thus lead to broadband resonance. Lithographically nanopatterns are also reported but the structures are mainly isolated nanoparticles unable to achieve high field enhancement which limits their sensitivity and tuning range. In contrast to individual nanoparticles, the excitation of SPs within the nanoscale air gap (less than 20 nm) in the coupled plasmonic nanoparticles greatly enhances of optical fields. This effect is useful for various applications in enhancing light-matter interactions, such as second harmonic generation, fluorescence enhancement and spaser. Our work studies the use of bowtie nanoantenna arrays (BNAs) with a tip-to-tip separation of 20 nm coated with temperature-responsive hydrogel. The intrinsically high field enhancement in the nanoscale gap is leveraged to achieve a more sensitive temperature-responsive device.

1.3.3 MEMS Based Tunable Metamaterials and Graphene Sensors

The MEMS technology based tunable metamaterials using thermally actuated bimorph beams or in-plane electrostatic comb-drive usually have relatively large size of resonant element which limits their optical resonance wavelength and mechanical modulation frequency. For example, although the metal diaphragm patterned with diffractive nanohole gratings can work in visible wavelength with a switch contrast of 61%, they exhibit modulation frequencies only at tens of kilohertz due to large mass hundred microns membrane [31]. To increase the mechanical

modulation frequency, multiple parallel pairs of metallic microstrings were driven using electrostatic forces to control nanoscale strip displacements at a rate of 1.6 MHz [32]. Despite these efforts, modulating EM properties of metamaterials at a rate of several tens of MHz into the near-infrared wavelength region remains very challenging.

Our work will design a compact and easy-to-implement tunable metamaterial, in which the nanoscale freestanding cantilevers provides a mechanical modulation frequency up to 32 MHz to modulate an optical signal at the wavelength of 2.1 μm . In addition, based on the same process scheme, a thermomechanically tunable asymmetric SRR metamaterial is also proposed to generate more than 90% optical signal modulation at the wavelength of 3.6 μm .

It is also promising to merge graphene with micromachining technology, however, there are only a few MEMS-based graphene pressure sensors as listed in Section 1.2.3. By carefully designing the micromachined membrane to optimize strain on graphene sheets, it is promising to realize ultrahigh sensitivity graphene based pressure sensor device. Our work developed high sensitivity graphene based pressure sensor via using the freestanding perforated thin membrane to significant enhance the areal strain of graphene. On the basis of the high sensitivity graphene piezoresistive pressures sensor, we also developed an air flow sensor to provide high velocity measurement with a high sensitivity.

1.3.4 Tape Based Nanotransfer Printing

As discussed in Introduction, the nTP is a cost-effective approach to fabricate large-area nanostructures. The adhesive tapes, often used to exfoliate graphene or single-layer MoS_2 , are also included in many nTP processes primarily as an intermediate transfer media. For example, the thermal adhesive tapes have been used for transferring nanotube transistors from a quartz substrate to plastic substrates [42]. This process utilizes the dramatic decrease in adhesion

strength of the tape at a high temperature and allows the nanotubes to be detached from the tape and adhered onto the receiver substrates.

On the other hand, adhesive tape itself can be a direct transfer media and the final architecture of the devices. To date, only one work is reported to have transferred the aluminum nanohole arrays onto the tape [43]. There is no systematical study to fully exploit the potential of the tape based nTP process for cost-effective fabrications of nanostructures. Our work focuses on the systematic development of a multifunctional nTP tape based technique to enable fast production of multiple optical nanodevices both on the tape and unconventional substrates.

1.4 Thesis Organizations

The following chapters are an accumulation of four published journal papers, two conference papers, one paper in preparation of which I am the primary author.

Chapter 2 describes the electrical tuning of optical properties of a quasi-3D mushroom plasmonic nanostructure using nematic LCs. The current design greatly reduces the operating electric field with a good switching contrast and resonance shift. The device may have applications in LCs display, sensing, and complex optical signal processing. The paper titled “Electrically Tunable Quasi-3-D Mushroom Plasmonic Crystal” is published in *Journal of Lightwave Technology*, **34** (9), 2175-2181 (2016).

Chapter 3 describes a temperature sensing device that incorporates optical nanobowtie structure and temperature-responsive hydrogels. The study suggests applications in environmental-sensitive plasmonic devices via integrating coupled plasmonic nanostructures and environmental-responsive materials. The paper titled “Tunable Optical Nanoantennas Incorporating Bowtie Nanoantenna Arrays with Stimuli-Responsive Polymer” is published in *Scientific Report*, **5**, 1567 (2015).

Chapter 4 reports on a NEMS enabled infrared tunable metamaterial that exhibits an ultrahigh mechanical modulation frequency for infrared signal modulation. The study may find many applications in optical modulators, infrared sensors, and transformation optics. The paper titled “NEMS-based Infrared Metamaterial via Tuning Nanocantilevers within Complementary Split Ring Resonators” is published in *Journal of Microelectromechanical Systems*, doi: 10.1109/JMEMS.2017.2746688 (2017).

Chapter 5 describes an easy-to-implement thermo-mechanically tunable metamaterial that provides 90% signal modulation at infrared wavelength. The study may find applications in thermal sensing, spectral filters, switches, and many other tunable photonic devices. The paper titled “Thermo-mechanically Tunable Asymmetric Split Ring Resonators for NEMS-based Infrared Metamaterials” is published in 17th International Conference on Nanotechnology (IEEE NANO 2017).

Chapter 6 describes a graphene-based MEMS pressure sensor. The measured sensitivity outperforms many other existing graphene based counterpart sensors. The paper titled “Graphene “Microdrums” on Freestanding Perforated Thin Membrane for High Sensitivity MEMS Pressure Sensor” is published in *Nanoscale*, **8** (14), 7663-7671 (2016).

Chapter 7 describes a graphene-based MEMS flow sensor. The perforated graphene sheet flows air and converts the mechanical signal of membrane deflection into electrical signal via the graphene piezoresistors. The paper is in preparation.

Chapter 8 describes a multifunctional nTP method based on a simple stick-and-peel procedure that enables fast production of multiple optical nanodevices using Scotch tape. The study suggests applications in wearable and highly flexible nanophotonic devices for biochemical sensing, imaging and optical emission applications. The paper titled “Tape-based

Flexible Metallic and Dielectric Photonic Devices and Metamaterials” is published in The 17th International Conference on Nanotechnology (IEEE NANO 2017).

1.5 References

- [1] Fang, N., Lee, H., Sun, C. & Zhang, X. Sub-diffraction-limited optical imaging with a silver superlens. *Science* **308**, 534-537, doi:10.1126/science.1108759 (2005).
- [2] Smolyaninov, II, Hung, Y. J. & Davis, C. C. Magnifying superlens in the visible frequency range. *Science* **315**, 1699-1701, doi:10.1126/science.1138746 (2007).
- [3] Haffner, C. *et al.* All-plasmonic Mach-Zehnder modulator enabling optical high-speed communication at the microscale. *Nature Photonics* **9**, 525-528, doi:10.1038/Nphoton.2015.127 (2015).
- [4] Anker, J. N. *et al.* Biosensing with plasmonic nanosensors. *Nature Materials* **7**, 442-453, doi:10.1038/nmat2162 (2008).
- [5] Brolo, A. G. Plasmonics for future biosensors. *Nature Photonics* **6**, 709-713, doi:10.1038/nphoton.2012.266 (2012).
- [6] Willets, K. A. & Van Duyne, R. P. Localized surface plasmon resonance spectroscopy and sensing. *Annual Review Of Physical Chemistry* **58**, 267-297, doi:10.1146/annurev.physchem.58.032806.104607 (2007).
- [7] El-Sayed, I. H., Huang, X. H. & El-Sayed, M. A. Surface plasmon resonance scattering and absorption of anti-EGFR antibody conjugated gold nanoparticles in cancer diagnostics: Applications in oral cancer. *Nano Letters* **5**, 829-834, doi:10.1021/nl050074e (2005).
- [8] Myszka, D. G. & Rich, R. L. Implementing surface plasmon resonance biosensors in drug discovery. *Pharm Sci Technolo Today* **3**, 310-317, 2000).

- [9] Noginov, M. A. *et al.* Demonstration of a spaser-based nanolaser. *Nature* **460**, 1110-1112, doi:10.1038/nature08318 (2009).
- [10] Oulton, R. F. *et al.* Plasmon lasers at deep subwavelength scale. *Nature* **461**, 629-632, doi:10.1038/nature08364 (2009).
- [11] Zhou, W. *et al.* Lasing action in strongly coupled plasmonic nanocavity arrays. *Nature Nanotechnology* **8**, 506-511, doi:10.1038/nnano.2013.99 (2013).
- [12] Kim, S. *et al.* High-harmonic generation by resonant plasmon field enhancement. *Nature* **453**, 757-760, doi:10.1038/nature07012 (2008).
- [13] Smith, D. R., Pendry, J. B. & Wiltshire, M. C. Metamaterials and negative refractive index. *Science* **305**, 788-792, doi:10.1126/science.1096796 (2004).
- [14] Shalaev, V. M. Optical negative-index metamaterials. *Nature Photonics* **1**, 41-48, doi:10.1038/nphoton.2006.49 (2007).
- [15] Zheludev, N. I. & Kivshar, Y. S. From metamaterials to metadevices. *Nature Materials* **11**, 917-924, doi:10.1038/NMAT3431 (2012).
- [16] Zheludev, N. I. & Plum, E. Reconfigurable nanomechanical photonic metamaterials. *Nature Nanotechnology* **11**, 16-22, doi:10.1038/Nnano.2015.302 (2016).
- [17] Xie, H. K., Pan, Y. T. & Fedder, G. K. A CMOS-MEMS mirror with curled-hinge comb drives. *Journal Of Microelectromechanical Systems* **12**, 450-457, doi:10.1109/Jmems.2003.815839 (2003).
- [18] Zhang, Y. H., Poonja, S. & Roorda, A. MEMS-based adaptive optics scanning laser ophthalmoscopy. *Optics Letters* **31**, 1268-1270, doi:10.1364/Ol.31.001268 (2006).
- [19] De Dobbelaere, P., Falta, K., Fan, L., Gloeckner, S. & Patra, S. Digital MEMS for optical switching. *Ieee Communications Magazine* **40**, 88-95, doi: 10.1109/35.989763 (2002).

- [20] Chanda, D. *et al.* Large-area flexible 3D optical negative index metamaterial formed by nanotransfer printing. *Nature Nanotechnology* **6**, 402-407, doi:10.1038/Nnano.2011.82 (2011).
- [21] Kossyrev, P. A. *et al.* Electric field tuning of plasmonic response of nanodot array in liquid crystal matrix. *Nano Letters* **5**, 1978-1981, doi:10.1021/nl0513535 (2005).
- [22] Buonsanti, R., Llordes, A., Aloni, S., Helms, B. A. & Milliron, D. J. Tunable infrared absorption and visible transparency of colloidal aluminum-doped zinc oxide nanocrystals. *Nano Letters* **11**, 4706-4710, doi:10.1021/nl203030f (2011).
- [23] Sweatlock, L. A. & Diest, K. Vanadium dioxide based plasmonic modulators. *Optics Express* **20**, 8700-8709, doi:10.1364/oe.20.008700 (2012).
- [24] Kuang, M., Wang, D. Y. & Mohwald, H. Fabrication of thermoresponsive plasmonic microspheres with long-term stability from hydrogel spheres. *Advanced Functional Materials* **15**, 1611-1616, doi:10.1002/adfm.200500141 (2005).
- [25] Baran, J. W., Raszewski, Z., Dabrowski, R., Kedzierski, J. & Rutkowska, J. Some Physical-Properties of Mesogenic "4-(Trans-4'-Normal-Alkylcyclohexyl) Isothiocyanatobenzenes. *Molecular Crystals And Liquid Crystals* **123**, 237-245, 1985).
- [26] Dong, L. & Jiang, H. Autonomous microfluidics with stimuli-responsive hydrogels. *Soft Matter* **3**, 1223-1230, doi:10.1039/b706563a (2007).
- [27] Stuart, M. A. C. *et al.* Emerging applications of stimuli-responsive polymer materials. *Nature Materials* **9**, 101-113, doi:10.1038/NMAT2614 (2010).
- [28] Mesch, M., Zhang, C. J., Braun, P. V. & Giessen, H. Functionalized Hydrogel on Plasmonic Nanoantennas for Noninvasive Glucose Sensing. *Acs Photonics* **2**, 475-480, doi:10.1021/acsp Photonics.5b00004 (2015).

- [29] Tao, H. *et al.* Reconfigurable Terahertz Metamaterials. *Physical Review Letters* **103**, 147401, doi:10.1103/Physrevlett.103.147401 (2009).
- [30] Zhu, W. M. *et al.* Switchable Magnetic Metamaterials Using Micromachining Processes. *Advanced Materials* **23**, 1792-1796, doi:10.1002/adma.201004341 (2011).
- [31] Liu, X. L. & Padilla, W. J. Dynamic Manipulation of Infrared Radiation with MEMS Metamaterials. *Advanced Optical Materials* **1**, 559-562, doi:10.1002/adom.201300163 (2013).
- [32] Ou, J. Y., Plum, E., Zhang, J. F. & Zheludev, N. I. An electromechanically reconfigurable plasmonic metamaterial operating in the near-infrared. *Nature Nanotechnology* **8**, 252-255, doi:10.1038/nnano.2013.25 (2013).
- [33] Huang, M. Y., Pascal, T. A., Kim, H., Goddard, W. A. & Greer, J. R. Electronic-Mechanical Coupling in Graphene from in situ Nanoindentation Experiments and Multiscale Atomistic Simulations. *Nano Letters* **11**, 1241-1246, doi:10.1021/nl104227t (2011).
- [34] Smith, A. D. *et al.* Electromechanical Piezoresistive Sensing in Suspended Graphene Membranes. *Nano Letters* **13**, 3237-3242, doi:10.1021/nl401352k (2013).
- [35] Zhu, S. E., Ghatkesar, M. K., Zhang, C. & Janssen, G. C. A. M. Graphene based piezoresistive pressure sensor. *Applied Physics Letters* **102**, doi:10.1063/1.4802799 (2013).
- [36] Reina, A. *et al.* Large Area, Few-Layer Graphene Films on Arbitrary Substrates by Chemical Vapor Deposition. *Nano Letters* **9**, 30-35, doi:10.1021/nl801827v (2009).
- [37] Suk, J. W. *et al.* Transfer of CVD-Grown Monolayer Graphene onto Arbitrary Substrates. *Acs Nano* **5**, 6916-6924, doi:10.1021/nn201207c (2011).

- [38] Loo, Y. L., Willett, R. L., Baldwin, K. W. & Rogers, J. A. Interfacial chemistries for nanoscale transfer printing. *Journal Of The American Chemical Society* **124**, 7654-7655, (2002).
- [39] Nagpal, P., Lindquist, N. C., Oh, S. H. & Norris, D. J. Ultrasmooth patterned metals for plasmonics and metamaterials. *Science* **325**, 594-597, doi:10.1126/science.1174655 (2009).
- [40] Buchnev, O., Ou, J. Y., Kaczmarek, M., Zheludev, N. I. & Fedotov, V. A. Electro-optical control in a plasmonic metamaterial hybridised with a liquid-crystal cell. *Optics Express* **21**, 1633-1638, doi:10.1364/OE.21.001633 (2013).
- [41] Chu, K. C., Chao, C. Y., Chen, Y. F., Wu, Y. C. & Chen, C. C. Electrically controlled surface plasmon resonance frequency of gold nanorods. *Applied Physics Letters* **89**, doi: 10.1063/1.2335812 (2006).
- [42] Lee, C. H., Kim, D. R. & Zheng, X. L. Fabricating nanowire devices on diverse substrates by simple transfer-printing methods. *Proceedings Of The National Academy Of Sciences Of The United States Of Ame* **107**, 9950-9955, doi:10.1073/pnas.0914031107 (2010).
- [43] Barrios, C. A. & Canalejas-Tejero, V. Compact discs as versatile cost-effective substrates for releasable nanopatterned aluminium films. *Nanoscale* **7**, 3435-3439, doi:10.1039/c4nr06271j (2015).

CHAPTER 2

ELECTRICALLY TUNABLE QUASI-3D MUSHROOM PLASMONIC CRYSTAL

A paper published in *Journal of Lightwave Technology*

Qiugu Wang, Weikun Han, Peng Liu, and Liang Dong

2.1 Abstract

This paper reports an electrically tunable plasmonic crystal incorporating a nematic liquid crystal (LC) layer on the top surface of quasi-3D mushroom plasmonic nanostructures. The presented plasmonic crystal is formed by an array of polymeric mushroom nanoposts with gold disks at the top and perforated nanoholes in a gold thin film at the bottom. The coupling between surface plasmon polariton (SPP) and Rayleigh anomaly (RA) is observed in experiments with quasi-3D plasmonic crystals, and verified by simulations. The coupled SPP-RA resonance mode has its electric field vector prominently normal to the surface of the plasmonic nanostructures, and extends into the surrounding medium. This feature makes the coupled resonance sensitive to molecular reorientation in LC, and thus, is useful for designing index modulation-based tunable plasmonic crystal devices. Therefore, by applying external voltages across the LC layer, the SPP-RA resonance mode shows a redshift of 8 nm with a 35% change in amplitude.

2.2 Introduction

Nanoplasmonics provides an efficient way to control and manipulate light in the vicinity of a metal surface below the diffraction limit through the excitation of surface plasmons (SPs) [1]. The Rayleigh anomaly (RA) is a non-resonant diffraction effect caused by light diffracting into an extended propagating in-plane wave [2-4]. This differs from surface plasmon polariton (SPP) resonance, which decays much more quickly away from the metal surface [4-6]. As has been previously studied, the coupling of RA and SPP [5, 6], and the coupling between RA and

localized surface plasmon resonance (LSPR) [7-12] in planar plasmonic nanostructures, can lead to a stronger and narrower hybridized resonance. Quasi-3D plasmonic crystals are structured by an array of metal nanodisk-nanohole pairs physically separated by dielectric nanoposts or air-filled nanowells [13-20]. Because of the nanoscale distance between the nanodisks and nanoholes, a variety of hybridized SP modes exist with higher electric-field enhancement than the sole SPPs found in conventional planar nanohole-based plasmonic structures [13-18]. Quasi-3D plasmonic crystals can support RA, SPP and LSPR and can be fabricated in large-area arrays using soft nanoimprinting lithography, giving unique plasmonic performance [13-20]. For example, the coupled LSPR-RA resonance resulted in a high figure of merit value approaching the theoretical limit for standard propagating SP sensors [12].

Quasi-3D plasmonic nanostructures have demonstrated their capabilities in SP resonance-based sensing [13-16], imaging [13], and surface enhanced Raman spectroscopy [19, 20] in the visible and near-infrared wavelengths. However, if their optical responses are dynamically tunable, the quasi-3D nanostructures will become more useful when adapting to different applications. Therefore, we are interested in realizing an unexplored capability to actively control plasmonic fields in quasi-3D plasmonic crystals. A simple way to tune their optical response is to modulate their refractive index environment by using an active medium. Among many possible active media, liquid crystal (LC) has been extensively used to tune properties of many optical structures and devices [21-31] due to its large and controllable optical anisotropy and its versatile driving methods, including electrical [21-25], optical [26, 27], thermal [28, 29], and acoustic tuning [30].

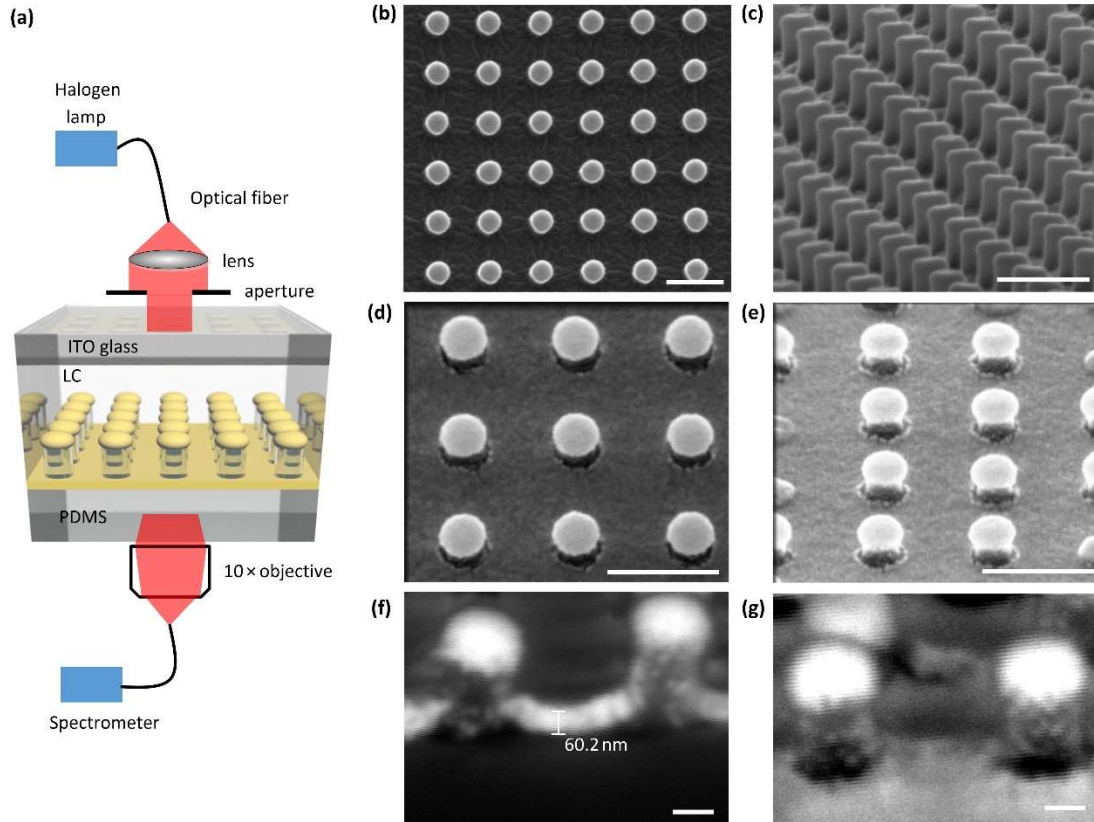


Figure 2.1 (a) Schematic of an electrically tunable quasi-3D plasmonic crystal in a transmission measurement setup. (b, c) Top and 45° side-view scanning electron microscopy (SEM) images for an array of polymer nanoposts without Au nanodisks (lattice constant $a = 500$ nm, post diameter = 190 nm, post height = 300 nm). (d, e) 10° and 30° tilt view of the nanopost array deposited with a Ti/Au thin film. Scale bars in (b-e) represent 500 nm. (f, g) Cross section and close-up of the nanoposts deposited with a Ti/Au thin film. Scale bars in (f) and (g) represent 100 nm.

In this paper, we demonstrate an electrically tunable quasi-3D plasmonic crystal using a thin layer of nematic LCs (Fig. 2.1(a)). This plasmonic nanostructure is formed by a periodic array of mushroom nanoposts with Au disks and nanoholes perforated in an Au thin film at the bottom (Figs. 2.1(b)-(e)). A shallow LC cell is created between the Au thin layer and a transparent conducting glass. We show that the introduction of the LCs allows for a redshift of an SPP mode excited at the Au disks to couple to the RA at the perforated Au film. The characteristic SPP-RA resonance field is predominately normal to the nanostructured surface and

penetrates into the surrounding LC, thus making the resonance sensitive to reorientation of LC molecules. By applying an electric field applied across the LC cell of $0.55 \text{ V}/\mu\text{m}$, an 8 nm resonance shift with a 35% change in amplitude for the SPP-RA mode is observed.

2.3 Methods and Experimental Details

To fabricate the proposed tunable quasi-3D plasmonic crystal, we first utilize soft lithography-based replica molding process to form a polymer nanopost array made of polydimethyl-siloxane (PDMS) elastomer. In this step, a silicon template is used as a solid master mold containing a square array of nanoposts. The master mold is silanized with (tridecafluoro-1, 1, 2, 2-tetrahydrooctyl)-1-trichlorosilane (T2492-KG, United Chemical Technologies) in a desiccator under active vacuum for 20 min. Then, an h-PDMS precursor solution is prepared by mixing poly (7-8% vinylmethyl-siloxane)- (dimethylsiloxane) (Gelest # VDT-731), (1, 3, 5, 7-tetravinyl-1, 3, 5, 7-tetramethylcyclotetrasiloxane) (Gelest # SIT7900.0), platinum catalyst Xylene (Gelest # SIP6831.2) and poly (25-30% methylhydro-siloxane)- (dimethylsiloxane) (Gelest # HMS-301) at the weight ratio of 3.4: 0.1: 0.05: 1. Air bubbles are removed from the mixture in a degassing chamber for 10 min, followed by spin-coating of the mixture onto the silicon mold at 1000 rpm for 40 sec and curing at $70 \text{ }^\circ\text{C}$ for 10 min. Subsequently, an s-PDMS precursor solution is prepared by mixing Sylgard 184 (Dow Corning, USA) and curing agent at the weight ratio of 10: 1 and degassing in a vacuum desiccator for 20 min. The s-PDMS mixture is then poured onto the top surface of the h-PDMS and cured on a hotplate at $65 \text{ }^\circ\text{C}$ for 2 hr. After that, the PDMS slab containing a square array of nanoholes is peeled from the silicon mold.

To form an array of polymer nanoposts shown in Fig. 2.1(c), the PDMS nanoholes obtained in the last step are used as a soft mold. This soft mold is treated with saline, coated with

h-PDMS, and poured over with s-PDMS using the exactly same procedures as those used to make the soft mold. After that, the PDMS slab containing a square array of nanoposts is peeled from the soft mold. The obtained nanoposts have the period of 500 nm, the post diameter of 190 nm, and the post height of 300 nm. Finally, a 5 nm thick titanium (Ti) adhesion layer and a 60 nm thick Au layer are deposited on the whole surface of the device by using e-beam evaporation.

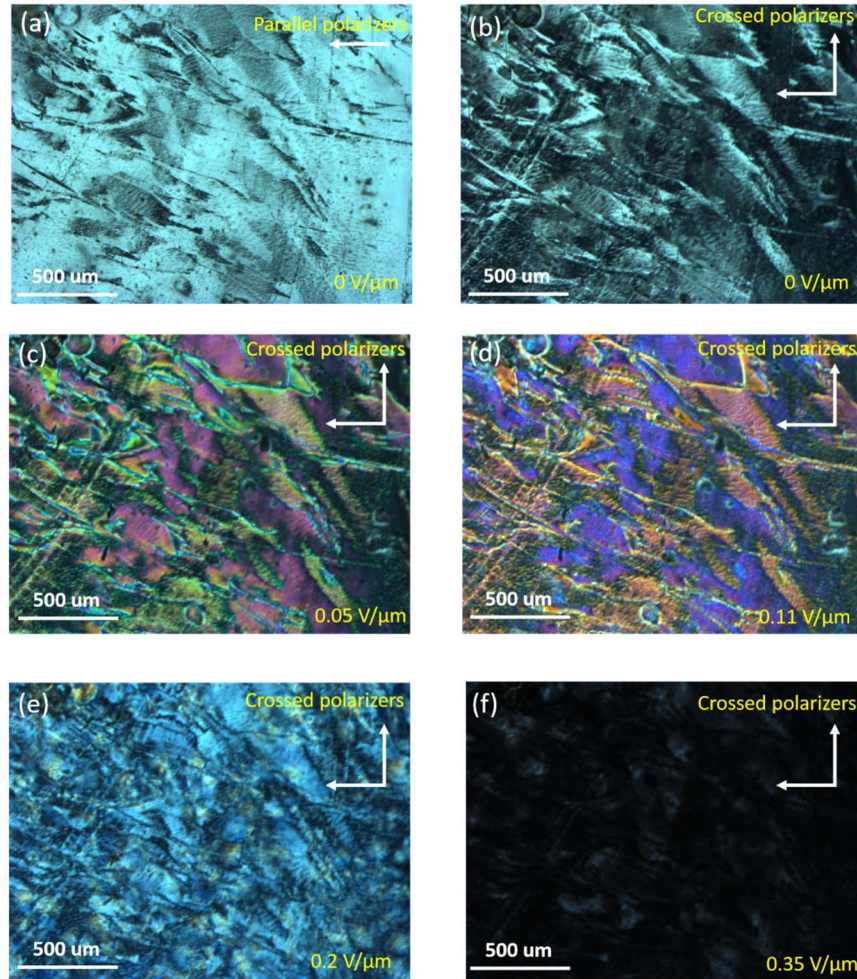


Figure 2.2 Microscopic transmission images of the device under different electric fields. The upper and lower electrode surfaces of the 100 μm -deep LC cell are treated with SCA. (a) No electric field with two parallel polarizers; (b) No electric field with crossed polarizers; (c)-(f) Different electric fields with crossed polarizers. The field strength in each case is given in each panel.

To obtain a uniform and large-area homeotropic alignment of nematic LCs (6CHBT; 1-(trans-4-Hexylcyclohexyl)-4- isothiocyanatobenzene, Sigma-Aldrich, USA) at the Au surface of the nanostructure, we functionalize the Au surface with a fluorinated silane-coupling agent (SCA, trichloro(1H,1H,2H, 2H-heptadecafluorodecyl) silane, Tokyo Chemical Industry, Japan) using a vapor-phase deposition method [32]. In this process, the PDMS-based array of nanoposts, an indium tin oxide (ITO) conducting glass, and a drop of silane-coupling agent (SCA, trichloro-1H,1H,2H,2H-heptadecafluorodecyl silane, Tokyo Chemical Industry, Japan) are placed inside an active vacuum desiccator at room temperature for 5 min, and then is left for another 25 min to complete the deposition process. The formation of a monolayer SCA on nanostructure surface makes it strongly hydrophobic, allowing for homeotropic anchoring and aligning of LC molecules at the nanostructure surface. The LC cell is then formed by placing a conducting ITO glass 100 μm away from the Au surface by using a double-sided silicone adhesive tape (Caplinq, UK). Lastly, the LCs are infused into the cell through a hole preformed in the ITO glass.

To verify the efficacy of the SCA treatment, two polarizers (Thorlabs, USA) are first arranged with their polarization directions parallel to each other and no electric field is applied to the device. In this case, the microscopic transmission image of LC textures appears quite bright (Fig. 2.2(a)). Subsequently, the polarizers are oriented orthogonally with each other and microscopic transmission images of LC textures under different electric fields are taken (Fig. 2.2(b)-(f)). As shown in Fig. 2.2(b), before applying an electric field, the microphotograph of LCs under the crossed polarizers do not become totally dark, indicating that the LC molecules are partially isotropic. This is because the upper and lower electrodes of the cell is 100 μm apart, the interaction between the LC molecules and SCA-treated surfaces may not be sufficient

enough to homeotropically align all the LC molecules. However, after an electric field is applied with increasing field strength, the microphotographs of LCs with the crossed polarizers gradually become darker (Fig. 2.2(c)-(e)). At the field strength of $0.35 \text{ V}/\mu\text{m}$, the LC cell turns to almost completely dark (Fig. 2.2(f)), indicating that under this electric field condition, all the LC molecules in the cell become almost homeotropically aligned to both the upper and lower electrode surfaces treated with SCA.

2.4 Results and Discussion

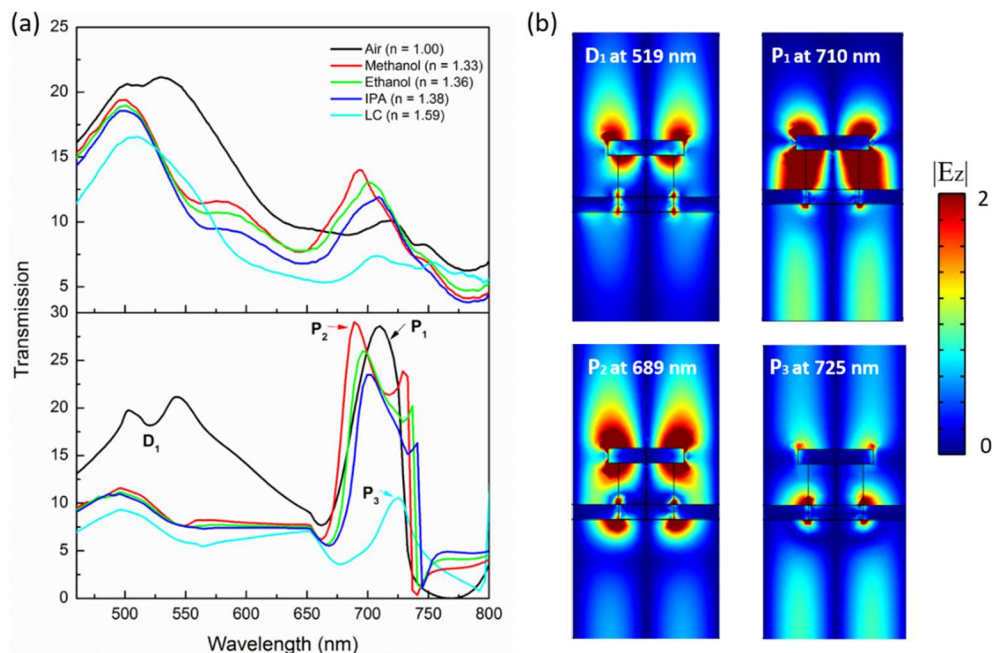


Figure 2.3 (a) Plots in the upper panel show the measured transmission spectra of the quasi-3D plasmonic nanostructure under the normal incidence of light in different media. Plots in the lower panel show the corresponding simulated results. D_1 , P_1 , P_2 , and P_3 in the simulated spectra indicate the transmission features of interest. $\lambda_{D1} = 519 \text{ nm}$ and $\lambda_{P1} = 710 \text{ nm}$ when the nanostructure surface was exposed in air; $\lambda_{P2} = 689 \text{ nm}$ when in methanol ($n = 1.33$); $\lambda_{P3} = 725 \text{ nm}$ when in LC ($n = 1.59$). (b) Simulated cross-sectional electric field distributions ($|E_z|$) at the resonant wavelengths mentioned above.

It should be noted that the optical properties of quasi-3D plasmonic crystals are generally attributed to many possible resonance modes, including SPP at the Au/media interface, LSPR at the Au nanodisks and nanoholes, and non-resonant RA. The coupling effect of these modes will

lead to further rich optical phenomena. Specifically, excitation wavelengths of the SPP and RA change with angle of incidence or surrounding index. Mode coupling between the SPP and RA may further be obtained through index modulations, which recently was demonstrated in planar plasmonic nanohole arrays [5, 6]. In addition, coupled SP resonances may also exist at the Au nanodisks and nanoholes due to their nanoscale distance, which leads to Fabry–Pérot (FP) resonance, as previously reported [12, 16, 18]. The resulting RA-FP resonance mode has a small full width at half maximum, a useful feature that enables high index sensitivity approaching the theoretical limit [12]. In the tunable quasi-3D plasmonic nanostructure presented here, electrical modulation of the effective index of LC will change the coupled resonance between the SPP at the medium/Au interface and the RA excited by the grating effect in the PDMS substrate, which will be discussed later.

To identify the underlying physics of the transmission features of the device, we first measure zero-order transmission spectra with normal incident light to the device surface exposed to air ($n = 1.00$) and different index liquids, including methanol ($n = 1.33$), ethanol ($n = 1.36$), isopropyl alcohol (IPA) ($n = 1.38$), and LC ($n_{eff} = 1.59$) at room temperature [Fig. 2.2(a)]. The effective index of LC is calculated using $n_{eff}^2 = \frac{2}{3}n_o^2 + \frac{1}{3}n_e^2$ [28], where $n_o = 1.53$ and $n_e = 1.71$ [33], representing the ordinary and extraordinary indices, perpendicular to and along the molecule orientation, respectively, of the LCs. In the optical measurement setup (Fig. 2.1(a)), a collimated white light source is generated from a 150 watts quartz halogen lamp. The transmitted light through the device is collected by an optical fiber through a 10× magnification objective lens (NA=0.25) and measured by a spectrometer. The measured transmission spectra are shown in the upper panel of Fig. 2.3(a). When the 3D-quasi plasmonic nanostructure is exposed to air, a transmission dip appears at 519 nm, and a broadband Fano-like resonance profile consisting of a

minimum transmission is observed at 710 nm. Full wave numerical simulations are carried out by using a finite element analysis (FEA) method with the commercial COMSOL software, where the relative permittivity of Au is taken from experimental data [34]. In this simulation, periodic boundary conditions are applied at the boundaries in parallel with the light propagation direction. Two perfect match layers (PMLs) are placed above and below the nanostructure to absorb the scattered electromagnetic (EM) fields. Also, the substrate is considered to be infinitely thick by setting the refractive index of the PMLs to be the same as that of the substrate. As given in the lower panel of Fig. 2.3(a), the simulation results agree with the experimental results when the Au disk has a diameter of 190 nm and a thickness of 60 nm. Note that the close-up SEM image of nanoposts (Fig. 2.1(f) and (g)) shows that there exists subtle isolated nanoscale grains of Au on the sidewall of nanoposts. But, in our simulation, these Au grains are not included in the model, because previous simulation for a similar nanostructure (nanodisk-nanohole pairs separated by air-filled nanowells) has shown that the inclusion of these Au grains on the sidewall will only slightly suppress the resonance intensity and shift the resonant wavelength. In Fig. 2.3(a), the formation of the dip D_1 at 519 nm is attributed to the overlap of (1, 0) SPPs at the air/Au nanodisk interface with the direct light transmission through the thin Au film at the bottom. The peak around the wavelength of 500 nm is due to the direct transmission of light through the Au film. As the real part of the gold dielectric constant becomes +1, it leads to transparency in the absence of damping [5, 13, 14]. For a square lattice, the free space incident wavelength to excite an SPP and the free space incident wavelength of the RA are given respectively by [2]:

$$\lambda_{SPP} = \frac{a}{\sqrt{j_1^2 + j_1^2}} \sqrt{\frac{\epsilon_d \epsilon_m}{\epsilon_d + \epsilon_m}} \quad 2.1$$

$$\lambda_{RA} = \frac{a}{\sqrt{j_2^2 + j_2^2}} \sqrt{\epsilon_d} \quad 2.2$$

where ϵ_d and ϵ_m are the dielectric constant of the medium and Au, a is the lattice constant, and (i_1, j_1) and (i_2, j_2) correspond to the order of SPPs and RA, respectively. According to Equation (1), at a normal incidence in air, the calculated SPP resonance $\lambda_{\text{SPP}}(1, 0)$ at the air/Au interface is 539 nm, which is redshifted compared to the experimental and simulated resonant wavelength at 519 nm. Eq. 1 used to estimate the SPP resonant wavelength is generally considered accurate when the metal film is thick enough. In our experiment, since the thickness of Au is only 60 nm, the interaction of the resonance modes on two sides of the Au film is expected to lead to a blueshift of the measured and FEA simulated resonance, compared to the calculated resonant wavelength using Eq. 2.1. As shown in the electric field distribution (Fig. 2.3(b)), the standing wave feature above the Au nanodisk and below the perforated Au film confirms the excitation of SPPs. At the peak P_1 of 710 nm, the strong interaction between the LSPRs at the Au nanodisk and the Au film leads to a broad FP resonance. This phenomenon has also been observed in Ref. [12, 16, 18]. It is noteworthy that a weak standing wave feature appears in the resonance field distribution at P_1 in the PDMS substrate, but with a deeper field penetration into the substrate compared to the SPP resonance at D_1 . This is attributed to the excitation of $(1, 0)$ RA at the side of the PDMS substrate which is slightly blue-shifted with respect to the calculated RA wavelength at 730 nm, as estimated by Eq. 2.2. Although this RA mode has a relatively weak field intensity, the coupling between the SPP and RA at both sides of the thin Au film causes an enhanced transmission amplitude. As the surrounding medium changes to methanol ($n = 1.33$), a transmission peak with a larger amplitude emerges around 693 nm, which agrees with the simulation result for the peak P_2 . The corresponding field distribution at P_2 (Fig. 2.3(b)) shows a similar pattern in the upper medium region to that at D_1 , except for the region in the PDMS substrate where $(1, 0)_{\text{PDMS}}$ RA occurs. According to Eq. 2.1, as the medium

changes from air to methanol, the resulting $(1, 0)$ SPP red-shifts to 705 nm and this leads to the coupling of $(1, 0)_{\text{methanol/Au}}$ SPP and $(1, 0)_{\text{PDMS}}$ RA. This SPP-RA coupling effect is similar to those that occurred in the planar plasmonic nanohole arrays where the coupling effect was achieved by tuning the position of RA [5, 6]. However, the SPP-RA resonance observed here is achieved by tuning the position of $\lambda_{\text{SPP}}(1, 0)$ at the medium/Au nanodisk interface. Further increasing the index of the surrounding liquid medium to 1.36 and 1.38 causes the SPP-RA resonance to red-shift with a sensitivity of 517 refractive index units per nm (RIU/nm), while gradually decreasing its amplitude.

In the case that the index liquid medium uses LC ($n_{\text{eff}} = 1.59$), both the experiment and simulation show the peak P_3 at 710 nm, but with a relatively lower amplitude compared to the peak P_2 . The corresponding field distribution in Fig. 2.3(b) shows a similar pattern to P_2 but with a much deeper penetration depth, suggesting another coupled SPP-RA resonance. By using Equation (1), $(1, 0)_{\text{LC/Au}}$ SPP is predicted to be at 831 nm, while the $(1, 1)$ order is at 651 nm. The relatively low amplitude at P_3 , in comparison with the peaks caused by the coupling of $(1, 0)$ SPP and RA, is due to two reasons: first, $(1, 1)_{\text{LC/Au}}$ SPP is away from the strongest coupling position at 690 nm; second, $(1, 1)_{\text{LC/Au}}$ SPP suffers more radiative losses than the $(1, 0)$ order. However, the $(1, 1)$ SPP electric field has a much deeper penetration rate into the medium than the $(1, 0)$ order, which can be a benefit in designing LC-based plasmonic tunable devices.

With increasing applied electric field, the LC molecules tend to be aligned with the electric field and become predominantly perpendicular to the substrate surface. Because the coupled SPP-RA mode has its electric field predominantly normal to the surface of the plasmonic nanostructure and extends up into the LC thin layer (as shown in Fig. 2.3(b)), the resonance characteristics of the device become sufficiently sensitive to index changes in the

direction perpendicular to the LC/Au interface. Let us first assume the LC molecules experience a transition from a total isotropic state to a total homeotropic state. Under this assumption, the resulting maximum index variation in the perpendicular direction will be 0.12 or $n_e - n_{eff}$. Obviously, this theoretical index change is overestimated. Nevertheless, a redshift of the coupled SPP-RA resonance will still be expected. Figure 2.4(a) shows the measured zero-order transmission spectra for different applied electric fields. By increasing the field strength to 0.55 V/ μm , a maximum resonant wavelength shift of 8 nm with a 35% change in amplitude at the SPP-RA resonance is observed. Based on the measured resonance shift of 8 nm and the measured sensitivity of 517 RIU/nm mentioned above, the actual index change is calculated to be 0.015, which is much lower than the theoretical maximum value of 0.12 mentioned above. This is because the initial alignment of LC molecules is not fully homeotropic to the upper and lower electrode surfaces. After applying an electric field, the LCs tend to become homeotropic. Note that previous work on LC-based plasmonic switches also reported the resonance shift due to the LC reorientation from a partially homeotropic state to a homeotropic state [35].

In other reported LC-based tunable plasmonic devices using SPP or LSPR mode confined at the dielectric/metal interface, the SPP field usually has a longer decay length and can extend more into the surrounding medium, and thus exhibits higher sensitivity to the reorientation of LC molecules than the LSPR field does. Consequently, the LC devices using SPP mode require a lower operating electric field (e.g., ~ 1.25 V/ μm [23]) than those using LSPR mode (e.g., ~ 2 V/ μm [21] and 5 V/ μm [22]). It should be pointed out that by coupling SPP and RA mode, our device has a higher field enhancement capability and allows extending the coupled field deeper into the LC layer. This unique feature leads to a lower operating electric field of ~ 0.55 V/ μm of our device than the previously reported LSPR or SPP based LC devices [21-23].

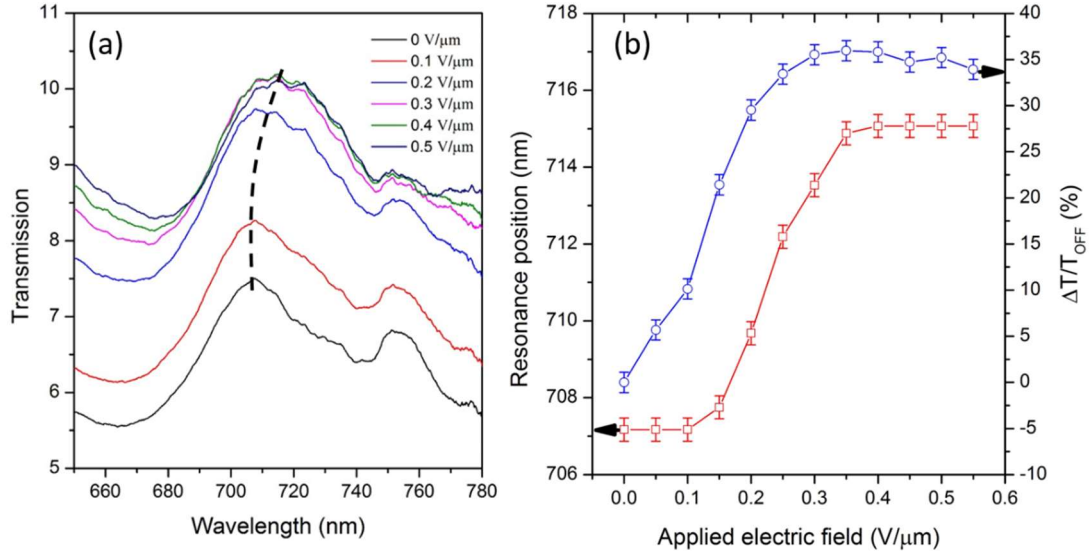


Figure 2.4 (a) Transmission spectra of the LC-based quasi-3D plasmonic crystal at different applied electric field strengths. (b) Wavelength and relative transmission variation of the SPP-RA resonance as a function of applied electric field strength. $\Delta T = T_{ON} - T_{OFF}$, where T_{ON} and T_{OFF} represent transmission intensity when an external voltage is at the ON and OFF state, respectively.

2.5 Conclusions

In summary, we have demonstrated a LC-based electrically tunable quasi-3D plasmonic crystal, where both the experiment and simulation results have confirmed the coupling effect between RA and SPP resonance. The SPP-RA resonance field is predominantly normal to the surface of the plasmonic nanostructure and penetrates into the surrounding LC, which makes the resonance sensitive to the molecular reorientation of the LC. The ability of the device to tune its optical response suggests many potential applications in the areas of micro-display, sensing, and complex optical signal processing.

2.6 Acknowledgment

The authors would thank Seval ÖREN for SEM imaging, Yifei Wang for gold evaporation, and Dr. Meng Lu and Longju Liu for helpful discussions. P. L. thanks the China Scholarship Council for partial financial support.

2.7 References

- [1] Barnes, W. L., Dereux, A. & Ebbesen, T. W. Surface plasmon subwavelength optics. *Nature* **424**, 824-830, doi:10.1038/nature01937 (2003).
- [2] Ghaemi, H. F., Thio, T., Grupp, D. E., Ebbesen, T. W. & Lezec, H. J. Surface plasmons enhance optical transmission through subwavelength holes. *Physical Review B* **58**, 6779-6782, doi:10.1103/PhysRevB.58.6779 (1998).
- [3] Sarrazin, M., Vigneron, J. P. & Vigoureux, J. M. Role of Wood anomalies in optical properties of thin metallic films with a bidimensional array of subwavelength holes. *Physical Review B* **67**, doi:10.1103/PhysRevB.67.085415 (2003).
- [4] Steele, J. M., Moran, C. E., Lee, A., Aguirre, C. M. & Halas, N. J. Metallodielectric gratings with subwavelength slots: Optical properties. *Physical Review B* **68**, doi:1103/PhysRevB.68.205103 (2003).
- [5] McMahon, J. M., Henzie, J., Odom, T. W., Schatz, G. C. & Gray, S. K. Tailoring the sensing capabilities of nanohole arrays in gold films with Rayleigh anomaly-surface plasmon polaritons. *Optics Express* **15**, 18119-18129, doi:10.1364/oe.15.018119 (2007).
- [6] Gao, H. *et al.* Rayleigh anomaly-surface plasmon polariton resonances in palladium and gold subwavelength hole arrays. *Optics Express* **17**, 2334-2340, doi:10.1364/oe.17.002334 (2009).
- [7] Hicks, E. M. *et al.* Controlling plasmon line shapes through diffractive coupling in linear arrays of cylindrical nanoparticles fabricated by electron beam lithography. *Nano Letters* **5**, 1065-1070, doi:10.1021/nl0505492 (2005).

- [8] Vecchi, G., Giannini, V. & Rivas, J. G. Surface modes in plasmonic crystals induced by diffractive coupling of nanoantennas. *Physical Review B* **80**, doi:10.1103/PhysRevB.80.201401 (2009).
- [9] Kravets, V. G., Schedin, F. & Grigorenko, A. N. Extremely narrow plasmon resonances based on diffraction coupling of localized plasmons in arrays of metallic nanoparticles. *Physical Review Letters* **101**, doi:10.1103/PhysRevLett.101.087403 (2008).
- [10] Zhou, W. & Odom, T. W. Tunable subradiant lattice plasmons by out-of-plane dipolar interactions. *Nature Nanotechnology* **6**, 423-427, doi:10.1038/Nnano.2011.72 (2011).
- [11] Eitan, M. *et al.* Degeneracy Breaking of Wood's Anomaly for Enhanced Refractive Index Sensing. *Acs Photonics* **2**, 615-621, doi:10.1021/acsp Photonics.5b00091 (2015).
- [12] Shen, Y. *et al.* Plasmonic gold mushroom arrays with refractive index sensing figures of merit approaching the theoretical limit. *Nature Communications* **4**, doi:10.1038/Ncomms3381 (2013).
- [13] Stewart, M. E. *et al.* Quantitative multispectral biosensing and 1D imaging using quasi-3D plasmonic crystals. *Proceedings Of the National Academy Of Sciences Of the United States Of America* **103**, 17143-17148, doi:10.1073/pnas.0606216103 (2006).
- [14] Truong, T. T. *et al.* Nanopost plasmonic crystals. *Nanotechnology* **20**, doi:10.1088/0957-4484/20/43/434011 (2009).
- [15] Bezares, F. J. *et al.* The Role of Propagating and Localized Surface Plasmons for SERS Enhancement in Periodic Nanostructures. *Plasmonics* **7**, 143-150, doi:10.1007/s11468-011-9287-3 (2012).

- [16] Xu, J. J. *et al.* Understanding the effects of dielectric medium, substrate, and depth on electric fields and SERS of quasi-3D plasmonic nanostructures. *Optics Express* **19**, 20493-20505, doi:10.1364/oe.19.020493 (2011).
- [17] Najiminaini, M., Vasefi, F., Kaminska, B. & Carson, J. J. L. Transmission resonance of a three dimensional nano-structure with a localized surface plasmon property. *Plasmonics in Biology and Medicine X* **8597**, doi:10.1117/12.2005133 (2013).
- [18] Artar, A., Yanik, A. A. & Altug, H. Fabry-Peacuterot nanocavities in multilayered plasmonic crystals for enhanced biosensing. *Applied Physics Letters* **95**, doi:10.1063/1.3202391 (2009).
- [19] Xu, J. J. *et al.* Light Transmission and Surface-Enhanced Raman Scattering of Quasi-3D Plasmonic Nanostructure Arrays with Deep and Shallow Fabry-Perot Nanocavities. *Journal Of Physical Chemistry C* **115**, 10996-11002, doi:10.1021/jp202110s (2011).
- [20] Baca, A. J. *et al.* Optimization of Nanopost Plasmonic Crystals for Surface Enhanced Raman Scattering. *Journal Of Physical Chemistry C* **115**, 7171-7178, doi:10.1021/jp109066c (2011).
- [21] Kossyrev, P. A. *et al.* Electric field tuning of plasmonic response of nanodot array in liquid crystal matrix. *Nano Letters* **5**, 1978-1981, doi:10.1021/nl0513535 (2005).
- [22] Chu, K. C. *et al.* Electrically controlled surface plasmon resonance frequency of gold nanorods. *Applied Physics Letters* **89**, doi:10.1063/1.2335812 (2006).
- [23] Dickson, W., Wurtz, G. A., Evans, P. R., Pollard, R. J. & Zayats, A. V. Electronically controlled surface plasmon dispersion and optical transmission through metallic hole arrays using liquid crystal. *Nano Letters* **8**, 281-286, doi:10.1021/nl072613g (2008).

- [24] Liu, Y. J., Leong, E. S. P., Wang, B. & Teng, J. H. Optical Transmission Enhancement and Tuning by Overlying Liquid Crystals on a Gold Film with Patterned Nanoholes. *Plasmonics* **6**, 659-664, doi:10.1007/s11468-011-9248-x (2011).
- [25] De Sio, L. *et al.* Double active control of the plasmonic resonance of a gold nanoparticle array. *Nanoscale* **4**, 7619-7623, doi:10.1039/c2nr31426f (2012).
- [26] Hsiao, V. K. S., Zheng, Y. B., Juluri, B. K. & Huang, T. J. Light-driven plasmonic switches based on Au nanodisk arrays and photoresponsive liquid crystals. *Advanced Materials* **20**, 3528+, doi:10.1002/adma.200800045 (2008).
- [27] Zhao, Y. H. *et al.* Light-driven tunable dual-band plasmonic absorber using liquid-crystal-coated asymmetric nanodisk array. *Applied Physics Letters* **100**, doi:10.1063/1.3681808 (2012).
- [28] Xiao, S. M. *et al.* Tunable magnetic response of metamaterials. *Applied Physics Letters* **95**, 033115, doi:10.1063/1.3182857 (2009).
- [29] Cetin, A. E., Mertiri, A., Huang, M., Erramilli, S. & Altug, H. Thermal Tuning of Surface Plasmon Polaritons Using Liquid Crystals. *Advanced Optical Materials* **1**, 915-920, doi:10.1002/adom.201300303 (2013).
- [30] Liu, Y. J. *et al.* Surface Acoustic Wave Driven Light Shutters Using Polymer-Dispersed Liquid Crystals. *Advanced Materials* **23**, 1656+, doi:10.1002/adma.201003708 (2011).
- [31] Si, G. Y., Zhao, Y. H., Leong, E. S. P. & Liu, Y. J. Liquid-Crystal-Enabled Active Plasmonics: A Review. *Materials* **7**, 1296-1317, doi:10.3390/ma7021296 (2014).
- [32] Yoshida, H. *et al.* Uniform liquid crystal alignment on metallic nanohole arrays by vapor-phase deposition of silane coupling agent. *Optical Materials Express* **2**, 893-899, (2012).

- [33] Baran, J. W., Raszewski, Z., Dabrowski, R., Kedzierski, J. & Rutkowska, J. Some Physical-Properties of Mesogenic "4-(Trans-4'-Normal-Alkylcyclohexyl) Isothiocyanatobenzenes. *Molecular Crystals And Liquid Crystals* **123**, 237-245, 1985).
- [34] Palik, E. D. *Handbook of optical constants of solids*. (Academic Press, 1985).
- [35] Liu, Y. J. *et al.* A frequency-addressed plasmonic switch based on dual-frequency liquid crystals. *Applied Physics Letters* **97**, doi:10.1063/1.3483156 (2010).

CHAPTER 3

TUNABLE OPTICAL NANOANTENNAS INCORPORATING BOWTIE NANOANTENNA
ARRAYS WITH STIMULI-RESPONSIVE POLYMER

A paper published in Scientific Report

Qiugu Wang, Longju Liu, Yifei Wang, Peng Liu, Huawei Jiang, Zhen Xu, Zhuo Ma, Seval Oren,
Edmond K.C. Chow, Meng Lu, and Liang Dong

3.1 Abstract

The ever-increasing demand for active control of optical properties of nanostructures has resulted in technological innovations to achieve reconfigurable features in size-limited devices. Compromises, however, are often made to optical device designs among their footprint, functionality, and complexity. Existing resonance-based devices require external control systems to accomplish reconfigurability. Here, we demonstrate environment-responsive autonomous plasmonic devices that incorporate coupled bowtie nanoantenna arrays (BNAs) with a submicron-thick, environment-responsive hydrogel coating. The coupled plasmonic nanoparticles provide an intrinsically higher field enhancement than conventional individual nanoparticles. The favorable scaling of plasmonic dimers at the nanoscale and ionic diffusion at the submicron scale is leveraged to achieve strong optical resonance and rapid hydrogel response, respectively. We demonstrate that the smart BNAs are able to be self-adapted to local environmental temperature variations driven by chemical to mechanical energy conversion. The phase transition of hydrogel brings 16.2 nm of resonant wavelength shift for the hydrogel-coated BNAs, whereas only 3 nm for the uncoated counterpart. In addition, the response time of the device to temperature variations is only 250 ms, due to the submicron-thick hydrogel. This research suggests a series of smart plasmonic nanoantennas with various stimuli-responsive hydrogels for applications in optics, sensing, and lab-chip devices.

3.2 Introduction

Reconfigurable plasmonic devices have attracted much attention, because of an increasing demand for tunable optical properties to accommodate flexible application requirements. Often, these active devices are structurally variable, or hybridizing functional materials (e.g., liquid crystal, semiconductor, phase-change media, and etc) with plasmonic structures [1, 2]. Various tuning mechanisms (e.g., mechanical stretching [3], thermo- and electro-mechanical [4-6], electro-, magneto-, and thermo-optical [7-10], and electron beam manipulation [11]) have been studied to regulate their structural configurations or refractive indices of surrounding media. Recently, stimuli-responsive, surface-bound hydrogels have been suggested as a promising candidate to realize active plasmonic devices [12-24]. These polymers are sensitive to different stimuli (e.g., temperature, pH, light, glucose, electric field, and ions strength), by changing their volume or shape [25, 26]. Most of the existing efforts in active plasmonics with hydrogels have mainly focused on using metallic nanoparticles or islands attached to polymer brushes [12-19], and on functionalizing gold (Au) films with hydrogels [20, 21]. As these nonlithographic nanoparticles have relatively poor control over their shape and size, fine tuning for optical properties of the nanoparticles-hydrogel composites is challenging; also, their optical responses usually have undesirable, broad resonance bands. Lithographically nanopatterned particles have thus been utilized to integrate with hydrogel [21-24], but almost all the reported research dealt with isolated nanoparticles unfavorable to achieving high field enhancement, thus hindering the improvement in their tuning range and sensitivity to specific environmental changes.

We herein report on smart coupled plasmonic bowtie nanoantennas (BNAs) that offer autonomous adaptation to changing environmental conditions by reconfiguring its resonance

properties. Neither any external controls nor external power supplies are needed. In contrast to individual nanoparticles, coupled plasmonic nanoparticles provide an intrinsically higher field enhancement. Their integration with stimuli-responsive hydrogel is expected to bring a synergistic effect to improve tuning of active plasmonics in response to environmental changes. Basically, plasmonic BNA is coupled metallic nanoparticle dimers with two tip-to-tip nanotriangles [27]. The nanoscale air gap between the nanotriangles allows for tight confinement and large enhancement of optical fields through the excitation of surface plasmons (SPs). This effect has been harnessed for many applications, such as high-harmonic generation [28], fluorescence enhancement [29], nanolasing [30], and optical trapping [31, 32]. In this study the smart BNAs are formed by simply coating the top surface of BNAs with a submicron-thick, stimulus-responsive hydrogel. As a specified environmental parameter changes, there will be a change in the refractive index of hydrogel, accompanied by swelling or deswelling behavior of the hydrogel cross-linked network in water. This will result in changing optical characteristics of the BNAs. Herein, the scaling of plasmonic dimers and ionic diffusion is favorably leveraged to achieve strong BNA resonance and rapid hydrogel response time, respectively. The creation of the smart BNAs takes advantages of these scaling properties.

3.3 Results and Discussion

We demonstrate the autonomous BNAs using thermosensitive poly(N-isopropylacrylamide) or PNIPAAm hydrogel that expands at low temperatures and contracts at high temperatures with a volume phase transition temperature (VPTT) at approximate 32 °C. The volumetric change of hydrogel causes a continuous and reversible change in its refractive index, typically between 1.36 and 1.46 [33]. As the degree of swelling drastically changes around the VPTT, the hydrogel-coated BNAs present a considerable resonant wavelength shift of 16.2 nm.

In contrast, with the same temperature change, the uncoated device yields only 3 nm resonant wavelength shift. Furthermore, the hydrogel-coated BNAs respond to environmental changes rapidly within 250 ms because the thickness of hydrogel is reduced to a submicron scale for fast ion diffusion. The present smart BNAs device is structurally simple, and can be modified to incorporate many other hydrogels that respond, for example, to light, pH, electric fields, and antigens, for use as physical, biological or chemical sensors.

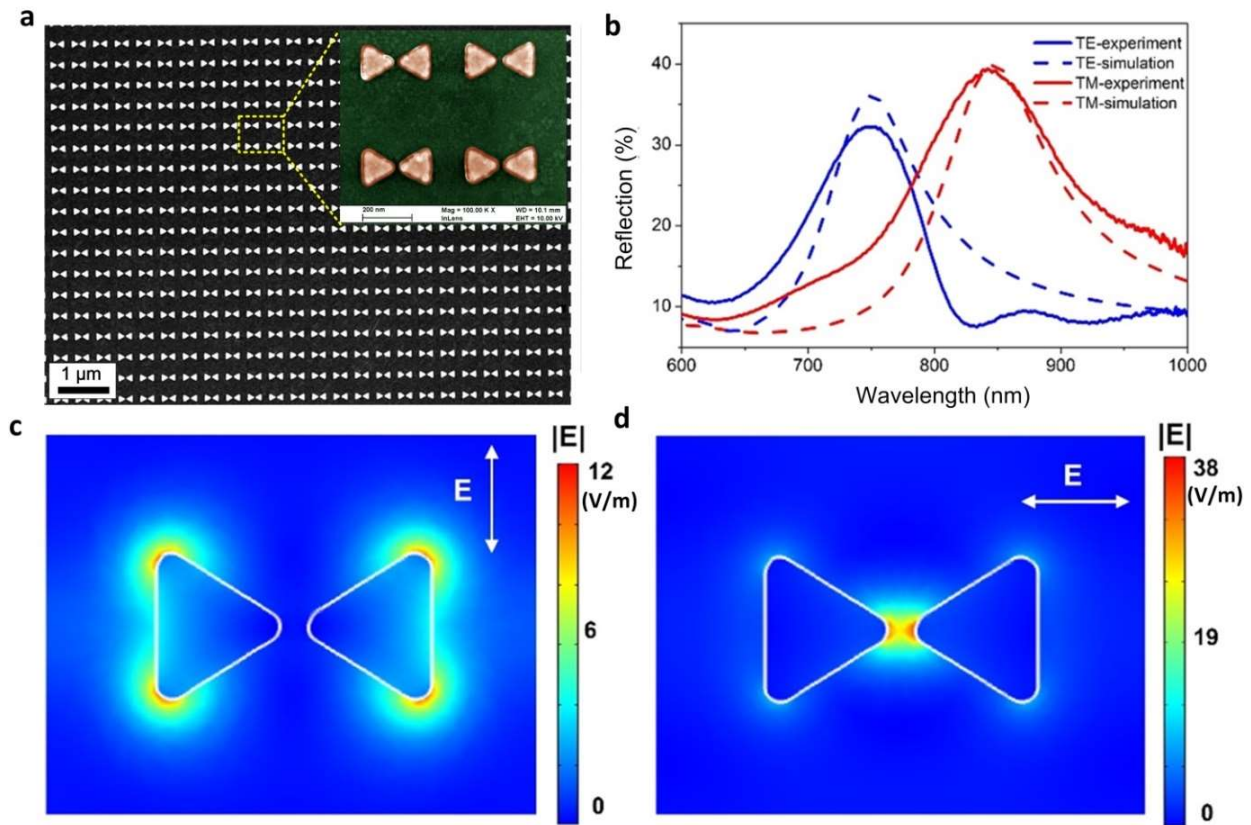


Figure 3.1 (a) Scanning electron microscopy (SEM) image for the bare Au BNAs without a hydrogel coating. The inset shows a pseudo-color SEM image for a close-up of BNAs. (b) Experimental and simulated reflection spectra of the uncoated BNAs in water under normally incident TE and TM polarized light. (c, d) Normalized electric field distributions at the resonances under the TE (c) and TM (d) polarization, respectively. The color scale bars show the normalized electric field amplitude relative to the incident field $|E_0|$.

In this study, 50 nm thick Au BNAs were patterned in 428 nm spaced square arrays covering an area of $500 \times 500 \mu\text{m}^2$ on a 25 nm thick indium tin oxide (ITO) coated glass

substrate (Fig. 3.1(a)). Each bowtie consists of two equilateral triangles with a side length of 150 nm and a tip-to-tip distance of 20 nm (see the inset of Fig. 3.1(a)). We first measured the reflection spectra of the bare BNAs (without hydrogel coating) using a spectroscopic measurement setup. For the transverse magnetic (TM) polarization, the excitation light has the electric field component along (parallel to) the nanogap direction of the bowtie. Figure 3.1(b) shows that the uncoated BNAs have a resonance at 838 nm for TM polarization and the other at 750 nm for transverse electric (TE) polarization. We then performed full wave simulation using a finite element analysis method. The simulation results show a good agreement with the experimental ones in terms of their resonance positions (Fig. 3.1(b)). The minor difference in the spectra may be attributed to imperfect structural uniformity of the fabricated device. Figures 3.1(c)-(d) show the electric field distributions at the resonances under TE and TM polarizations. In the case of TM polarization, the surface plasmon resonance leads to significant field confinement inside the nanogap of the bowtie with a maximum amplitude enhancement factor of 38, while under TE polarization, the “hot spots” occur at the two base corners of each triangle with a much lower maximum enhancement factor of 12. Therefore, the strong ability of the BNAs to enhance the local field amplitude, especially at the TM resonance, is promising to enable effective tuning of their optical characteristics by minute changes of the surrounding index.

To form the proposed smart BNAs, we coated the top surface of the BNAs with a 750 nm thick PNIPAAm hydrogel layer [34] (Figs. 3.2(a)-(c)). The fabrication details are described in Materials and Methods. We studied optical responses of the hydrogel-coated and uncoated BNAs to local environmental temperature changes. Fig. 3.2(d) shows the reflection spectra of the two devices at room temperature (22 °C), both with normal incidence of non-polarized light.

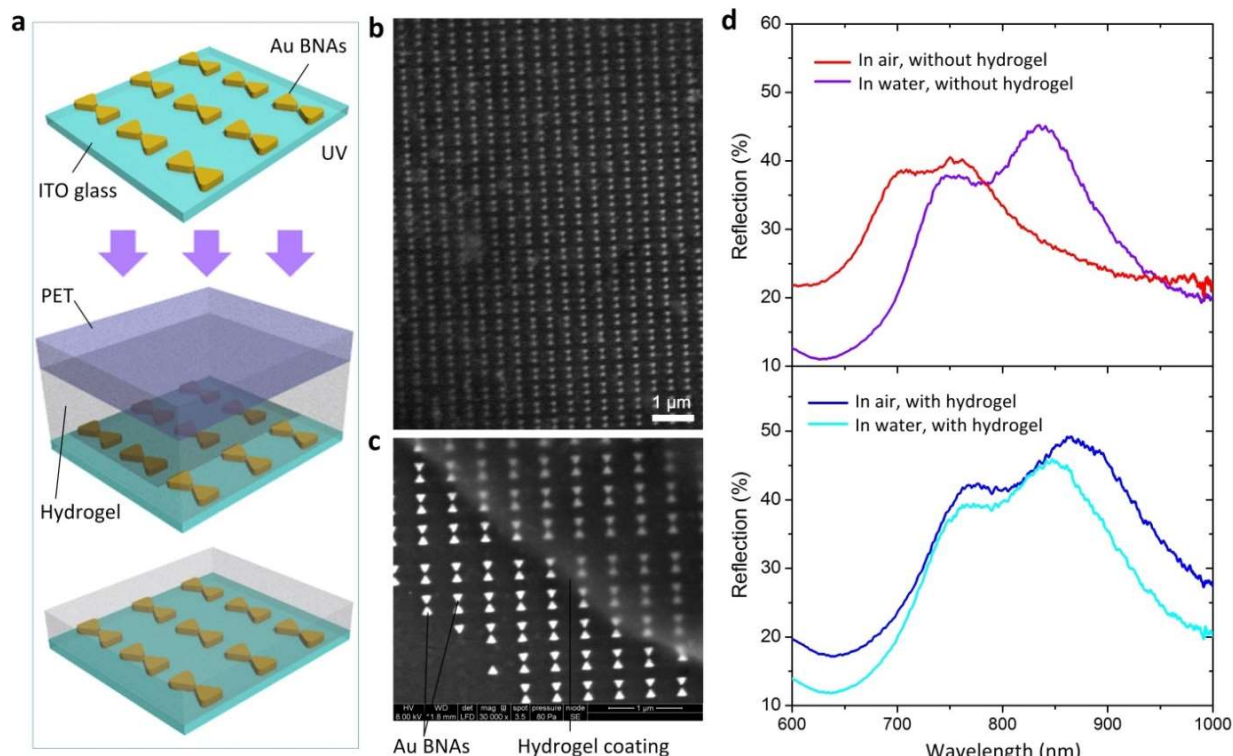


Figure 3.2 (a) Fabrication processes for the environment-responsive smart BNAs. (b) SEM image of the hydrogel-coated BNAs. (c) SEM image showing the morphological difference between the hydrogel-coated and the uncoated BNAs. The hydrogel at the edge was intentionally unexposed to ultraviolet (UV) light during the device fabrication. (d) Reflection spectra of the uncoated BNAs (upper panel) and the hydrogel-coated device (lower panel) in air and water at 22 °C under non-polarized normal light incidence.

Immersing the uncoated BNAs in water caused a resonant wavelength red shift of 83 nm and 40 nm to the TM and TE modes, respectively. After the uncoated device were coated with PNIPAAm hydrogel, the TM and TE resonances red shifted by 92 nm and 50 nm, respectively. By immersing the hydrogel-coated device in water at 22 °C, both the TE and TM resonances red shifted, but with different amounts: 25 nm for the TM mode and 7.5 nm for the TE mode. It is also noteworthy that when immersed in water, the two devices shifted their resonant wavelength in an opposite direction. This is because the as-polymerized hydrogel on the smart BNAs initially absorbed water to reach an initial equilibrium, giving rise to an increase in physical volume, in accompany with a decrease in refractive index, thus causing a blue resonance shift. In

addition, the introduction of the hydrogel to the surface of the BNAs did not significantly influence the bandwidth of the plasmonic resonances.

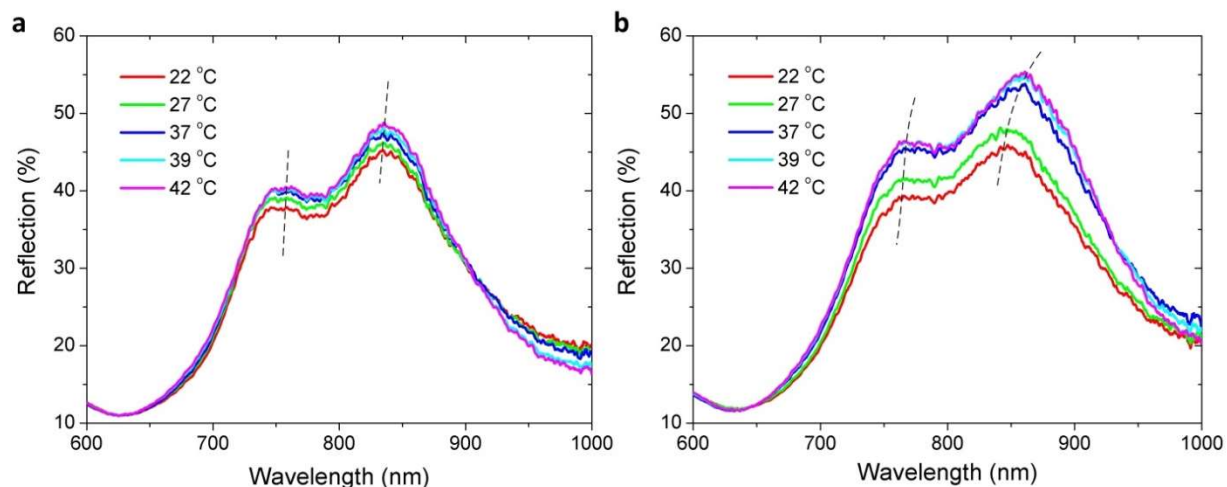


Figure 3.3 (a) Reflection spectra of the uncoated BNAs at different temperatures. (b) Reflection spectra of the hydrogel-coated BNAs at different temperatures. The spectra were measured under normally incident non-polarized light.

Figure 3.3 shows the reflection spectra of the hydrogel-coated and uncoated BNAs as the environment temperature changes from 22 to 42 °C. First, when responding to an increase in temperature, the hydrogel-coated device showed a larger increase in reflection intensity than the uncoated counterpart, because of a larger increase in refractive index for the hydrogel-coated BNAs. As for the resonance response to increasing temperature, the TM resonance peak of the hydrogel-coated device significantly red shifted by 16.2 nm, while the TE resonance peak shifted by 8 nm (Fig. 3.3(b)). This difference may result from the higher field enhancement factor at the TM mode than that at the TE mode. Figure 4a shows that the majority of the resonance shift occurred around the VPTT of the hydrogel, due to the phase transition induced large index change, confirming the function of the hydrogel in tuning the optical properties of the hydrogel-coated BNAs.

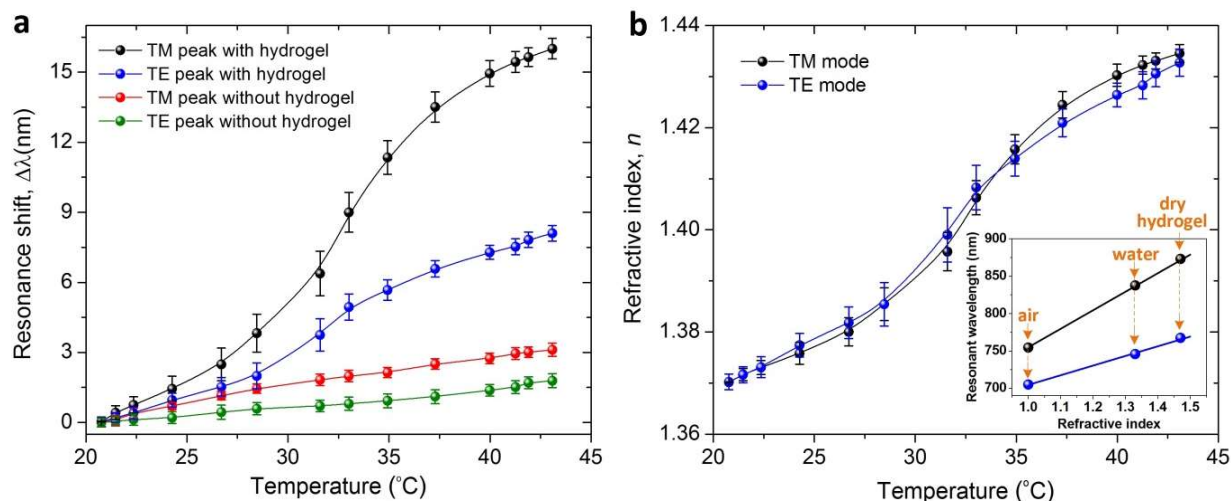


Figure 3.4 (a) TM and TE mode resonance shifts of the hydrogel-coated and uncoated BNAs as a function of temperature. (b) Calculated refractive index of the PNIPAAm hydrogel as a function of temperature. The inset shows the TE and TM resonant wavelengths of the BNAs as a function of environmental refractive index n . The yellow arrows indicate the different surrounding media, including air, water, and dry hydrogel [35, 36].

To estimate how the refractive index of the hydrogel coating changed with temperature, we first plotted the TM and TE resonant wavelengths of the Au BNAs with respect to the refractive indices of different surrounding media, including air ($n = 1$), water ($n = 1.33$), and a dry hydrogel layer ($n = 1.48$) [35, 36]. The slopes of the two plots in the inset of Fig. 3.4(b) indicate that the BNAs have the refractive index sensitivity of 248 nm/RIU (RIU: refractive index unit) and 129 nm/RIU for the TM and TE resonances, respectively. Based on the resonance wavelength shift (Fig. 3.4(a)) of the hydrogel-coated BNAs and the refractive index sensitivity obtained above, the refractive index of the hydrogel coating at different temperatures was extracted. As the temperature increased from 22 $^{\circ}\text{C}$ to 42 $^{\circ}\text{C}$, the refractive index increased from 1.37 to 1.435, with a total index variation of 0.065 (Fig. 3.4(b)). Essentially, the effective refractive index variation of the BNAs may be attributed to the following factors. The dominating factor is the volume change induced index change of the hydrogel coating. As the local temperature increased by 20 $^{\circ}\text{C}$, the refractive index of the hydrogel was significantly

increased by 4.74%. Another factor relates to changes in thermophysical properties of other device materials (i.e., water, Au, and ITO-coated glass), which is considered to have an insignificant effect on the resonance shift, as evident by a maximum 3 nm and 1.6 nm shift of the TM and TE mode resonance peaks, respectively, of the uncoated BNAs (Fig. 3.3(a) and Fig. 3.4(a)). The temperature induced dispersion change of Au may also contribute to the observed resonance shift of both the hydrogel-coated device and the uncoated counterpart, in accompany with a minor decrease in quality factor. At 830 nm near the TM mode resonance of the BNAs, as the temperature increases from 22 °C to 42 °C, the real part of Au permittivity remains almost the same at the value of -8, while the imaginary part changes from 1.6 to 1.9, which leads to an increase in radiative losses [37]. This, in turn, may cause a decrease in collective coupling of neighboring bowties, thus slightly red shifting the TM mode resonant wavelength.

To further demonstrate the ability of the BNAs to dynamically respond to environmental temperature changes, we applied a temperature stimulus by flowing warm water (42 °C) over the surface of both the hydrogel-coated and uncoated BNAs in a microfluidic channel. Figure 2.5 tracks the TE and TM mode resonant wavelengths of the two devices during temperature rising and natural cooling. For the uncoated device (Fig. 3.5(a)), the resonance shift of each resonance mode has a similar trend with the temperature variation. As the warm water arrived, the resonance shift of each peak reached a maximum value of about 3 nm for TM mode and 1.6 nm for TE mode. As the device naturally cooled down, the resonance peaks progressively blue shifted until a new temperature stimulus came. For the hydrogel-coated device (Fig. 3.5(b)), the overall resonance shift patterns are similar to those for the uncoated one, except for having a much larger amplitude at the level of 16.2 nm for TM mode and 8 nm for TE mode. Figure 3.5(b) further confirms the phase transition effect of the hydrogel around 32 °C on the resonance

shift of the device. The resonant wavelength blue shifted much faster at 29-35 °C than it did in other temperatures. Therefore, the hydrogel-coated device is able to dynamically sense the environmental temperature variations and take action to shift its resonance shift.

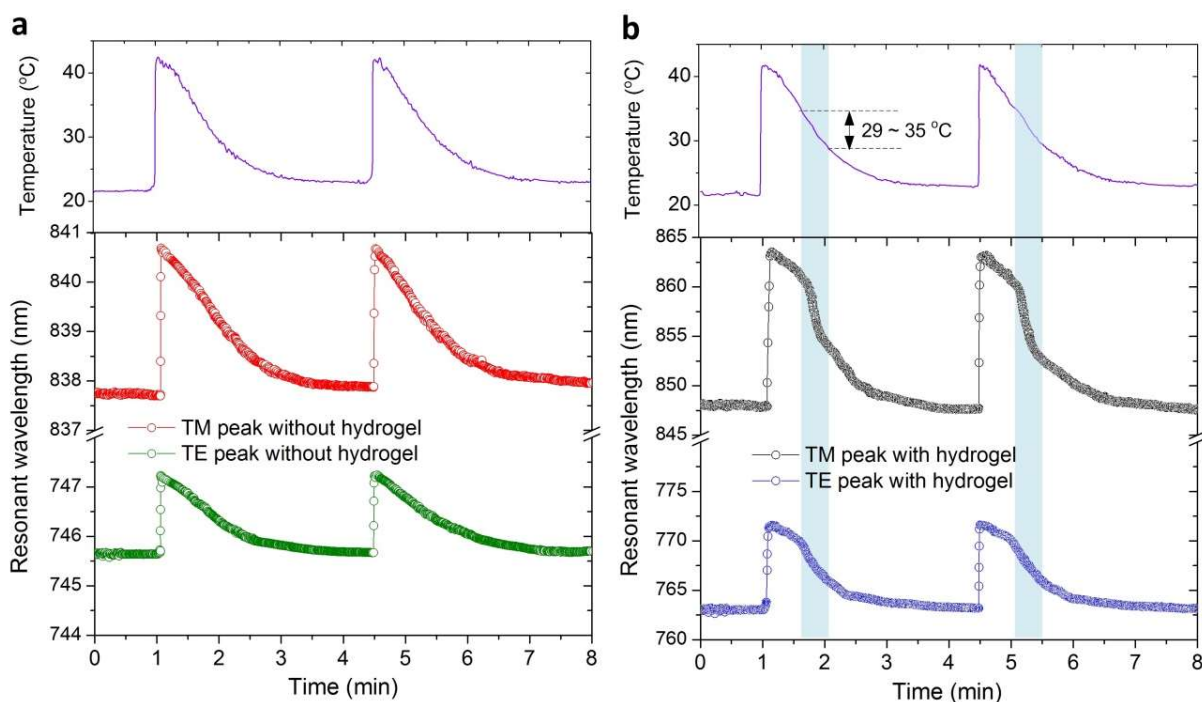


Figure 3.5 Dynamic tracking of TE and TM mode resonance peaks for the uncoated BNAs (a) and the hydrogel-coated BNAs (b) at different temperatures. The upper panels in (a) and (b) show the changing environmental temperatures.

To quantify how fast the hydrogel-coated BNAs respond to temperature changes, we tracked changes in reflection intensity of the hydrogel-coated BNAs at the TM mode wavelength of 847 nm at 22 °C. In this study, warm water at a raised temperature (i.e., 30, 32, 35, or 37°C) was continuously injected into the channel such that the surface temperature of the BNAs remained constant. As the warm water flowed over the device, the reflection intensities at the two fixed wavelengths reached maximum or plateau values in just about one second (Figure 3.6). It should be pointed out that a response time of only 250 ms was observed for the device; this refers to the time from being exposed 42 °C warm water to a clear intensity change shown on the

spectrometer. Such a short response time is attributed to the use of the submicron hydrogel coating, because the time response of the volume change approximately follows the square of the dimension as the hydrogel structure reversibly expands and contracts, depending on the temperature of the surrounding environment. As the temperature was kept constant, the hydrogel remained in a contracted state where no volumetric change of the hydrogel occurred. As a result, the resonant wavelength remained unchanged, forming the intensity plateau.

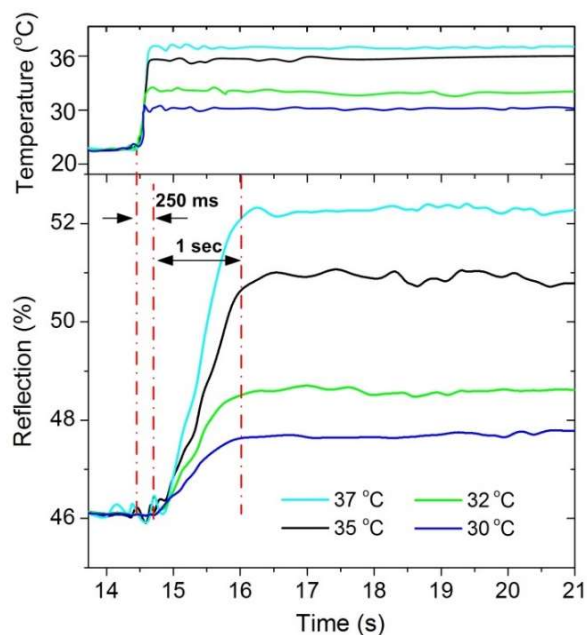


Figure 3.6 Dynamic tracking of reflection intensity of the hydrogel-coated BNAs at different temperatures. Water at different temperatures (37, 35, 32, and 30 °C) flowed over the surface of the BNAs located on the bottom of a microfluidic channel.

While this study utilizes the PNIPAAm hydrogel with a fixed VPTT as a model hydrogel to proof the concept of stimuli-responsive BNAs, the use of multiple thermoresponsive hydrogels with different VPTTs for multiple temperature-responsive BNAs will make it feasible to program the response of each individual BNAs device where a specific hydrogel coating is used [38]. This will provide adequate flexibility in the design of stimuli-responsive BNAs. Furthermore, a variety of hydrogels can be used to further diversify the tuning mechanisms and

their applications [39]. For example, functionally complex BNAs can be realized to act as biological and chemical sensors to detect multi-environmental parameters, and subsequently generate optical outputs (resonant wavelength, and optical intensity). By working in the scale range of submicron for stimuli-responsive hydrogels where ion diffusion pathway is favorably short, and by working in the scale range of nanometers for BNAs where the localized field is sensitive to small local index changes, the stimuli-responsive BNAs will bridge local environmental input parameters with optical resonance outputs through the use of stimuli-responsive hydrogels.

3.4 Methods and Experimental Details

The NIPAAm hydrogel precursor solution was prepared according to the recipe described in Ref. [34]. The hydrogel solution contained 14.3 wt% NIPAAm, 2 wt% crosslinking agent N,N'-methylenebis (acrylamide) (99%) (BIS), and 2 wt% photoinitiator 2-hydroxy-4'-(2-hydroxyethoxy)-2-methyl propiophenone (98%) in distilled water (all purchased from Sigma-Aldrich).

The BNAs were fabricated on a $25 \times 25 \times 0.42 \text{ mm}^3$ ITO-coated glass slide. E-beam lithography was used to form nanopatterns of BNAs in poly(methyl methacrylate) resist (Sigma-Aldrich). The area of the BNAs is $500 \times 500 \text{ }\mu\text{m}^2$ with a periodicity of 428 nm in each direction. Each bowtie has a length of 150 nm and a tip-to-tip distance of 20 nm. A 5 nm thick titanium adhesion layer and a 50 nm thick Au layer were evaporated onto the sample using an e-beam evaporator. Subsequently, a lift-off process was used to remove the metal from the regions where the e-beam resist remained. The sample was immersed into pure acetone with sonication for 20 mins. Therefore, the Au BNAs were formed.

To coat the NIPAAm hydrogel on the BNAs, a shallow air cavity was created between the ITO-coated glass slide and a polyethylene terephthalate (PET) slab. Here, a 750 nm thick photoresist was spin-coated and patterned on the glass slide to form multiple spacers. The PET slab was supported by these photoresist spacers. Therefore, the 750 nm thick air cavity was formed. Subsequently, the hydrogel precursor solution was injected into the cavity at the edge of the cavity by using a pipette. The sample was cooled down on a cooling stage with a surface temperature of 5 °C, and then, was exposed to UV light (wavelength: 365 nm, intensity: 74 mW/cm²) for 5 s. The low-temperature exposure enabled enhancing optical transparency of the hydrogel. Lastly, the PET slab was peeled off and nonpolymerized residual monomer was removed by rinsing the sample with ethanol and water.

Optical spectra of the sample were measured using a spectroscopic measurement setup. The incident light was coupled from a 150 watts quartz halogen lamp using a multimode fiber and focused on to the BNAs by a 60× objective lens (NA = 0.85). A polarizer was inserted between the light source and the objective to control the polarization state of the excitation light.

Optical full wave simulation was carried out using a finite element method based commercial package COMSOL Multiphysics. The geometric parameters of the BNAs were extracted from the SEM image of the fabricated device. The curvature radius at the triangle apex was set to 14 nm. The glass substrate was considered to have an infinite thickness. The 25 nm thick ITO layer between the substrate and BNAs was also included in the model of the device.

To facilitate changing environmental temperatures, a microfluidic channel (1 mm wide, 750 μm high, and 15 mm long) was built on the top of the BNAs. To form the channel, a 100 μm thick glass coverslip (Sigma-Aldrich) was placed 750 μm above the BNAs with double sided adhesive as spacers. A photopatternable polymer solution consisting of isobornyl acrylate,

tetraethylene glycol dimethacrylate, and 2,2-dimethoxy-2-phenylacetophenone (all purchased from Sigma-Aldrich) with a weight ratio of 32:1.7:1.38 was injected into the chamber formed between the coverslip and the device surface using a pipette. A film photomask (Fineline Imaging) was used to define the patterns. The UV light intensity was set to 8.4 mW/cm². After 20 s exposure, the channel was developed by soaking the device in pure ethanol (Sigma-Aldrich) for 2 min, followed by baking on a hotplate at 60 °C for 1 hr. The inlet and outlet of the chambers were punched through the glass slides by using a conventional milling machine. Water with different temperatures were injected into the channel and flowed over the top surface of the device. The local temperature was monitored by a thermocouple probe (Omega HH506RA multilogger thermometer) placed in contact with the surface of the device.

3.5 Conclusions

In this work, we have demonstrated a temperature-responsive BNAs device by coating the plasmonic dimers with a submicron-thick thermos-responsive hydrogel. Upon the temperature variations, the water content of hydrogel varies due to the transition of hydrogel from hydrophobic to hydrophilic state and will gradually alter the refractive index of hydrogel. Because of the large field enhancement of the plasmonic modes in the BNAs, the spectra shift of resonances can indicate refractive index changes. The experiment results show that for the hydrogels-coated BNAs, a 16.2 nm of resonance shift was observed, compared to a 3 nm shift for the uncoated bare BNAs. Our study suggests a possibility of making environmental-sensitive plasmonic devices through the incorporation of coupled plasmonic nanostructures and environmental-responsive materials.

3.6 Acknowledgement

This work was supported in part by National Science Foundation under Grants # ECCS-0954765 and CCF-1331390, United State Agriculture Department under Grant # NIFA-2013-68004-20374, and Iowa State University's Plant Sciences Institute. P. L. and H. J. thank China Scholarship Council for partial financial support. S.O. thanks Turkish Council of High Education and Anadolu University in Turkey for financial support.

3.7 References

- [1] Zheludev, N. I. & Kivshar, Y. S. From metamaterials to metadevices. *Nature Materials* **11**, 917-924, doi:10.1038/NMAT3431 (2012).
- [2] Liu, A. Q., Zhu, W. M., Tsai, D. P. & Zheludev, N. I. Micromachined tunable metamaterials: a review. *Journal Of Optics* **14**, doi:10.1088/2040-8978/14/11/114009 (2012).
- [3] Pryce, I. M., Aydin, K., Kelaita, Y. A., Briggs, R. M. & Atwater, H. A. Highly Strained Compliant Optical Metamaterials with Large Frequency Tunability. *Nano Letters* **10**, 4222-4227, doi:10.1021/nl102684x (2010).
- [4] Tao, H. *et al.* Reconfigurable Terahertz Metamaterials. *Physical Review Letters* **103**, 147401, doi:10.1103/Physrevlett.103.147401 (2009).
- [5] Ou, J. Y., Plum, E., Jiang, L. & Zheludev, N. I. Reconfigurable Photonic Metamaterials. *Nano Letters* **11**, 2142-2144, doi:10.1021/n1200791r (2011).
- [6] Ou, J. Y., Plum, E., Zhang, J. F. & Zheludev, N. I. An electromechanically reconfigurable plasmonic metamaterial operating in the near-infrared. *Nature Nanotechnology* **8**, 252-255, doi:10.1038/nnano.2013.25 (2013).

- [7] Dicken, M. J. *et al.* Electrooptic Modulation in Thin Film Barium Titanate Plasmonic Interferometers. *Nano Letters* **8**, 4048-4052, doi:10.1021/nl802981q (2008).
- [8] Si, G. Y., Zhao, Y. H., Leong, E. S. P. & Liu, Y. J. Liquid-Crystal-Enabled Active Plasmonics: A Review. *Materials* **7**, 1296-1317, doi:10.3390/ma7021296 (2014).
- [9] Temnov, V. V. *et al.* Active magneto-plasmonics in hybrid metal-ferromagnet structures. *Nature Photonics* **4**, 107-111, doi:10.1038/Nphoton.2009.265 (2010).
- [10] Gagnon, G., Lahoud, N., Mattiussi, G. A. & Berini, P. Thermally activated variable attenuation of long-range surface plasmon-polariton waves. *Journal Of Lightwave Technology* **24**, 4391-4402, doi:10.1109/Jlt.2006.883683 (2006).
- [11] Roxworthy, B. J., Bhuiya, A. M., Yu, X., Chow, E. K. C. & Toussaint, K. C. Reconfigurable nanoantennas using electron-beam manipulation. *Nature Communications* **5**, doi:10.1038/Ncomms5427 (2014).
- [12] Tokareva, I., Minko, S., Fendler, J. H. & Hutter, E. Nanosensors based on responsive polymer brushes and gold nanoparticle enhanced transmission surface plasmon resonance spectroscopy. *Journal Of The American Chemical Society* **126**, 15950-15951, doi:10.1021/ja044575y (2004).
- [13] Tokarev, I., Tokareva, I. & Minko, S. Gold-nanoparticle-enhanced plasmonic effects in a responsive polymer gel. *Advanced Materials* **20**, 2730-2734, doi:10.1002/adma.200702885 (2008).
- [14] Sanchez-Iglesias, A. *et al.* Synthesis of multifunctional composite microgels via in situ Ni growth on pNIPAM-coated Au nanoparticles. *Acs Nano* **3**, 3184-3190, doi:10.1021/nn9006169 (2009).

- [15] Gehan, H. *et al.* Thermo-induced electromagnetic coupling in gold/polymer hybrid plasmonic structures probed by surface-enhanced raman scattering. *Acs Nano* **4**, 6491-6500, doi:10.1021/nn101451q (2010).
- [16] Joshi, G. K., Johnson, M. A. & Sardar, R. Novel pH-responsive nanoplasmonic sensor: controlling polymer structural change to modulate localized surface plasmon resonance response. *Rsc Advances* **4**, 15807-15815, doi:10.1039/c4ra00117f (2014).
- [17] Wang, Y., Brunsen, A., Jonas, U., Dostalek, J. & Knoll, W. Prostate Specific Antigen Biosensor Based on Long Range Surface Plasmon-Enhanced Fluorescence Spectroscopy and Dextran Hydrogel Binding Matrix. *Analytical Chemistry* **81**, 9625-9632, doi:10.1021/ac901662e (2009).
- [18] Toma, M., Jonas, U., Mateescu, A., Knoll, W. & Dostalek, J. Active Control of SPR by Thermoresponsive Hydrogels for Biosensor Applications. *Journal Of Physical Chemistry C* **117**, 11705-11712, doi:10.1021/jp400255u (2013).
- [19] Mesch, M., Zhang, C. J., Braun, P. V. & Giessen, H. Functionalized Hydrogel on Plasmonic Nanoantennas for Noninvasive Glucose Sensing. *Acs Photonics* **2**, 475-480, doi:10.1021/acsp Photonics.5b00004 (2015).
- [20] Jiang, H., Markowski, J. & Sabarinathan, J. Near-infrared optical response of thin film pH-sensitive hydrogel coated on a gold nanocrescent array. *Optics Express* **17**, 21802-21807, doi:10.1364/oe.17.021802 (2009).
- [21] Gehan, H. *et al.* Design and Optical Properties of Active Polymer-Coated Plasmonic Nanostructures. *Journal Of Physical Chemistry Letters* **2**, 926-931, doi:10.1021/jz200272r (2011).

- [22] Dong, L. & Jiang, H. Autonomous microfluidics with stimuli-responsive hydrogels. *Soft Matter* **3**, 1223-1230, doi:10.1039/b706563a (2007).
- [23] Mao, D. P., Liu, P. & Dong, L. Multichannel Detection Using Transmissive Diffraction Grating Sensor. *Journal Of Polymer Science Part B-polymer Physics* **49**, 1645-1650, doi:10.1002/polb.22365 (2011).
- [24] Karg, M. *et al.* Multiresponsive Hybrid Colloids Based on Gold Nanorods and Poly(NIPAM-co-allylacetic acid) Microgels: Temperature- and pH-Tunable Plasmon Resonance. *Langmuir* **25**, 3163-3167, doi:10.1021/la803458j (2009).
- [25] Karg, M. *et al.* L. M. Nanorod-coated PNIPAM microgels: Thermoresponsive optical properties. *Small* **3**, 1222-1229, doi:10.1002/sml.200700078 (2007).
- [26] Gupta, S., Agrawal, M., Uhlmann, P., Simon, F. & Stamm, M. Poly(N-isopropyl acrylamide)-Gold Nanoassemblies on Macroscopic Surfaces: Fabrication, Characterization, and Application. *Chemistry Of Materials* **22**, 504-509, doi:10.1021/cm9031336 (2010).
- [27] Sundaramurthy, A. *et al.* Field enhancement and gap-dependent resonance in a system of two opposing tip-to-tip Au nanotriangles. *Physical Review B* **72**, doi:10.1103/Physrevb.72.165409 (2005).
- [28] Kim, S. *et al.* High-harmonic generation by resonant plasmon field enhancement. *Nature* **453**, 757-760, doi:10.1038/nature07012 (2008).
- [29] Kinkhabwala, A. *et al.* Large single-molecule fluorescence enhancements produced by a bowtie nanoantenna. *Nature Photonics* **3**, 654-657, doi:10.1038/Nphoton.2009.187 (2009).

- [30] Suh, J. Y. *et al.* Plasmonic Bowtie Nanolaser Arrays. *Nano Letters* **12**, 5769-5774, doi:10.1021/nl303086r (2012).
- [31] Roxworthy, B. J. *et al.* Application of Plasmonic Bowtie Nanoantenna Arrays for Optical Trapping, Stacking, and Sorting. *Nano Letters* **12**, 796-801, doi:10.1021/nl203811q (2012).
- [32] Roxworthy, B. J. *et al.* Plasmonic Optical Trapping in Biologically Relevant Media. *Plos One* **9**, doi:10.1371/journal.pone.0093929 (2014).
- [33] Kuckling, D., Harmon, M. E. & Frank, C. W. Photo-cross-linkable PNIPAAm copolymers. 1. Synthesis and characterization of constrained temperature-responsive hydrogel layers. *Macromolecules* **35**, 6377-6383, doi:10.1021/ma0203041 (2002).
- [34] Richter, A. & Paschew, G. Optoelectrothermic Control of Highly Integrated Polymer-Based MEMS Applied in an Artificial Skin. *Advanced Materials* **21**, 979-983, doi:10.1002/adma.200802737 (2009).
- [35] Plunkett, K. N. *et al.* Leckband, D. E. PNIPAM chain collapse depends on the molecular weight and grafting density. *Langmuir* **22**, 4259-4266, doi:10.1021/la0531502 (2006).
- [36] Malham, I. B. & Bureau, L. Density Effects on Collapse, Compression, and Adhesion of Thermoresponsive Polymer Brushes. *Langmuir* **26**, 4762-4768, doi:10.1021/la9035387 (2010).
- [37] Dong, L., Agarwal, A. K., Beebe, D. J. & Jiang, H. R. Variable-focus liquid microlenses and microlens arrays actuated by thermoresponsive hydrogels. *Advanced Materials* **19**, 401-405, doi:10.1002/adma.200601561 (2007).
- [38] Stuart, M. A. C. *et al.* Emerging applications of stimuli-responsive polymer materials. *Nature Materials* **9**, 101-113, doi:10.1038/NMAT2614 (2010).

CHAPTER 4

NEMS-BASED INFRARED METAMATERIAL VIA TUNING NANOCANTILEVERS
WITHIN COMPLEMENTARY SPLIT RING RESONATORS

A paper published in Journal of Microelectromechanical Systems

Qiugu Wang, Depeng Mao, Peng Liu, Tomas Koschny, Costas M. Souklious, and Liang Dong

4.1 Abstract

Dynamic control of the electromagnetic properties of metamaterials requires wide modulation bandwidth. Tunable metamaterials with large tunability and fast speed are thus highly desirable. Due to the small dimensions, subwavelength meta-atoms or resonant elements that constitute a metamaterial in the mid-to-near-infrared (IR) wavelength range are often not easy to be tuned at a high rate of several tens of megahertz (MHz). Here, we report on a nanoelectromechanical systems (NEMS)-based tunable IR metamaterial realized by unique embedding of nanocantilevers into complementary split ring resonators (c-SRRs) suspended over individual wells. The optical field confined in the air gap of the c-SRR is strongly influenced by electrostatically induced mechanical deflection of the nanocantilever, thus modulating the reflection spectrum of the metamaterial. With the easy-to-implement tunable meta-atom design, the IR metamaterial with 800 nm-long cantilevers provides an ultrahigh mechanical modulation frequency of 32.26 MHz for optical signal modulation at a wavelength of 2.1 μm and is rather easy to manufacture and operate. We envision a compact, efficient, and high-speed electro-optic modulation platform in the IR region using this tunable metamaterial technology.

4.2 Introduction

Metamaterials are artificially-engineered resonant structures that can be used to manipulate electromagnetic (EM) waves on subwavelength scales. They are promising for a variety of applications such as superlenses [1, 2], invisibility cloaks [3, 4], perfect absorbers [5,

6], and biochemical sensors [7-9]. The ever-increasing demand for active control of the EM properties of metamaterials has led to the development of tunable metamaterials [10], which are mainly realized by hybridizing meta-atoms or resonant elements with nonlinear materials such as phase-change media [11-13], liquid crystals [14-17] and semiconductors [18-20]. Alternatively, the microsystems technology has also enabled the realization of tunable metamaterials [21] by using thermally-actuated bimorph beams [22-25] and in-plane electrostatic comb drives [26-29]. This type of tunable metamaterials can be realized via the complementary-metal-oxide-semiconductor (CMOS) fabrication process to enable flexible control with integrated circuits [21]. Nevertheless, both the optical resonance wavelength and mechanical modulation frequency of these metamaterials are usually limited by the relatively large size of the tunable meta-atoms. For example, tunable near-infrared (IR) metamaterial-based absorbers [30, 31] have recently been developed via constructing diffractive nanohole gratings on a diaphragm with dimensions of hundred microns. They rely on sophisticated CMOS-compatible fabrication processes but only have modulation frequencies of the order of kilohertz. In order to improve the modulation frequency, multiple pairs of tens-of-microns-long metallic strings were previously arranged in parallel, and electrostatic [32] or optical [33] forces were applied to control nanoscale strip displacements at a rate of 1-2 MHz. Despite these efforts, tuning metamaterials at a rate of several tens of MHz in the near-IR and shorter-wavelength spectral region remains very challenging. Here, we report on a nanoelectromechanical systems (NEMS)-based reconfigurable metamaterial operating in the near-to-mid-IR region which affords ultrafast electro-optic modulation and is rather easy to fabricate and operate.

4.3 Device Structure and Principle

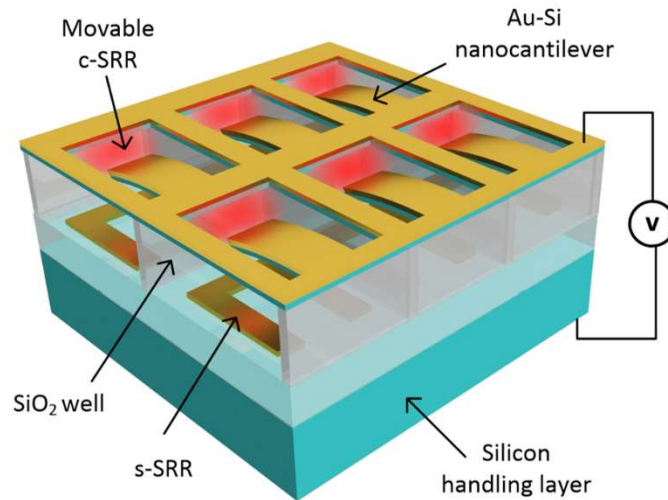


Figure 4.1 Schematic of the NEMS-enabled tunable metamaterial operating in the near-to-mid-IR wavelength region.

Fig. 4.1 schematically illustrates the working principle of the proposed metamaterial. The metamaterial is composed of an array of gold–silicon (Au–Si) bilayer complementary split ring resonators (c-SRRs) at the top and an array of Au solid SRRs (s-SRRs) at the bottom of SiO₂ wells. The c-SRR has an inverse shape to the s-SRR. An in-plane cantilever is embedded in the c-SRR and surrounded by a 200 nm-wide U-shaped air gap. The top c-SRRs are positioned 250 nm above the bottom of the SiO₂ well formed in a 1 μm-thick buried SiO₂ layer of a silicon-on-insulator (SOI) substrate. The cantilever is composed of 20 nm-thick Si and 20 nm-thick Au layers. One end of the cantilever is anchored while the other end is free to move. The cantilever is 800 nm long and 500 nm wide. The entire top Au layer serves as an electrode, while the Si handling layer of the SOI substrate is the other electrode of an electrostatic actuator. Depending on the polarization direction of incident light, different eigenmodes of the c-SRR or s-SRR structures of the metamaterial can be excited. When a voltage is applied between the top Au and bottom Si handling layers, the generated electrostatic force bends the embedded nanocantilever

towards the bottom of the SiO₂ well. The electrostatically induced mechanical deflection of the nanocantilever changes the shape of the U-shaped air gap, thus allowing tuning of the characteristics of the optical resonant modes of the c-SRR or s-SRR. Profoundly, due to the compact design and small dimensions of the nanocantilever, the proposed metamaterial can be synchronously driven at modulation frequencies up to several tens of MHz to tune its reflection spectrum in the IR region, thus providing much faster electro-optic modulation than many other counterpart metamaterials [26-34]. Note that in this paper subwavelength meta-atoms refer to the c-SRR or s-SRR resonant units shown in Fig. 4.1.

4.4 Methods

4.4.1 Metamaterial Fabrication

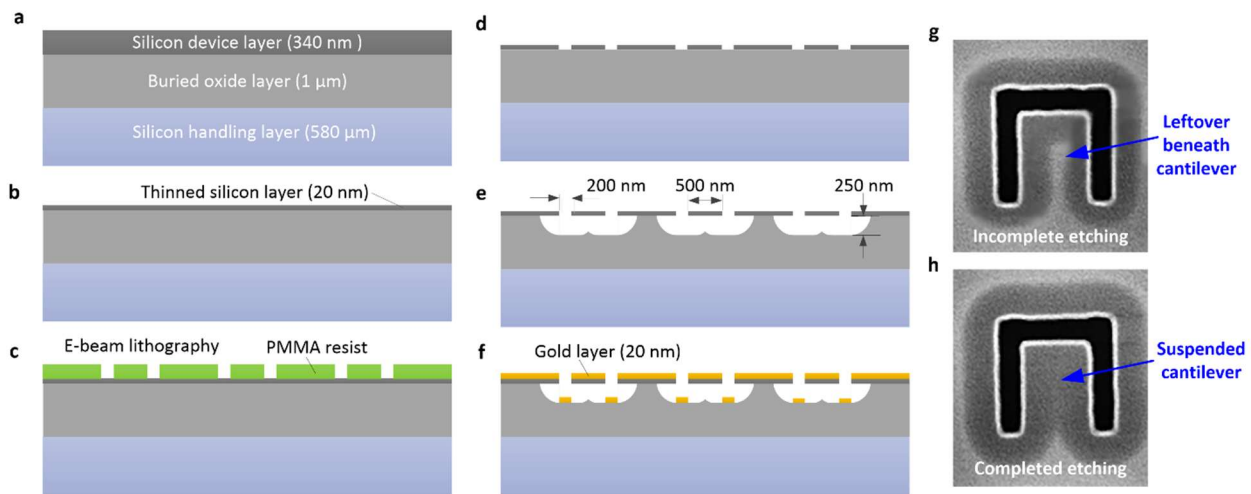


Figure 4.2. (a)-(f) Schematic of the fabrication process for the tunable IR metamaterial. (g)-(h) SEM images showing an unreleased cantilever after BOE etching of buried oxide for 3.5 min (g), and a released cantilever after BOE etching of oxide for 5 min. The length of the cantilever in (g) and (h) is 800 nm.

The metamaterial design was implemented on a SOI wafer. Fig. 4.2 shows the schematic of the fabrication process for the metamaterial. The SOI wafer consisted of a 340-nm-thick device silicon layer, a 1- μ m-thick buried oxide layer, and 580- μ m-thick handling silicon wafer (Fig. 4.2(a)). First, the top silicon layer of the SOI substrate was thinned down to \sim 20 nm by

thermal oxidation, with subsequent wet-etching of SiO₂ using a buffered oxide etch (BOE) solution (Fig. 4.2(b)). Subsequently, the thinned silicon layer was doped with phosphorous ions ($5 \times 10^{19} \text{ cm}^{-3}$) to increase electrical conductivity for serving as a top electrode. U-shaped air gaps were then patterned in the thinned silicon layer by means of e-beam lithography (Fig. 4.2(c)) and subsequent reactive-ion etching of silicon (Fig. 2(d)); thus, the patterns of the nanocantilever array were formed. Next, the wafer was immersed into the BOE solution for 5 min to totally remove the SiO₂ underneath the nanocantilevers, while retaining most of the SiO₂ underneath the frame structure between neighbouring c-SRRs (Fig. 4.2(e)). This design prevented possible collapse of the entire metamaterial surface under an applied voltage. Finally, a ~ 20 -nm-thick Au thin film was evaporated onto the surface of the device through evaporation. Thus, the Au/Si c-SRRs on the top and Au solid SRRs at the bottom of the air cavities were formed (Fig. 4.2(f)). The resulting vertical separation between the c-SRRs and SRRs was ~ 250 nm. Fig. 4.2(g) and (h) show the unreleased and released cantilever after BOE etching of the buried oxide for 3.5 min and 5 min, respectively.

4.4.2 Numerical Simulation

Optical simulations were carried out using finite-element-method-based software (COMSOL Multiphysics). The geometrical parameters used in the simulations were extracted from the SEM images of the fabricated device. In the simulations, the thick handling Si layer of the SOI substrate was not included in the computed region due to limited computation power. For simplicity, the rounded 90-degree corners and geometrical irregularities of the fabricated c-SRRs occurring in the experiments were not considered.

4.4.3 Electro-optical Characterization

The reflection spectra of metamaterials were measured via the Fourier transform IR (FTIR) microscope system (Hyperion 2000, Bruker) for normal incidence of light. Transverse

magnetic (TM) and transverse electric (TE) polarizations were obtained using the built-in polarizers of the FTIR microscope. A D.C. voltage was applied between the gold-coated top surface of the device and the silicon handling layer of the SOI wafer to electrostatically tune the metamaterials during the reflection spectra measurement.

Electro-optical modulation of the metamaterials was conducted by measuring the reflectance change in a 2.1 μm laser beam (Ho: YAG end-pump laser) reflected from the metamaterials, while modulating the metamaterial with a function generator (FG; Agilent 81101A) and a voltage amplifier. The reflected laser beam was detected by an InGaAs photodetector (818-BB-51, Newport) and a lock-in amplifier (SR830, Stanford Research). The whole optical setup for the electro-optical modulation is displayed in the Results and Discussion section.

4.5 Results and Discussion

Fig. 4.3 shows the SEM images of the metamaterial before and after gold coating at the surface of the device. Fig. 4.4(a) presents the measured and simulated optical reflection spectra of the metamaterial under TM and TE polarizations when no voltage is applied to the metamaterial. Conspicuous resonance dips are observed at different wavelengths. In general, when the incident field is polarized along the parallel (TM) or perpendicular (TE) directions to their gaps, odd or even eigenmodes will be excited for SRRs [35]. In contrast, even or odd eigenmodes of c-SRRs will be excited by TM- or TE-polarized fields, respectively. Therefore, for TM polarizations (Fig. 4.4(a); left panel), one even c-SRR mode and two odd s-SRR resonance modes appear as reflectance dips. Here we mark these resonance modes with '1^S' at a wavelength of 6.8 μm , '3^S' at 3.3 μm , and '2^C' at 2.1 μm in the spectrum, where the superscripts 'S' and 'C' denote the modes of the s-SRR and c-SRR, respectively. The origins of these

resonances are unveiled by the computed field distributions in Fig. 4.4(c), where the orders of eigenmodes can be defined by the number of nodes in the electric- or magnetic-field component normal to the surface of the s-SRR or c-SRR structure [35, 36].

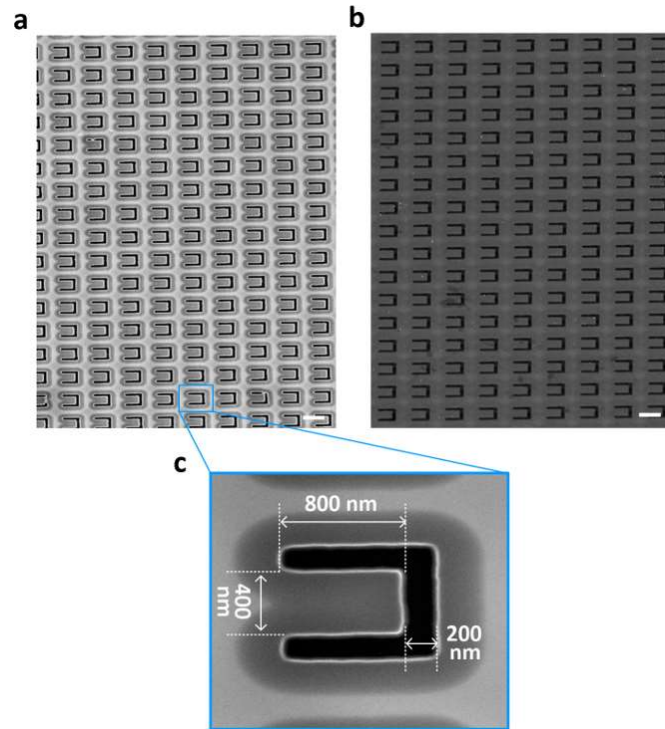


Figure 4.3 SEM images of the metamaterial before (a) and after (b) coating with a 20 nm-thick Au layer. The scale bars represent 1 μm . In (a), the cantilevers are released. In (b), the metamaterial is formed. A closed-up of the c-SRR without an Au layer is displayed in (c).

For TE polarizations, two odd-order c-SRR resonances (1^{C} at 5.3 μm and 3^{C} at 2.5 μm) are excited (Fig. 4.4(a); right panel), as confirmed by the magnetic field distributions in Fig. 4.4(b). However, no distinct resonance dip associated with an even-order s-SRR resonance is observed. Actually, an asymmetric Fano line shape is exhibited near mode 3^{C} . This originates from the plasmon mode overlap between modes 2^{S} and 3^{C} , as confirmed by the electric field distribution of mode 2^{S} in Fig. 4.4(d), where two amplitude nodes of the electric field are observed. It is worthy to note that no obvious coupling is observed between 1^{C} or 1^{S} modes. This is because the s-SRRs are formed with the use of the c-SRRs as shadow masks during deposition

of the Au layer, the s-SRRs and c-SRRs are identically shaped and orientated as a solid-inverse structure [37].

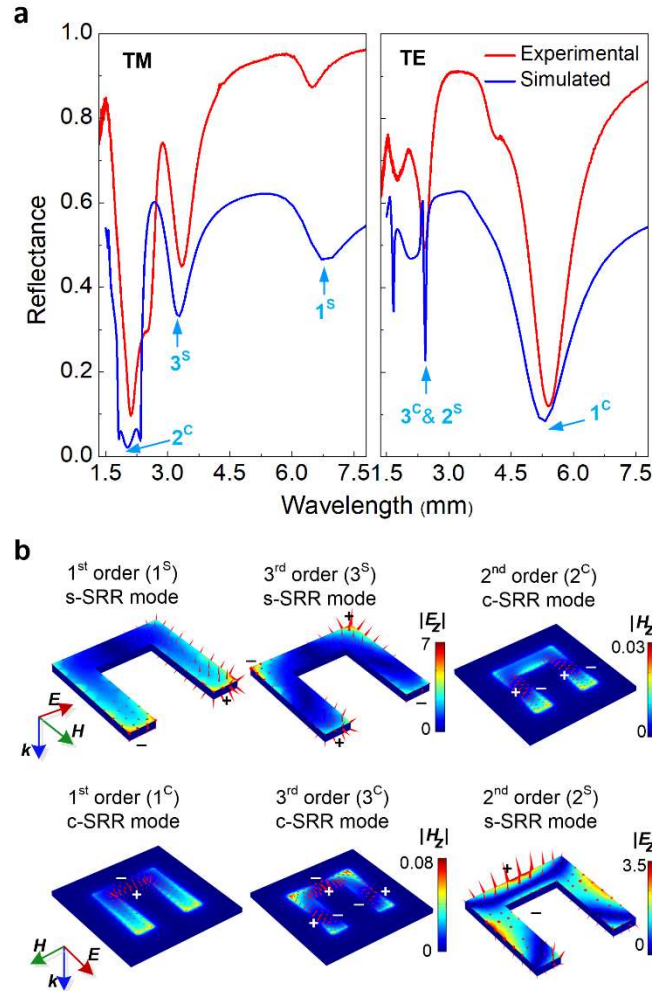


Figure 4.4 (a) Measured and simulated reflection spectra of the metamaterial under TM and TE polarizations. Notations 1^S-3^S and 1^C-3^C represent the different orders of the s-SRR and c-SRR modes, respectively. (b) Simulated field distributions of c-SRR and s-SRR modes. The intensity of incident electric field is $E_0 = 1$ V/m. The units of the electric field strength (E_z) and magnetic field strength (H_z) are V/m and A/m, respectively. The arrows in the field distributions denote the electric field, where their directions indicate the vector directions of surface currents.

It should be noted that the discrepancies between the simulated and experimental results may be caused by the imperfection of the simulation model. The modeling accuracy mainly depends on how accurate the extracted geometric parameters of the c-SRR and s-SRR are. The

geometric errors of the model influence the optical resonances of the device, particularly more significant for high-order resonances. The removal of the handling Si layer of the SOI substrate from the limited computed region also impacts the reflection intensity. In addition, due to the nanofabrication, the inevitable non-uniformity of the fabricated meta-atoms may be another cause of the discrepancies between the simulated and experimental spectra. Nevertheless, the simulations still provide a useful prediction in the wavelengths and line shapes of the resonances that help us to identify the origin of the resonance modes.

We now discuss the influence of applied voltage on the resonance characteristics for the major resonance modes of the metamaterial. As shown in Fig. 4.5(a) and (b), as the voltage increases from 0 to 55 V, the reflectance dips, assigned to the 1^C , 2^C , and 3^C modes, all exhibit positive changes consistently. The changes of optical signals are caused by the bending of nanocantilevers that change the shapes of c-SRRs. In order to highlight the voltage induced variations, we plot in Fig. 4.5(c) and (d) the relative changes in reflectance at different voltages: $\Delta R/R_0 = (R - R_0)/R_0$, where R and R_0 represent the reflection intensities at a given voltage and no voltage, respectively. Here one can see that the spectra of $\Delta R/R_0$ show peak-like features. As voltage increases, all the c-SRR modes exhibit a positive change in reflectance. For example, when the applied voltage increases from 0 V to 55 V, the reflectance at the 2^C mode progressively increases from 9.8% to 13.5% (Fig. 4.5(a)). This corresponds to a relative reflectance change of $\Delta R/R_0 = 38\%$ (Fig. 4.5(c)). Accordingly, the values of $\Delta R/R_0$ at the 1^C and 3^C modes are 15% and 5% respectively when applying a voltage of 55 V (Fig. 4.5(d)).

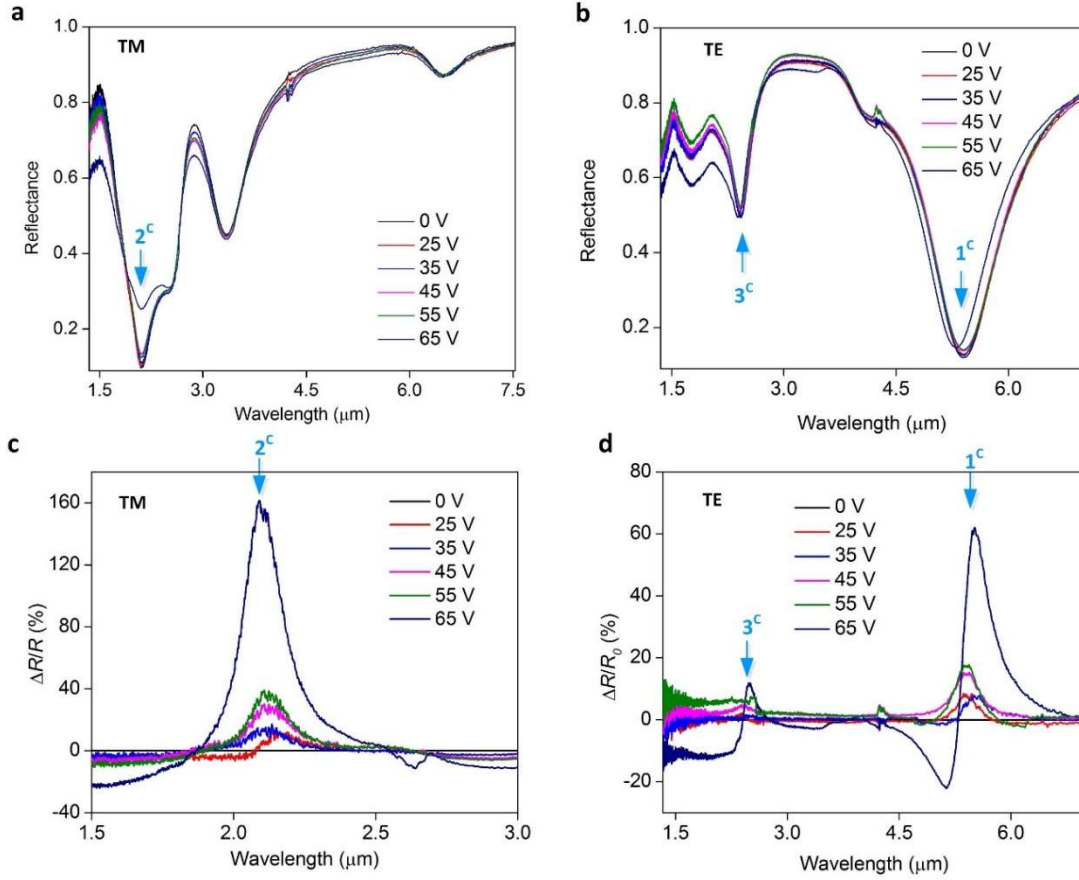


Figure 4.5 NEMS-enabled tuning of spectral characteristics of the metamaterial using 0.8 μm -long cantilevers. (a, b) Reflection spectra for different applied voltages under TM (a) and TE (b) polarizations. At 65 V, the cantilevers of the metamaterial are in the pull-in state. (c, d) Spectra of relative reflectance change $\Delta R/R_0$ for different applied voltages under TM (c) and TE (d) polarizations.

At higher voltages, the pull-in effect of the nanocantilever occurs due to the strongly nonlinear increase in the electrostatic force, thus causing abrupt deflection and stiction of the nanocantilever to the bottom of the SiO_2 well. The pull-in voltage V_P for a bilayer nanocantilever beam with dimensions of L (length) \times w (width) \times t (thickness) can be estimated using the following equation [38, 39]:

$$V_P = \sqrt{8k_{\text{eff}}(d + t_{\text{oxide}}/\epsilon_r)^3 / (27\epsilon_0 wL)} \quad 4.1$$

where k_{eff} represents the effective stiffness of the nanocantilever, $d = 250$ nm the distance between the nanocantilever and the bottom of the well, $t_{\text{oxide}} = 750$ nm is the thickness of the remaining SiO_2 layer at the bottom of the well, $\epsilon_r = 3.9$ is the dielectric constant of SiO_2 , and ϵ_0 is the permittivity of vacuum. For the given design parameters of $L = 800$ nm, $w = 500$ nm, and $t = 40$ nm, the calculated pull-in voltage was $V_p = 66$ V, which is close to the experimental result of 65 V. In the pull-in state of the nanocantilevers, the reflectance of the metamaterial at the $2C$ mode dramatically increases to 25.5% (Fig. 4.5(a)) and thus the corresponding value of $\Delta R/R_0$ reaches 160% (Fig. 4.5(c)).

In Fig. 4.6(a), we summarize the reflection intensity modulations for the resonance modes of the metamaterial for different applied voltages. Here one can see that, when applying voltages, the even-order (2^C) c-SRR modes exhibit more significant changes in reflectance than odd-order modes (1^C and 3^C). As the s-SRR structure is unchanged, only minor reflectance changes are observed. For example, the 1^S mode of s-SRR is hardly influenced by the applied voltage and the 3^S mode exhibits only a 3% reduction in $\Delta R/R_0$.

To understand the changes of the c-SRR modes caused by the deflection of the nanocantilever, we computed the field distributions corresponding to the 1^C , 2^C , and 3^C resonance modes under different nanocantilever bending conditions, as shown in Fig. 4.6(b). The incident EM field leads to currents flowing in opposite directions on the concave and convex surfaces of the nanoapertures, thus forming a waveguide mode inside the nanoaperture [40]. Alternatively, the c-SRR resonances can essentially be understood as Fabry–Pérot resonances of guided waves propagating perpendicular to the nanoaperture [36]. The widening gap of the nanoaperture under an applied voltage leads to blue-shift of the resonance wavelength and reduced reflection intensity, owing to weakened near-field interactions around the sidewalls of

nanoaperture. The even-order c-SRR modes are more sensitive to the shape change of the nanoaperture compared to the odd-order modes. A plausible explanation for this observation is given below. The field strength is the highest at the amplitude node.

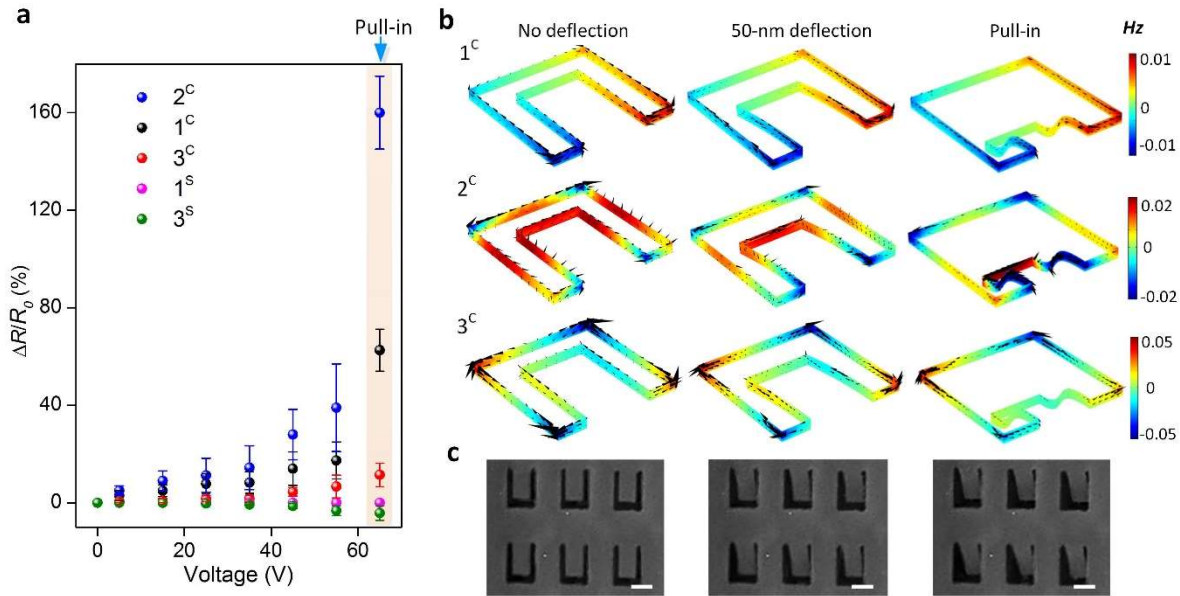


Figure 4.6 Effect of applied voltage on resonance modes and field distributions. (a) Summary of the relative changes in reflection intensity for different c-SRR and s-SRR modes as functions of the applied voltage. (b) Magnetic field distributions in the 1^C–3^C modes on the sidewalls of the air nanoaperture under the initial state (left column), with 50 nm deflection (middle column), and the pull-in state (right column) of the nanocantilever. The arrows in the field distributions indicate the vector directions of surface currents. (c) SEM photographs of the metamaterial in the three states shown in (b). The scale bars present 500 nm.

For the odd-order modes, the current flow starts at the front sidewall of the nanocantilever and ends at the opposite surface across the gap. The magnetic field intensities at these surfaces are low (close to zero). In contrast, for the even-order modes, the current flow starts and ends at the corners of the nanoaperture, and thus, the front sidewall of the nanocantilever serves as one of the amplitude nodes, where the nanocantilever has strong near-field interactions with its opposite surface. As a result, these even-order modes are more sensitive to changes of the nanoaperture size. As shown in Fig. 4.6(b), a 50 nm deflection at the

tip of the nanocantilever causes significant changes in the current and magnetic field density in the 2^C mode at the front sidewall of the nanocantilever, whereas very little change is observed in the 1^C and 3^C modes. In the pull-in state, both 1^C and 3^C c-SRR modes still exist but are insensitive to the deflection of the nanocantilever, as confirmed by the EM simulation.

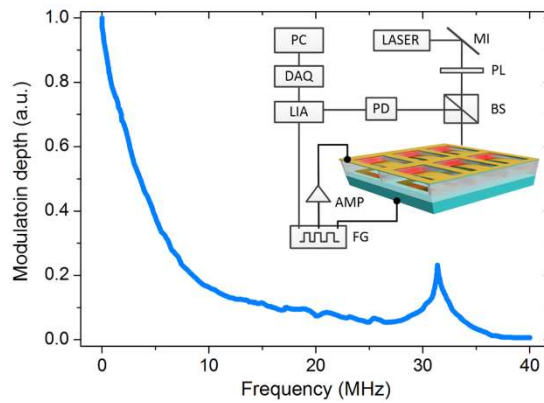


Figure 4.7 Normalized modulation depth of the tunable metamaterial as a function of driving frequency. The metamaterial utilizes $0.8 \mu\text{m}$ -long cantilevers. The inset illustrates the setup. MI – mirror; PL – polarizer; BS – beam splitter; PD – photodetector; LIA – lock-in amplifier; DAQ – data acquisition; FG – function generator; AMP – amplifier; PC – personal computer.

Following the above discussions of the device tunability, we examine the electro-optical modulation of the IR metamaterial. As illustrated in the inset of Fig. 4.7, a $2.1 \mu\text{m}$ -wavelength laser beam in mode 2^C was made normally incident on the metamaterial. A square-wave driving voltage switching between 0 and 55 V was applied to the metamaterial. The incident laser beam was thus modulated by the metamaterial, and the reflected light was detected by a photodetector. Fig. 4.7 shows the frequency dependences of electro-optic modulation for the metamaterial. The spectral responses exhibit an initial roll-off until 10 MHz and the mechanical resonance frequency exhibits at 32.26 MHz, which agrees well with the simulated frequency of 31.35 MHz. Here, the normalized modulation depth at the mechanical resonance frequency is 24% (Fig. 4.7), in which the reflectance obtained at the mechanical resonance frequency of 31.35 MHz is normalized to the one obtained at 55 V DC input. The absolute modulation depth can be

calculated as $(1+0.24) \times (\Delta R/R_0) = 1.24 \times 38\% = 47\%$, where $\Delta R/R_0 = 38\%$ is the relative reflectance change at the 2^C resonance mode of the metamaterial (Fig. 4.5(c)). This result indicates that the metamaterial can be driven to its fundamental resonance frequency.

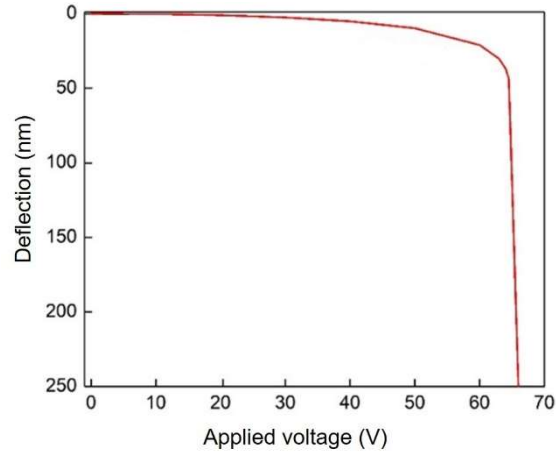


Figure 4.8 Simulated mechanical deflection of the cantilevers with the length of $0.8 \mu\text{m}$ under various applied voltages.

Note that in the electro-optic modulation experiment where a square-wave voltage switching between 0 and 55 V was applied, no stiction was observed. To explain the fact, mechanical simulations of cantilever deflections under various applied voltages are presented in Fig. 4.8. The result shows the deflection of the cantilever increases slowly below the pull-in voltage, but changes drastically when the voltage approaches the pull-in voltage. For the 800 nm-long cantilevers, the pull-in voltage is 65 V. Note that the air cavity beneath the cantilever is 250 nm deep. At 55 V, the deflection (see the red curve in Fig. 4.8) is ~ 20 nm and is insufficient to cause any stiction.

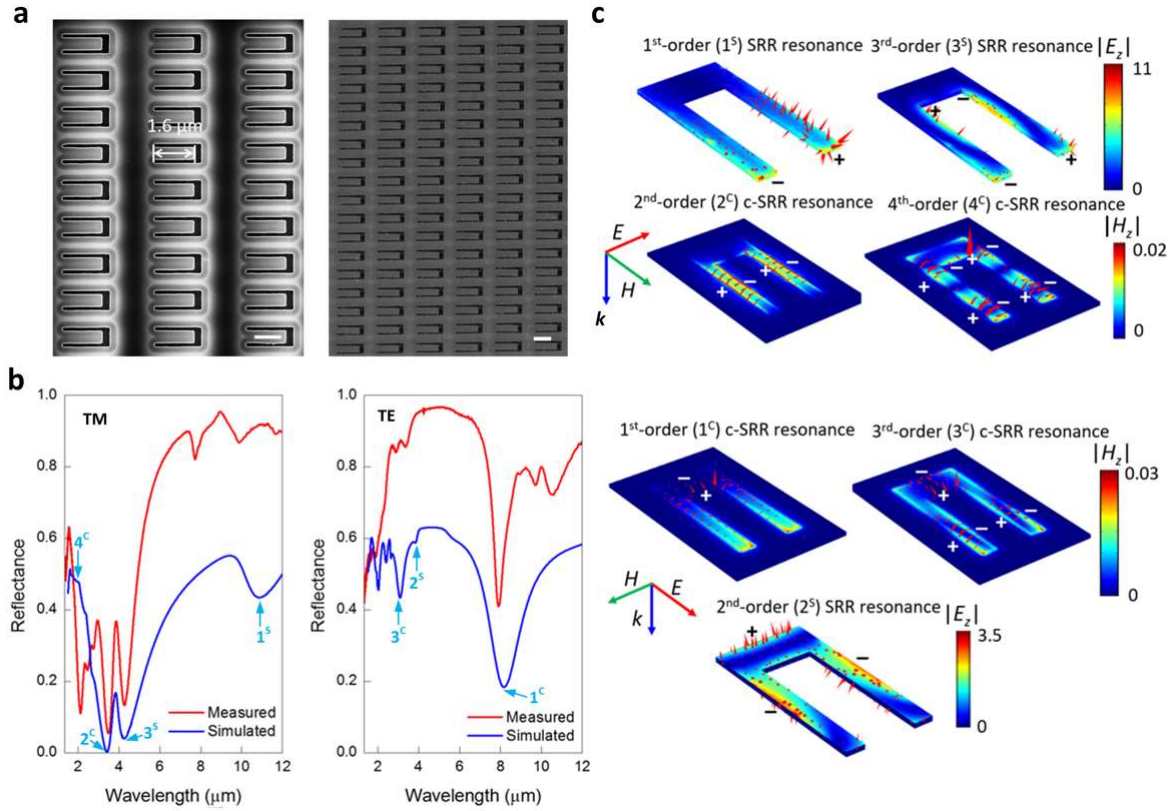


Figure 4.9 Tunable metamaterial using 1.6- μm -long cantilevers. (a) SEM photographs of the metamaterial with 1.6- μm -long cantilevers before (left) and after (right) coating of Au layer. The scale bars represent 1 μm . (b) Measured and simulated reflection spectra of the metamaterial for TM (left) and TE (right) polarizations. Notations 1^S–3^S and 1^C–4^C indicate the different orders of the s-SRR and c-SRR modes, respectively. (c) Simulated field distributions of the c-SRR or SRR resonance modes. The intensity of incident electric field is $E_0 = 1$ V/m. The units of the electric field strength (E_z) and magnetic field strength (H_z) are V/m and A/m, respectively. The arrows in the field distributions indicate the electric field, where their directions indicate the phase relation.

In essence, the electro-optic effect of the tunable metamaterial shown in Fig. 4.7 originates from the electrostatically induced mechanical deformation of the c-SRRs, affecting the effective refractive index of each optical resonant element and thus the resonance characteristics of the metamaterial. In contrast, conventional electro-optic materials such as electrified crystals often have millimetre-scale dimensions and use birefringence-induced polarization effects with the aid of polarizers [41]. Meanwhile, liquid-crystal-based electro-optic modulators [15, 42, 43] provide slow responses due to the slow reorientation process of the liquid-crystal molecules,

which limits their modulation frequency. In contrast, via constructing c-SRRs with free-standing Au-Si nanocantilevers at the subwavelength scale, we can tune the optical resonances of the formed metamaterials to modulate the incident waves by applying an electrical potential. The complementary structural feature of the optical resonators also simplifies the nanomanufacturing processes and the driving method for electro-optic modulations in the near-to-mid-IR spectral regime. Further, the resulting small dimensions of the meta-atoms lead to high mechanical resonance frequencies of the order of several tens of MHz, i.e. one to three order of magnitude higher than almost all existing reconfigurable metamaterials [21-29]. An optomechanical dielectric metamaterial [44] was recently reported to exhibit a higher modulation frequency; however, owing to the weak optical force, the metamaterial provided a limited maximum modulation depth of 0.2% (normalized value) [44]. In comparison, our metamaterial, when operating at its mechanical resonance frequency, offers the normalized modulation depth of 24% (Fig. 4.7), about two orders of magnitude higher than the metamaterial using the optical force [44]. This is because the electrostatic actuation method used in our device allows larger deflections of the cantilever than the optomechanical actuation method.

Although the nanocantilever stiction at pull-in is irreversible due to van der Waals interactions, the stiction could be avoided by some methods such as using closed-loop control and proper surface treatment to extend the range of travel for the nanocantilever [39]. In addition, to achieve larger tunability of the EM resonances with lower driving voltages, design improvements can be made. Possible optimization includes introducing appropriate structural symmetry breaking between the c-SRR and s-SRR structures to generate stronger coupled resonances in their fundamental modes [37, 45-47], thus improving resonance sensitivity of the cantilever deflection. The symmetry breaking could be achieved via formation of overlapping

shadow areas between the c-SRR and SRR. Moreover, it is flexible to adjust optical resonance wavelengths of the metamaterial by adjusting the geometries and dimensions of nanoapertures and cantilevers. For example, Fig. 4.9(a) shows the metamaterial with 1.6 μm -long cantilevers embedded in the c-SRRs. The resonance wavelength of the 2^{C} c-SRR mode for this metamaterial redshifts to a longer wavelength at 3.41 μm (Fig. 4.9(b); left panel), compared to the mode wavelength of 2.1 μm for the above-mentioned metamaterial using 0.8 μm -long cantilevers. Similarly, to identify the origins of the resonance dips displayed in Fig. 4.9(b), we computed the field distributions of the c-SRR or SRR resonance modes in Fig. 4.9(c).

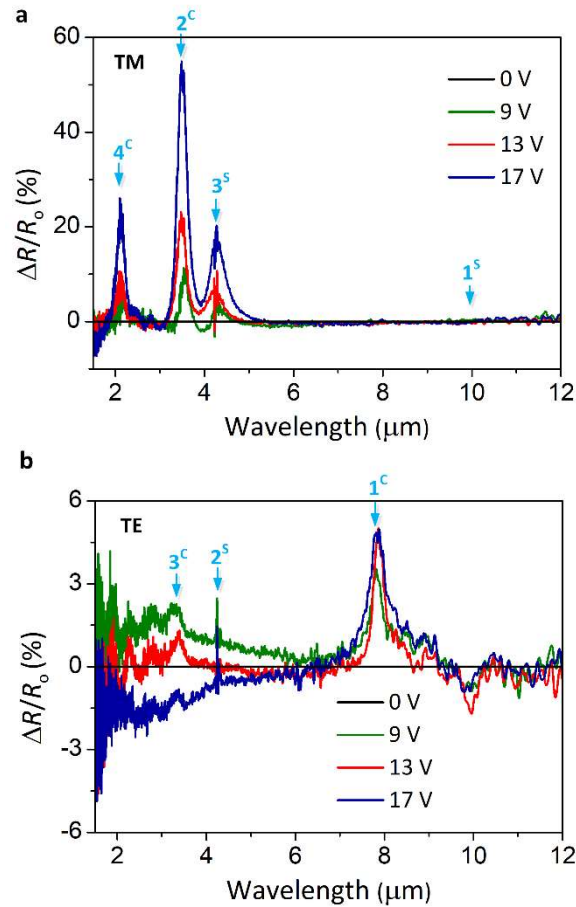


Figure 4.10 Spectra of relative reflectance change $\Delta R/R_0$ of the tunable metamaterial using 1.6 μm -long cantilevers for TM (a) and TE (b) polarizations under different applied voltages. The voltages applied here are below the 20.5 V pull-in voltage of the embedded cantilever.

Further, Fig. 4.10 shows the TE and TM spectra for the relative reflectance change $\Delta R/R_0$ of the metamaterial with 1.6 μm -long cantilevers under different applied voltages before the pull-in effect occurs at 20.5 V. As expected, with increasing applied voltages from 0 to 17 V, the 1^{C} and 3^{C} c-SRR modes for TE polarizations and the 1^{S} s-SRR mode for TM polarizations exhibit relatively low sensitivities to the applied voltages. The maximum value of $\Delta R/R_0$ is found to be 58% at the 2^{C} mode at 17 V (Fig. 4.10). The electro-optic modulation experiment indicates that due to the longer cantilevers embedded in the c-SRR structures, this metamaterial exhibits a lower mechanical modulation frequency of 5.32 MHz, compared to the above-described one using 0.8 μm -long cantilevers (i.e., 32.26 MHz).

Lastly, it should be noted that in this design, the length of the Au-coated cantilevers should be no more than 3 μm to avoid significant initial bending. Fig. 4.11 shows that when the metamaterial has 3 μm -long cantilevers, even in the absence of voltage application the thin cantilevers (20-nm-thick silicon and 20 nm-thick gold) are already bent into the wells, perhaps owing to the initial stress of the cantilevers.

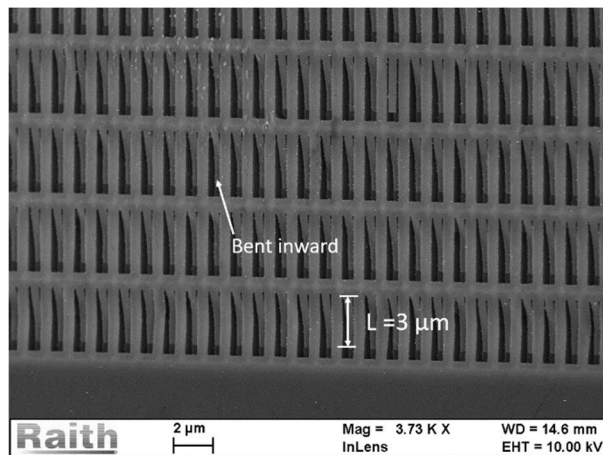


Figure 4.11 SEM photo of the metamaterial with 3- μm -long cantilevers.

4.6 Conclusions

In summary, we have demonstrated the NEMS-enabled tunable metamaterials operating in the near-to-mid-IR range by electromechanically tuning the nanocantilevers embedded in the c-SRR units. As the nanocantilevers bend downward towards the substrate, the U-shaped air gaps in the c-SRRs are geometrically changed, thus altering the surface-current flows on the sidewalls of the nanoapertures and varying the resonance intensity. The deflection of the nanocantilevers leads to significantly larger changes in the even c-SRR modes, while this change is less impactful in the odd c-SRR and SRR modes. With the compact and easy-to-implement meta-atom design, the present tunable metamaterial can provide fast electro-optic modulation at frequencies of several tens of MHz. In addition, this technology will find many applications in optical modulators, infrared sensors [48], and transformation optics [49]. Our tunable metamaterial design may also shed a light on a reconfigurable metamaterial where each resonant element may be individually controlled via integration of CMOS based integrated circuits within the top silicon device layer of SOI substrate.

4.7 Acknowledgement

The authors thank the Microelectronics Research Center at the Iowa State University, Ames, Iowa, and the Minnesota Nano Center at the University of Minnesota, Twin City, MN, for semiconductor fabrication facilities, and Dr. Siming Yang, Prof. Jiming Song, Prof. Robert J. Weber, and Prof. Zhe Fei for their helpful discussions.

4.8 References

- [1] Fang, N., Lee, H., Sun, C. & Zhang, X. Sub-diffraction-limited optical imaging with a silver superlens. *Science* **308**, 534-537, doi:10.1126/science.1108759 (2005).

- [2] Smolyaninov, I., Hung, Y. J. & Davis, C. C. Magnifying superlens in the visible frequency range. *Science* **315**, 1699-1701, doi:10.1126/science.1138746 (2007).
- [3] Schurig, D. *et al.* Metamaterial electromagnetic cloak at microwave frequencies. *Science* **314**, 977-980, doi:10.1126/science.1133628 (2006).
- [4] Yang, S. *et al.* From Flexible and Stretchable Meta-Atom to Metamaterial: A Wearable Microwave Meta-Skin with Tunable Frequency Selective and Cloaking Effects. *Scientific Reports* **6**, 21921, doi:10.1038/srep21921 (2016).
- [5] Landy, N. I., Sajuyigbe, S., Mock, J. J., Smith, D. R. & Padilla, W. J. Perfect metamaterial absorber. *Physical Review Letters* **100**, 207402, doi:10.1103/PhysRevLett.100.207402 (2008).
- [6] Liu, N., Mesch, M., Weiss, T., Hentschel, M. & Giessen, H. Infrared Perfect Absorber and Its Application As Plasmonic Sensor. *Nano Letters* **10**, 2342-2348, doi:10.1021/nl9041033 (2010).
- [7] Kabashin, A. V. *et al.* Plasmonic nanorod metamaterials for biosensing. *Nature Materials* **8**, 867-871, doi:10.1038/NMAT2546 (2009).
- [8] Pryce, I. M., Kelaita, Y. A., Aydin, K. & Atwater, H. A. Compliant Metamaterials for Resonantly Enhanced Infrared Absorption Spectroscopy and Refractive Index Sensing. *Acs Nano* **5**, 8167-8174, doi:10.1021/nn202815k (2011).
- [9] Xu, X. L. *et al.* Flexible Visible-Infrared Metamaterials and Their Applications in Highly Sensitive Chemical and Biological Sensing. *Nano Letters* **11**, 3232-3238, doi:10.1021/nl2014982 (2011).
- [10] Zheludev, N. I. & Kivshar, Y. S. From metamaterials to metadevices. *Nature Materials* **11**, 917-924, doi:10.1038/NMAT3431 (2012).

- [11] Seo, M. *et al.* Active Terahertz Nanoantennas Based on VO₂ Phase Transition. *Nano Letters* **10**, 2064-2068, doi:10.1021/nl1002153 (2010).
- [12] Driscoll, T. *et al.* Dynamic tuning of an infrared hybrid-metamaterial resonance using vanadium dioxide. *Applied Physics Letters* **93**, 024101, doi:10.1063/1.2956675 (2008).
- [13] Wang, Q. G. *et al.* Tunable Optical Nanoantennas Incorporating Bowtie Nanoantenna Arrays with Stimuli-Responsive Polymer. *Scientific Reports* **5**, 18567, doi:10.1038/Srep18567 (2015).
- [14] Minovich, A., Neshev, D. N., Powell, D. A., Shadrivov, I. V. & Kivshar, Y. S. Tunable fishnet metamaterials infiltrated by liquid crystals. *Applied Physics Letters* **96**, 193103, doi:10.1063/1.3427429 (2010).
- [15] Shrekenhamer, D., Chen, W. C. & Padilla, W. J. Liquid Crystal Tunable Metamaterial Absorber. *Physical Review Letters* **110**, 177403, doi:10.1103/Physrevlett.110.177403 (2013).
- [16] Grzeskiewicz, B., Wolarz, E., Sierakowski, A., Marczewski, J. & Palka, N. Liquid Crystal-Tunable Metamaterial Absorber for THz Frequency Range. *2013 7th International Congress on Advanced Electromagnetic Materials In Microwaves And Optics (Metamaterials 2013)*, 178-180, 2013).
- [17] Xiao, S. M. *et al.* Tunable magnetic response of metamaterials. *Applied Physics Letters* **95**, 033115, doi:10.1063/1.3182857 (2009).
- [18] Chen, H. T. *et al.* Active terahertz metamaterial devices. *Nature* **444**, 597-600, doi:10.1038/nature05343 (2006).

- [19] Shen, N. H. *et al.* Optically Implemented Broadband Blueshift Switch in the Terahertz Regime. *Physical Review Letters* **106**, 037403, doi:10.1103/Physrevlett.106.037403 (2011).
- [20] Urzhumov, Y. *et al.* Electronically reconfigurable metal-on-silicon metamaterial. *Physical Review B* **86**, 075112, doi:10.1103/Physrevb.86.075112 (2012).
- [21] Zheludev, N. I. & Plum, E. Reconfigurable nanomechanical photonic metamaterials. *Nature Nanotechnology* **11**, 16-22, doi:10.1038/Nnano.2015.302 (2016).
- [22] Tao, H. *et al.* Reconfigurable Terahertz Metamaterials. *Physical Review Letters* **103**, 147401, doi:10.1103/Physrevlett.103.147401 (2009).
- [23] Ou, J. Y., Plum, E., Jiang, L. & Zheludev, N. I. Reconfigurable Photonic Metamaterials. *Nano Letters* **11**, 2142-2144, doi:10.1021/nl200791r (2011).
- [24] Ho, C. P. *et al.* Electrothermally actuated microelectromechanical systems based omega-ging terahertz metamaterial with polarization dependent characteristics. *Applied Physics Letters* **104**, 161104, doi:10.1063/1.4871999 (2014).
- [25] Ma, F. S., Lin, Y. S., Zhang, X. H. & Lee, C. Tunable multiband terahertz metamaterials using a reconfigurable electric split-ring resonator array. *Light-Science & Applications* **3**, e171, doi:10.1038/lisa.2014.52 (2014).
- [26] Zhu, W. M. *et al.* Switchable Magnetic Metamaterials Using Micromachining Processes. *Advanced Materials* **23**, 1792-1796, doi:10.1002/adma.201004341 (2011).
- [27] Zhu, W. M. *et al.* Microelectromechanical Maltese-cross metamaterial with tunable terahertz anisotropy. *Nature Communications* **3**, 1274, doi:10.1038/Ncomms2285 (2012).

- [28] Fu, Y. H. *et al.* A Micromachined Reconfigurable Metamaterial via Reconfiguration of Asymmetric Split-Ring Resonators. *Advanced Functional Materials* **21**, 3589-3594, doi:10.1002/adfm.201101087 (2011).
- [29] Zhao, X. *et al.* Voltage-tunable dual-layer terahertz metamaterials. *MICROSYSTEMS & NANOENGINEERING* **2**, 16025, doi:10.1038/micronano.2016.25 (2016).
- [30] Pitchappa, P. *et al.* Micro-electro-mechanically switchable near infrared complementary metamaterial absorber. *Applied Physics Letters* **104**, 201114, doi:10.1063/1.4879284 (2014).
- [31] Liu, X. L. & Padilla, W. J. Dynamic Manipulation of Infrared Radiation with MEMS Metamaterials. *Advanced Optical Materials* **1**, 559-562, doi:10.1002/adom.201300163 (2013).
- [32] Ou, J. Y., Plum, E., Zhang, J. F. & Zheludev, N. I. An electromechanically reconfigurable plasmonic metamaterial operating in the near-infrared. *Nature Nanotechnology* **8**, 252-255, doi:10.1038/nnano.2013.25 (2013).
- [33] Ou, J. Y., Plum, E., Zhang, J. F. & Zheludev, N. I. Giant Nonlinearity of an Optically Reconfigurable Plasmonic Metamaterial. *Advanced Materials* **28**, 729-733, doi:10.1002/adma.201504467 (2016).
- [34] Valente, J., Ou, J. Y., Plum, E., Youngs, I. J. & Zheludev, N. I. A magneto-electro-optical effect in a plasmonic nanowire material. *Nature Communications* **6**, 7021, doi:10.1038/Ncomms8021 (2015).
- [35] Rockstuhl, C. *et al.* On the reinterpretation of resonances in split-ring-resonators at normal incidence. *Optics Express* **14**, 8827-8836, doi:Doi 10.1364/Oe.14.008827 (2006).

- [36] Rockstuhl, C., Zentgraf, T., Meyrath, T. P., Giessen, H. & Lederer, F. Resonances in complementary metamaterials and nanoapertures. *Optics Express* **16**, 2080-2090, doi:Doi 10.1364/Oe.16.002080 (2008).
- [37] Hentschel, M., Weiss, T., Bagheri, S. & Giessen, H. Babinet to the Half: Coupling of Solid and Inverse Plasmonic Structures. *Nano Letters* **13**, 4428-4433, doi:10.1021/nl402269h (2013).
- [38] Chowdhury, S., Ahmadi, M. & Miller, W. C. A closed-form model for the pull-in voltage of electrostatically actuated cantilever beams. *Journal Of Micromechanics And Microengineering* **15**, 756-763, doi:10.1088/0960-1317/15/4/012 (2005).
- [39] Zhang, W. M., Yan, H., Peng, Z. K. & Meng, G. Electrostatic pull-in instability in MEMS/NEMS: A review. *Sensors And Actuators A-physical* **214**, 187-218, doi:10.1016/j.sna.2014.04.025 (2014).
- [40] Porto, J. A., Garcia-Vidal, F. J. & Pendry, J. B. Transmission resonances on metallic gratings with very narrow slits. *Physical Review Letters* **83**, 2845-2848, doi:10.1103/PhysRevLett.83.2845 (1999).
- [41] Noguchi, K., Mitomi, O. & Miyazawa, H. Millimeter-wave Ti : LiNbO₃ optical modulators. *Journal Of Lightwave Technology* **16**, 615-619, doi:10.1109/50.664072 (1998).
- [42] Vicari, L. *Optical applications of liquid crystals*. (Institute of Physics Pub., 2003).
- [43] Wang, Q. G., Han, W. K., Liu, P. & Dong, L. Electrically Tunable Quasi-3-D Mushroom Plasmonic Crystal. *Journal Of Lightwave Technology* **34**, 2175-2181, doi:10.1109/Jlt.2016.2526634 (2016).

- [44] Karvounis, A., Ou, J. Y., Wu, W. P., MacDonald, K. F. & Zheludev, N. I. Nano-optomechanical nonlinear dielectric metamaterials. *Applied Physics Letters* **107**, doi:10.1063/1.4935795 (2015).
- [45] Chen, H. T. *et al.* Complementary planar terahertz metamaterials. *Optics Express* **15**, 1084-1095, doi:10.1364/Oe.15.001084 (2007).
- [46] Wu, S. *et al.* Asymmetric transmission and optical rotation of a quasi-3D asymmetric metallic structure. *Optics Letters* **39**, 6426-6429, doi:10.1364/Ol.39.006426 (2014).
- [47] Aydin, K. *et al.* Split-Ring-Resonator-Coupled Enhanced Transmission through a Single Subwavelength Aperture. *Physical Review Letters* **102**, 013904, doi:10.1103/Physrevlett.102.013904 (2009).
- [48] Dong, L., Feng, Y. R. & Tian L. L. Characterization of uncooled poly SiGe microbolometer for infrared detection. *Chinese Physics Letter* **20**, 770, doi:10.1088/0256-307X/20/5/351 (2003).
- [49] Wang, Y. *et al.* Optical bound states in slotted high-contrast gratings. *Journal of the Optical Society of America B* **33**, 2472, doi:10.1364/JOSAB.33.002472 (2016).

CHAPTER 5

THERMO-MECHANICALLY TUNABLE ASYMMETRIC SPLIT RING RESONATORS FOR
NEMS-BASED INFRARED METAMATERIALS

A paper published in The 17th International Conference on Nanotechnology (IEEE NANO 2017)

Qiugu Wang, Depeng Mao, and Liang Dong

5.1 Abstract

This paper presents a nanoelectromechanical systems (NEMS)-based tunable infrared (IR) metamaterial formed with an array of Au/Si bilayer split ring resonators (SRRs) having two asymmetric arms. The wider arm of the SRR is anchored on the device substrate, while the narrower arm is suspended above the substrate and can be thermally actuated to bend downward. The thermomechanical deflection of the thin arm can change the air gap between the two arms, thus modulating the optical resonance modes of the metamaterial. With the easy-to-implement tunable SRR design, the metamaterial is rather easy to manufacture, and provides up to 90% optical signal modulation at a wavelength of 3.6 μm .

5.2 Introduction

Plasmonic metamaterials are artificially engineered resonant materials capable of manipulating light at a subwavelength scale. Their potential applications include superlenses, perfect absorbers, and biochemical sensors. Considerable efforts have been made towards the realization of tunable metamaterials at infrared (IR) wavelengths by hybridizing metamolecules with nonlinear materials such as phase-change media, liquid crystals and semiconductors [1-5]. This approach, however, often suffers from a small tuning range of light intensity and wavelength. On the other hand, micro-electro-mechanical systems (MEMS) technology has allowed lateral control of inter-metamolecular coupling of metamaterials, to achieve desired

tunability [6]. But, most existing MEMS-based tunable metamaterials resonate at relatively long wavelengths, because the introduction of MEMS actuators into metamolecules often has to sacrifice the compactness of the metamaterial. Therefore, smaller metamolecules were designed to realize reconfigurable IR metamaterial, consisting of alternating nonbendable and thermally bendable bridge structures [7]. Another reported tunable IR metamaterial was formed by pairs of parallel metallic strings and actuated by electrostatic forces [8].

In this paper, we report on a nano-electro-mechanical systems (NEMS)-based tunable metamaterial in the near- to mid-IR spectral range with structural simplicity and compactness, easy fabrication, and large spectral tunability. The central idea of the metamaterial is to form an array of bilayer metal/dielectric (Au/Si) asymmetric split ring resonators (SRRs). The SRR is unique in that one arm of the SRR is suspended from the device substrate acting as a thermally bendable element, while the other arm is anchored on the substrate. The capability to tune the optical properties of the SRR arises from the fact that mechanical deflection of the bendable arm not only alters the air gap between the two arms, but perturbs optical modes excited by the complementary SRR (c-SRR) formed on the substrate.

As shown in Fig. 5.1(a)-(c) the metamaterial is formed on a silicon-on-insulator (SOI) substrate, and composed of an array of gold/silicon (Au/Si) bilayer (20 nm-thick Au and 20 nm-thick Si) SRRs at the top and an array of Au-based c-SRRs at the bottom. There is a 100 nm vertical separation between the SRRs and c-SRRs. Each SRR unit has two 900 nm-long arms with different widths and separated by an air gap. The wider arm sits on an anchor of SiO₂. The other arm is free to bend in vertical direction (Fig. 5.1(b)). When the metamaterial is heated up, the slimmer free arm of the SRR bends towards the c-SRR due to differences in coefficients of thermal expansion between Au and Si. Therefore, different eigenmodes of the c-SRR or c-SRR

can be excited, depending on the polarization direction of incident light. As the deflection of the nanocantilever changes the air gap of the SRR, the optical properties of the eigenmodes will be tuned.

5.3 Methods

Fabrication of the metamaterial started with a SOI substrate (Fig. 5.1(d)). First, the top Si layer of the SOI substrate was thinned down to 20 nm by thermal oxidation and subsequent wet chemical etching. Next, SRRs were patterned on the surface of the thinned Si layer via e-beam lithography and subsequent reactive-ion etching. The resulting wafer was then immersed into a buffered oxide etch solution for 2 min to remove the SiO₂ layer from underneath the slimmer arms of the SRRs, while retaining most of the SiO₂ underneath the wider arms of the SRRs. Finally, a 20 nm thick Au film was evaporated onto the device surface to form Au/Si bilayer SRRs on the top and Au c-SRRs at the bottom.

Fourier transform infrared spectroscopy microscope (Hyperion 2000; Bruker; Billerica, MA) was used to obtain reflection spectra of the fabricated metamaterial under normal incidence of light. To change temperature of the metamaterial, the metamaterial was emplaced on the top of a microheater pad (PH-G4-1; Micropyretics Heaters International; Cincinnati, OH).

5.4 Results and Discussion

5.3.1 Optical properties of the metamaterial

Fig. 5.2(a) presents the measured reflection spectra of the metamaterials under transverse magnetic or TM (p) and transverse electric or TE (s) polarizations at room temperature (21 °C). Conspicuous resonance dips are observed at different wavelengths. For example, when the SRRs have a gap separation of $g = 170$ nm between the two arms (bottom curves in Fig. 5.2(a)), under

p-polarization two odd s-SRR resonance modes appear as the reflectance dips. Here we mark these resonance modes with ‘ 1^S ’ at a wavelength of 6 μm , and ‘ 3^S ’ at 3.4 μm in the spectrum,

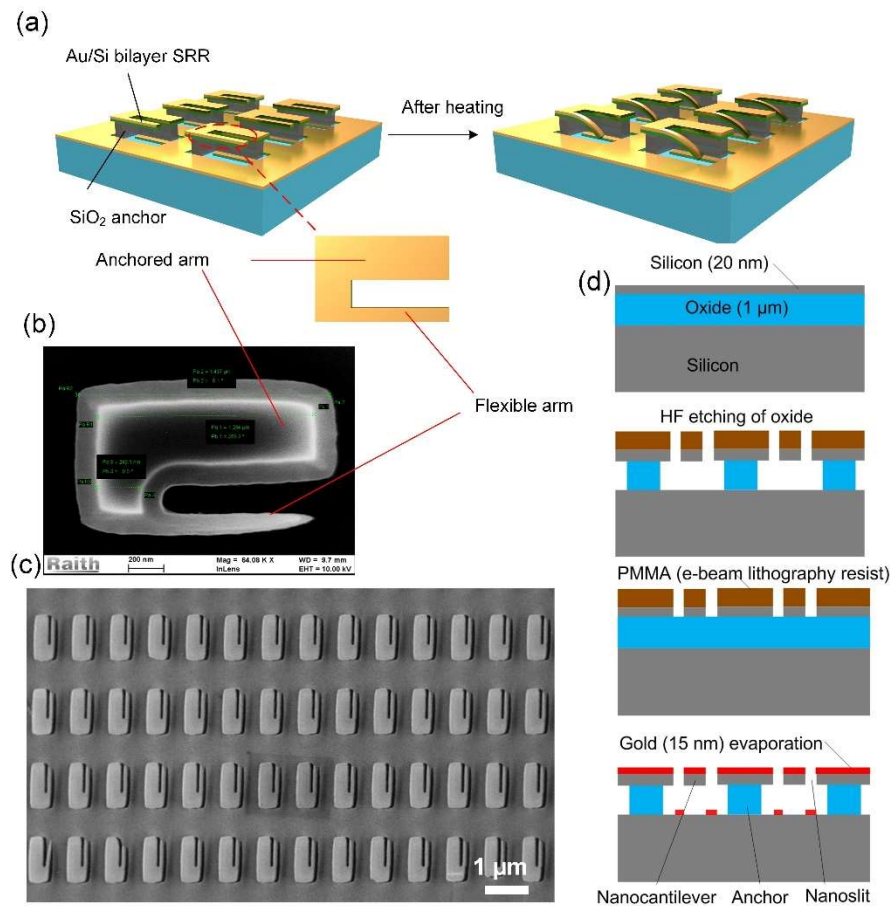


Figure 5.1 (a) Schematic of the NEMS-based tunable IR metamaterial before and after heating. (b) Scanning electron microscopy (SEM) image of tunable s-SRR. (c) SEM image of an array of s-SRRs. (d) Fabrication process flow for the tunable IR metamaterial.

where the superscripts ‘S’ denote the modes of the s-SRR. For s-polarization, two odd-order c-SRR resonances (1^C at 6.1 μm and 3^C at 3.6 μm) are excited, where the superscripts ‘C’ denote the modes of the c-SRR. Knowing that odd or even eigenmodes will be excited for SRRs under p- or s-polarized fields, to identify the order of these modes, their electric field distributions are plotted in Fig. 5.2(d). For 1^S mode, only one electric field node is seen while 3^S mode exhibits three nodes, which confirms the order of these modes. Likewise, because the bottom c-SRRs are totally

inversed structure created from top SRRs, the spectrum of the c-SRR structures under s -polarizations are very similar to that of the SRRs under p -polarizations, which are expected according to the Babinet principle.

To see how the air gap separation g between the two SRR arms influence the SRR and c-SRR resonances, we have increased the gap separation to 220 nm. It is seen that all the resonance modes exhibit slight redshifts and the levels of shift are greater for the resonances at shorter wavelengths. This also hints that the alteration of the air gap between the two arms of SRR can tune the optical properties of the metamaterial.

5.3.2 Thermomechanical tunable metamaterials

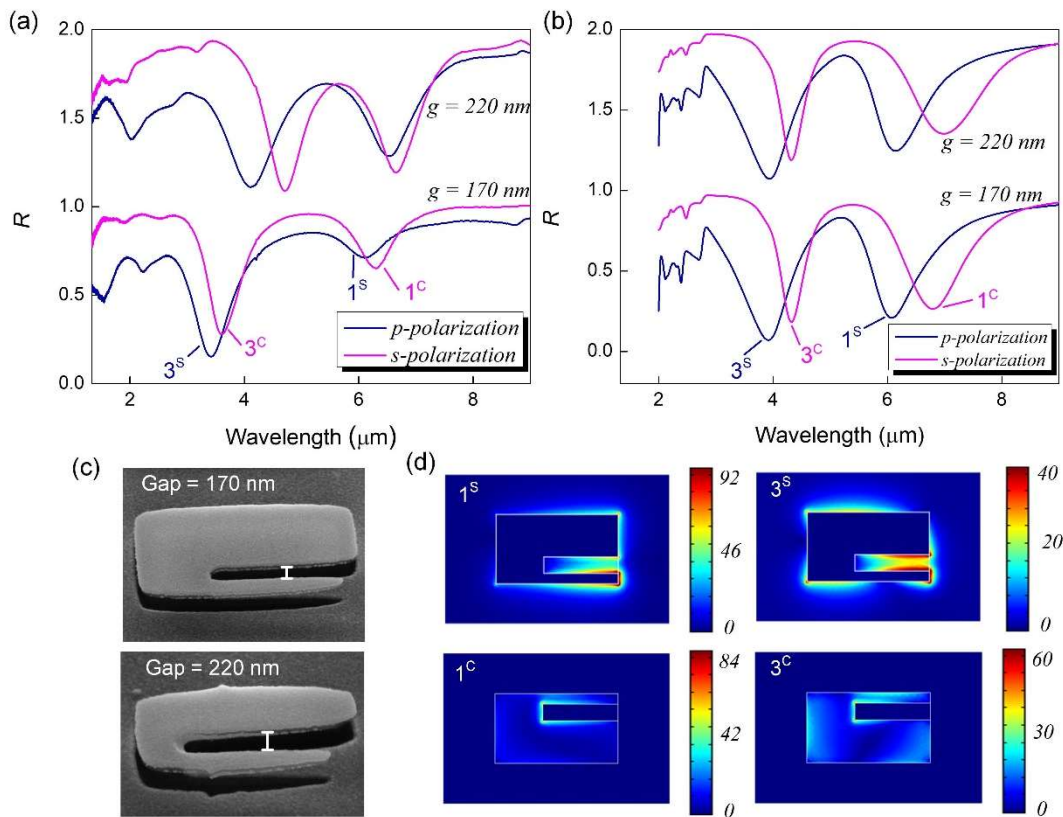


Figure 5.2 Measured (a) and Simulated (b) reflection spectra of the metamaterials under p - and s -polarizations for two devices with the gap separation of 170 nm (bottom) and 220 nm (top), respectively. (c) SEM images on 30° tilt view of the SRRs with two different gap separations. (d) Normalized electric field distributions of the modes as denoted in (b). The unit of the electric field strength is V/m.

We now discuss the influence of temperature on the characteristics of resonance modes of the metamaterial. As shown in Fig. 5.3(a) and (b), when the temperature increases from room temperature (21 °C), all the reflectance dips exhibit positive changes consistently. The changes of the optical properties are caused by the bending of the slimmer SRR arm that changes the air gap of SRR. To highlight the temperature induced variations in reflection intensity, we plot relative reflectance changes at different temperatures: $\Delta R/R_0 = (R - R_0)/R_0$, where R and R_0 represent the reflection intensities at an applied temperature and the room temperature, respectively. Here one can see that the spectra of $\Delta R/R_0$ show peak-like features. As the temperature increases, 3^S mode at p -polarization or 3^C at s -polarization presents the greatest change while other resonances show almost no changes. For example, when the temperature rise increases from 0 to 173 °C, the reflectance at the 3^S mode progressively increases from 11.9% to 20.5% (top curves in Fig. 5.3(a)). This corresponds to a relative reflectance change of $\Delta R/R_0 = 77\%$ (bottom curves in Fig. 5.3(a)). Accordingly, the value of $\Delta R/R_0$ at the 3^C is 91% when the temperature rise is 173 °C (Fig. 5.3(b)). In contrast, the lower order modes present much less changes, which are almost zero for 1^S mode and 11.8% for 1^C mode.

In Fig. 5.3(c), we summarize the reflection intensity modulations for the resonance modes of the metamaterial at different temperatures. Here one can see that, when temperature increases, for both metamaterial devices, the resonance modes for the smaller gap separation of the two SRR arms are more significant. For instance, in respond to the temperature rise of 173 °C, the values of $\Delta R/R_0$ at the 3^C (s -polarization) are 91% and 62% for $g = 170$ nm and 220 nm, respectively. Also, with the same temperature increase, the corresponding $\Delta R/R_0$ at the 3^S (p -polarization) are 77% and 49% for two devices, which agrees with the result of 3^C mode.

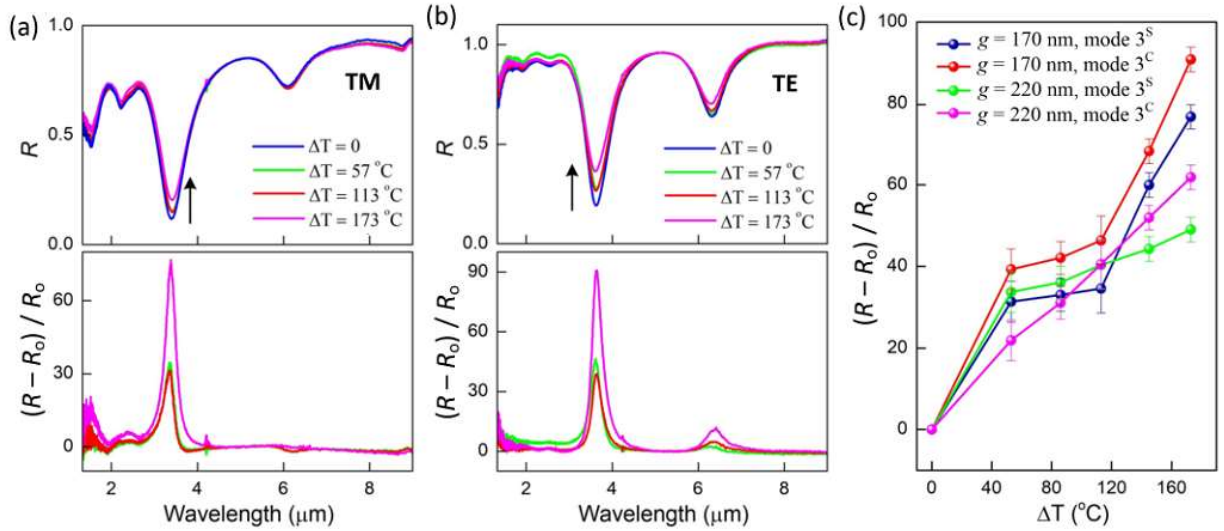


Figure 5.3 (a, b) Measured reflection spectra (top panels) of the metamaterial ($g = 170$ nm) under TM (a) and TE (b) polarizations. The bottom panels show the corresponding $\Delta R/R_0$ spectra at different temperature rises ΔT above a 21°C room temperature. The device temperature was changed by a mini heater placed below the metamaterial. Temperature was monitored by a thermocouple. (c) Summary of the changes in reflection intensity as a function of ΔT for different resonances.

Another noticeable fact is that the c-SRR modes excited under s-polarization exhibit greater changes in reflectance than corresponding s-SRR modes under p-polarization. For example, for the device with $g = 220$ nm, the relative changes for 3^S mode are 62% greater than 49% for 3^C mode at the temperature rise of 173°C . One possible explanation is that the difference in the mechanisms that change the optical properties of 3^S and 3^C modes. For 3^S mode, the optical changes originate from the geometrical gap variations caused by the bending of the slimmer arm of SRRs while for 3^C mode assumed to have no change because of the fixed structure, the optical changes are a result of downward slimmer arm that interfere the optical fields of 3^C mode. Thus, it is reasonable to assume that the latter one has a greater impact to the optical properties of the mode considering the larger effective refractive index changes it causes.

5.5 Conclusions

In summary, we developed a NEMS tunable IR metamaterial by thermally actuating the asymmetric SRR structures. This is achieved by fabricating bilayer SRRs with asymmetric arms, one of which is a slimmer freestanding bilayer while the other is anchored by oxide support. By increasing the temperature, the difference in thermal expansion coefficient of the materials results in the deflection of slimmer arms of SRRs and modulate the optical properties of the metamaterials. This tunable metamaterial will have many potential applications in transformation optics, spectral filters, switches, and many other tunable photonic devices.

5.6 Acknowledgement

This work was supported by the U.S. National Science Foundation under Grant # ECCS-0954765. The authors thank Prof. Jiming Song and Dr. Siming Yang for discussions in design and simulation of SRRs.

5.7 References

- [1] Tao, H. *et al.* Reconfigurable Terahertz Metamaterials. *Physical Review Letters* **103**, 147401, doi: 10.1103/Physrevlett.103.147401 (2009).
- [2] Wang, Q. G., Han, W. K., Liu, P. & Dong, L. Electrically Tunable Quasi-3-D Mushroom Plasmonic Crystal. *Journal Of Lightwave Technology* **34**, 2175-2181, doi:10.1109/Jlt.2016.2526634 (2016).
- [3] Wang, Q. G. *et al.* Tunable Optical Nanoantennas Incorporating Bowtie Nanoantenna Arrays with Stimuli-Responsive Polymer. *Scientific Reports* **5**, 18567, doi: 10.1038/Srep18567 (2015).
- [4] Liu, P. *et al.* Tunable meta-atom using liquid metal embedded in stretchable polymer. *Journal Of Applied Physics* **118**, doi: 10.1063/1.4926417 (2015).

- [5] Yang, S. *et al.* From Flexible and Stretchable Meta-Atom to Metamaterial: A Wearable Microwave Meta-Skin with Tunable Frequency Selective and Cloaking Effects. *Scientific Reports* **6**, 21921, doi:10.1038/srep21921 (2016).
- [6] Zhu, W. M. *et al.* Switchable Magnetic Metamaterials Using Micromachining Processes. *Advanced Materials* **23**, 1792-1796, doi:10.1002/adma.201004341 (2011).
- [7] Ou, J. Y., Plum, E., Jiang, L. & Zheludev, N. I. Reconfigurable Photonic Metamaterials. *Nano Letters* **11**, 2142-2144, doi:10.1021/nl200791r (2011).
- [8] Ou, J. Y., Plum, E., Zhang, J. F. & Zheludev, N. I. An electromechanically reconfigurable plasmonic metamaterial operating in the near-infrared. *Nature Nanotechnology* **8**, 252-255, doi:10.1038/nnano.2013.25 (2013).

CHAPTER 6

GRAPHENE “MICRODRUMS” ON FREESTANDING PERFORATED THIN MEMBRANE
FOR HIGH SENSITIVITY MEMS PRESSURE SENSOR

A paper published in *Nanoscale*

Qiugu Wang, Wei Hong, and Liang Dong

6.1 Abstract

We present a microelectromechanical systems (MEMS) graphene-based pressure sensor realized by transferring a large area, few-layered graphene on a suspended silicon nitride thin membrane perforated by a periodic array of micro-through-holes. Each through-hole is covered by a circular drum-like graphene layer, namely graphene “microdrum”. The uniqueness of the sensor design is that introducing the through-hole arrays into the supporting nitride membrane allows generating an increased strain in the graphene membrane over the through-hole array by local deformations of the holes under an applied differential pressure. Further reasons contributing to increased strain in the devised sensitive membrane include larger deflection of the membrane than that of its imperforated counterpart membrane, and direct bulging of the graphene microdrum under an applied pressure. Electromechanical measurements show a gauge factor of 4.4 for the graphene membrane and a sensitivity of $2.8 \times 10^{-5} \text{ mbar}^{-1}$ for the pressure sensor with a good linearity over a wide pressure range. The present sensor outperforms most existing MEMS-based small footprint pressure sensors using graphene, silicon, and carbon nanotubes as sensitive materials, due to the high sensitivity.

6.2 Introduction

Graphene is a promising material for applications in micro-electro-mechanical systems (MEMS) owing to its atomic thickness, fast electron mobility [1, 2] and high Young’s modulus

[3-5]. Because a single layer of graphene is impermeable to standard gases including helium [6, 7] and has strong adhesion to silicon oxide (SiO_2) substrate [8], graphene has been suggested as an atomic thick pressure sensor [7], a separation barrier between two distinct regions [9, 10] and a high-performance drumhead resonator [11]. Recently, chemical vapor deposition (CVD) has enabled large-area uniform formation of single and few-layer graphene sheets on different substrates [12-14]. This ability, in conjunction with well-developed patterning and transferring methods for graphene sheets [15-23], have opened up new opportunities of developing graphene-based sensors and actuators. Strain induced electrical-mechanical coupling in graphene are widely reported [17, 24-29]. At present a few MEMS-based graphene pressure sensors have been demonstrated [7, 30-32]. In a pioneering work on graphene pressure sensors, a graphene membrane was suspended over a shallow well etched into a SiO_2 layer grown on a silicon substrate, where the piezoresistive effect provided direct electrical readout of pressure to strain transduction and was demonstrated to be independent of crystallographic orientation [7]. Another remarkable pressure sensor design involved forming a graphene membrane on a silicon nitride (SiN_x) membrane suspended over a micromachined silicon base [30, 31]. Also, a different pressure transducer was developed by using graphene flakes to cover an array of wells engraved into a fixed SiO_2 layer grown on a silicon substrate [32]. The aforementioned graphene-based MEMS pressure sensors have a compact footprint of sub- mm^2 and even smaller. In another category of graphene-based pressure sensors, large area graphene-polymer composite and laser-scribed graphene foam have been used as sensitive materials [33, 34]. These sensors provided tremendous sensitivity, but had a large sensing area on the order of square centimeters and even larger.

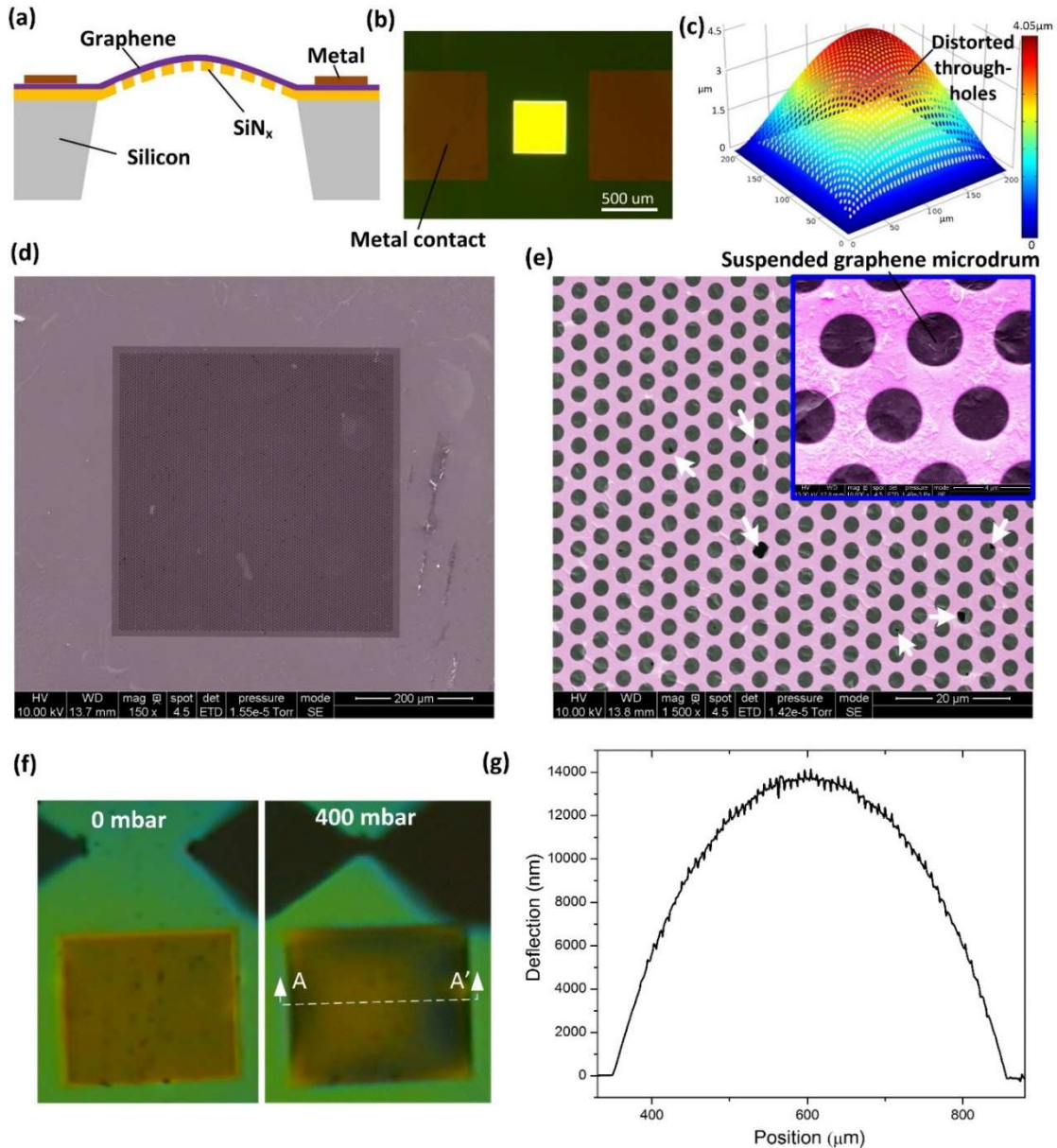


Figure 6.1 (a) Schematic of the proposed MEMS pressure sensor using a graphene membrane on a perforated SiN_x thin membrane formed on a micromachined silicon base. (b) Optical image of the fabricated pressure sensor. (c) Simulated deformation of the membrane and shape distortion of the through-holes. (d, e) SEM images of the graphene membrane on the perforated SiN_x membrane. The white arrows in (e) indicate the locations of some pinholes in the graphene. The inset of (e) shows the standalone circular graphene microdrums. (f) Optical images of the sensor before and after applying a differential pressure of 400 mbar. (g) Measured surface profile of the graphene-perforated SiN_x composite membrane along the line A-A' across the center of the membrane. The measurement was conducted using Ambios XP-100 Stylus contact surface profiler.

In this paper, we report on a high sensitivity, small area MEMS pressure sensor using few-layered graphene on a flexible perforated SiN_x thin membrane (Fig. 6.1(a) and (b)). The

SiN_x membrane acts as a supporting layer for the graphene membrane and has a periodic array of microsized through-holes (Fig 6.1(d)). Therefore, an array of circular drum-like graphene structures, namely graphene “microdrums”, are formed above these through-holes (Fig. 6.1(e)). Compared to the previously reported sensor designs of using a standalone graphene membrane [7] and an imperforated nitride-graphene composite membrane [31] as sensing elements, the introduction of the microsized through-hole array into the supporting membrane allows generating an increased membrane strain locally in the graphene layer over the holes (Fig. 6.1(c)). Further reasons which add to obtain a large strain change in graphene and thus a high pressure sensitivity of the sensor include the facts that the perforated membrane deflects more than an imperforated counterpart membrane of the same dimensions, and that the graphene microdrums are pressurized to bulge up under an applied pressure.

To proof this device concept, we fabricated a perforated SiN_x square membrane ($490 \times 490 \mu\text{m}^2$) by depositing 200 ± 2.7 nm thick nitride on a silicon substrate and patterning with $2.5 \mu\text{m}$ -diameter holes, followed by removing silicon below the membrane. Subsequently, a few-layered graphene membrane (~ 2 nm thick or ~ 6 atomic layers) was transferred on the perforated nitride membrane [18]. The nitride membrane was pretreated with oxygen plasma to improve van der Waals interactions between the graphene and nitride membrane [35-37]. After that, the graphene resistor pattern was patterned with the help of a metal shadow mask. Lastly, metal contacts were formed by using shadow mask evaporation of gold. See Methods section for details of device fabrication. To test the fabricated device, the backside of the device was adhered to the outlet of a plexiglass-based air channel. Air pressure was applied from the inlet of the air channel using a programmable syringe pump. A commercial differential pressure sensor

was used to measure differential pressures applied across the sensitive membrane. See Methods section for details of the testing setup.

Fig. 6.1(d) shows the surface coverage of graphene on the perforated nitride membrane suspended over the micromachined silicon base. Only a few pinholes were observed in the graphene membrane (see arrows in Fig. 6.1(e)), which may be introduced during the graphene deposition and/or the transfer process. To confirm that the graphene membrane stayed bonded with the nitride membrane within a range of applied pressures, we performed contact profile measurement (Fig. 6.1(f)). Fig. 6.1(g) shows that the measured maximum deflection of the composite membrane is $14.1\ \mu\text{m}$ at a differential pressure of 400 mbar. Let us assume that the pressurized graphene is totally detached from the supporting membrane. Then, according to mechanical simulations, the maximum deflection of $46\ \mu\text{m}$ will be expected at the center of the membrane, which is much larger than the measured deflection mentioned above. Therefore, it was likely that the graphene adhered well with the nitride membrane. In fact, no detachment of the graphene from the perforated nitride membrane was observed even when the membrane popped out under the air pressure of ~ 600 mbar.

The piezoresistive effect of the graphene sensor was measured with a Wheatstone bridge circuit (Fig. 6.2 (a)). A small input voltage of 20 mV was applied across the junctions of two shunt resistive circuits. The total resistance of the graphene sensor R_{tot} is composed of R_{g} of the graphene on the suspended square membrane, $R_{\text{g}1}$, $R_{\text{g}2}$, $R_{\text{g}3}$ and $R_{\text{g}4}$ of graphene in the surrounding regions, and the contact resistance R_{c} between the metal contacts and graphene. The measured R_{tot} for twelve devices varied between $1170\ \Omega$ and $1290\ \Omega$, which presumably arose from slight manufacturing inconsistency during graphene patterning and transferring steps for

these devices. The device given in Fig. 6.2(a) had $R_{\text{tot}} = 1215 \Omega$ at room temperature. The relative resistance change of the sensor $\Delta R_{\text{tot}}/R_{\text{tot}}$ can be related to the output and input voltages

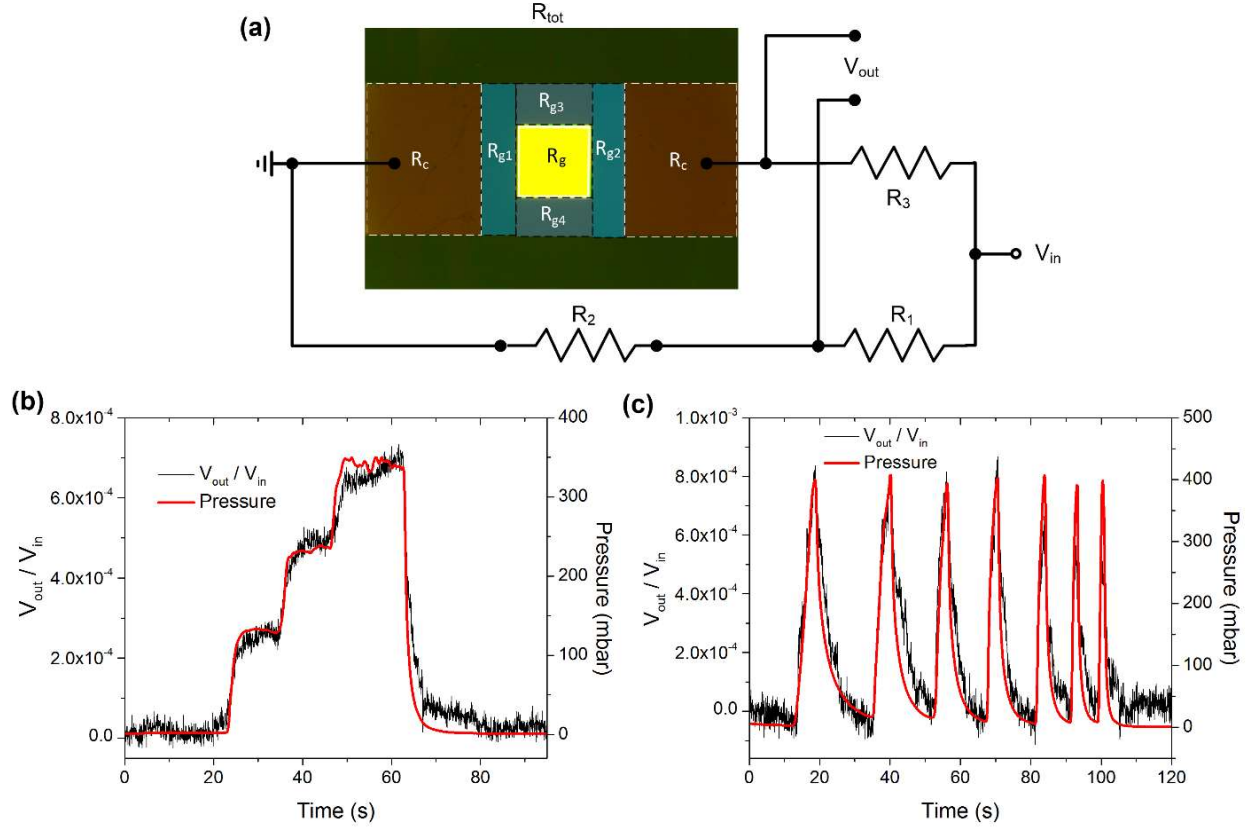


Figure 6.2 (a) Schematic of the equivalent circuit of the graphene sensing element connected into a Wheatstone bridge circuit. (b) Voltage response of the device to step like increasing differential pressures. (c) Voltage response of the device to rapid increase and gradual decrease in applied differential pressure.

(V_{out} and V_{in}) of the sensor by Eq. 6.1:

$$V_{\text{out}} = V_{\text{in}} \left(\frac{R_3}{R_3 + R_{\text{tot}}} - \frac{R_2}{R_1 + R_2} \right) \quad 6.1$$

where R_1 and R_2 were chosen to be the same and R_3 was adjusted till a balanced bridge circuit was obtained. The output voltage variation is quasi-linearly proportional to ΔR_{tot} and described as:

$$\frac{V_{\text{out}}}{V_{\text{in}}} \approx \frac{\Delta R_{\text{tot}}}{4R_{\text{tot}}} \quad 6.2$$

Based on the equivalent circuit of the sensor shown in Fig. 6.2 (a), R_{tot} is expressed in Eq. 6.3:

$$R_{\text{tot}} = R_{g1} + \frac{1}{\frac{1}{R_{g3}} + \frac{1}{R_g} + \frac{1}{R_{g4}}} + R_{g2} + 2R_c \quad 6.3$$

The dimensions of graphene resistors are obtained from Fig. 6.2 (a), which are $224 \times 978 \mu\text{m}^2$ for R_{g1} , $201 \times 978 \mu\text{m}^2$ for R_{g2} , $500 \times 261 \mu\text{m}^2$ for R_{g3} and $500 \times 246 \mu\text{m}^2$ for R_{g4} . As a result, the relationship between ΔR_{tot} and ΔR_g is obtained in Eq. 6.4:

$$\Delta R_{\text{tot}} \approx \frac{\Delta R_g}{\left(1 + \frac{R_g}{R_{g3}} + \frac{R_g}{R_{g4}}\right)^2} \quad 6.4$$

Based on the dimensions of the resistors in Fig. 6.2(a), the graphene on the suspended square membrane is estimated to be $R_g = 1473 \Omega$. The relative resistance change of this part of the graphene can be written as $\Delta R_g/R_g = 3.6 \Delta R_{\text{tot}}/R_{\text{tot}}$. As R_{g3} and R_{g4} are in parallel with R_g , their values can largely influence the measured electrical signal. If R_{g3} and R_{g4} become too low (or graphene in the side regions is too wide), the output voltage signal will be greatly suppressed. In our design, the two parallel resistors R_{g3} and R_{g4} are not totally removed. The reason for keeping R_{g3} and R_{g4} is from a practical standpoint as follows. As mentioned earlier, our fabrication process utilized the metal shadow mask to form the graphene pattern on the device surface. Although using the metal shadow mask simplified the device fabrication process, the accuracy of aligning the shadow mask and the suspended SiN_x thin membrane was relatively low ($\sim 100 \mu\text{m}$). To avoid misaligning the edges of graphene pattern into the perforated SiN_x membrane region, we intended to keep the two side resistors R_{g3} and R_{g4} on the device surface. The present design sacrificed the sensitivity but gains the simplicity of device fabrication. By optimizing fabrication processes, it is possible to further increase the sensitivity of the device.

6.3 Results and Discussion

Fig. 6.2(b) shows the output voltage normalized to the input voltage of the device responding to an increase in step-like differential pressure. The output voltage rose with increasing air pressure applied to the graphene-perforated membrane. At a differential pressure of 350 mbar, 0.067% relative change was observed at the output voltage, corresponding to 0.97% change in the resistance. The rapid rise of the output signal indicates an immediate piezoresistive response to the pressure applied to the membrane. Based on the noise floor of the output signal shown in Fig. 6.2 (b), the noise equivalent pressure resolution of the sensor is about 30 mbar, which can be further improved by optimizing the detection circuit, e. g., using a low-pass filter and a low-noise amplifier.

Fig. 6.2(c) show the results of cyclic pressure testing for the device. The experiment involved rapidly applying differential air pressure to the sensitive membrane by pumping air and then gradually releasing the pressure. In Fig. 6.2(c), the pressure pump time was controlled from 7 s to 1.5 s while the pressure release time was decreased from 18 s to 2 s by adjusting the air pumping and withdrawal speed of the pressure control apparatus. It is clear that upon applying an air pressure, the output voltage was able to quickly follow the sudden increase of the internal pressure and then go back to the baseline. The response time here is mainly determined by the pump and vent speed, so the actual response time is expected to be faster.

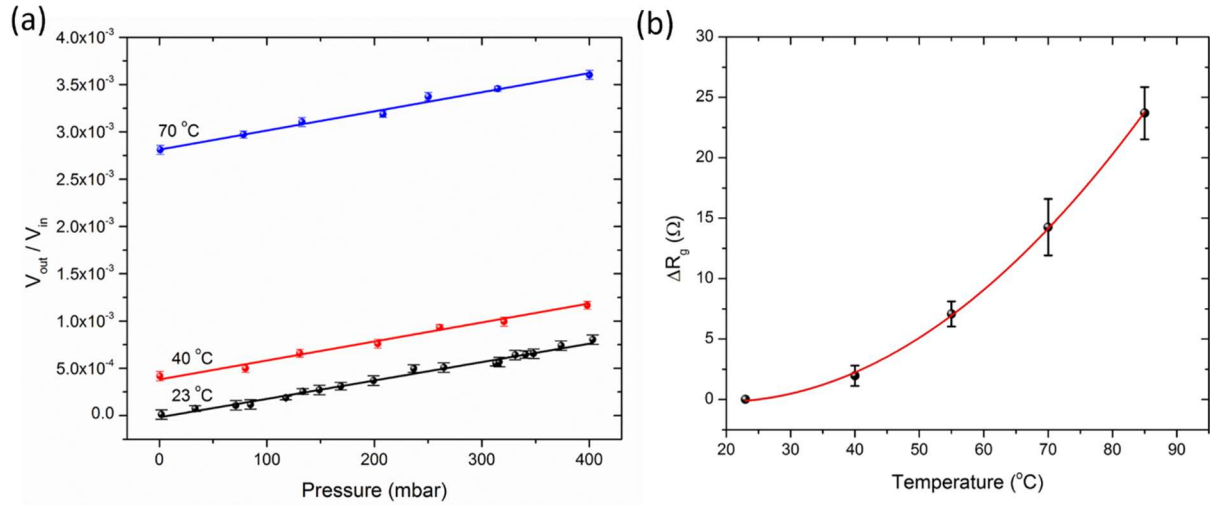


Figure 6.3 (a) Static voltage response of the sensor as function of applied differential pressure at the temperatures of 23°C, 40°C and 70°C. (b) The change of graphene resistance versus different temperature before applying differential pressure. The resistance of graphene R_g was measured to be 1215.43 Ω at 23 °C.

Fig. 6.3(a) shows the static response of V_{out}/V_{in} of the device with respect to applied pressure. In order to see the influence of temperature variation on the sensitivity, the device at different temperatures was measured. At 23 °C, a good linearity was observed and the sensitivity of 3.88×10^{-5} mV/mbar was obtained. The gauge factor G of graphene for the sensor was estimated by $G = \frac{\Delta R/R}{\Delta L/L} = 4.4$ at 350 mbar. Here, the average strain of the suspended square membrane was calculated to be 0.22% for 14.3 μm deflection at the center of the membrane [38]. The obtained gauge factor of the graphene used here is comparable to other reported CVD-grown graphene [7, 26, 31]. For example, the reported gauge factor is 2.92 for the standalone graphene [7], 6.1 for the graphene on poly(dimethylsiloxane) substrate [26], and 1.6 for the graphene on the SiN_x membrane [31]. As the environmental temperature increased from room temperature to 70 °C, the response of V_{out}/V_{in} showed an overall increase and had a good linear dependence on the applied pressure. The slopes of the linearly fitted curves at different temperatures were almost unchanged, indicating that within the tested temperature range, the temperature variations

actually did not degrade the sensitivity of the device. Fig. 6.3(b) plots the change of graphene resistance with increasing temperature. A nonlinear positive temperature coefficient of the graphene resistance is observed, which is similar to previously reported result [2]. At 70 °C, the resistance of graphene increased by 2.3% compared to that at 23 °C.

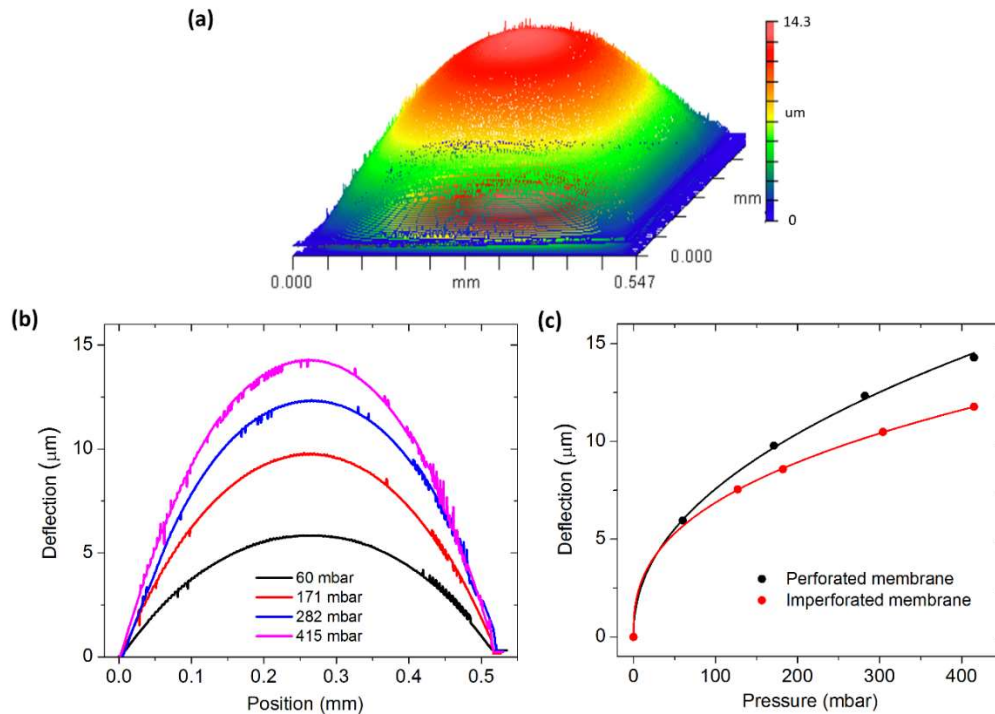


Figure 6.4 (a) Measured 3D surface profile of the graphene coated perforated nitride membrane under 415 mbar differential pressure. (b) Deflection profiles of the membrane across the middle line of the perforated membrane (parallel to the side of the membrane) under various differential pressures. (c) Maximum deflection at the center of the membrane as a function of differential pressure for the perforated and the imperforated membranes. The black and red dots are the experimental data. The black and red lines are the fitted curves obtained using Eq. 6.5.

We studied the roles of the perforated SiN_x membrane and the graphene microdrums over the through-holes in determining the sensitivity of the sensor. First, mechanical responses of the graphene coated perforated nitride membrane to different applied pressures were visualized using a 3D optical surface profiler (ZYGO Newview, Middlefield, CT). As shown in Fig. 6.4(a), under 415 mbar differential pressure, the membrane was deformed into a convex shape with a

maximum out-of-plane deflection of 14.3 μm at its center. The measured surface profiles of the membrane under other differential pressures were also given in Fig. 6.4(b). For a square imperforated nitride membrane, the maximum out-of-plane deflection δ with respect to differential pressure P can be described with the following equation [39, 40]:

$$P = \frac{B_1 t \sigma_0}{(a/2)^2} \delta + \frac{B_2 f(v) t E}{(a/2)^4 (1-\nu)} \delta^3 \quad 6.5$$

where B_1 and B_2 are dimensionless constants, σ_0 is the initial stress, E is Young's modulus, a is the side length of the square membrane, ν is the Poisson ratio, $f(v)$ is a geometry function, and t is the thickness of the membrane. $B_1 = 3.45$, $B_2 = 1.994$, $\nu = 0.22$, and $E = 239$ GPa were taken from Refs [40, 41]. Previous research shows that perforated membrane can be replaced with imperforated one with modified elastic modulus in the numerical calculation [42]. Thus, the Eq. 6.5 can also be applied to perforated membrane. Fig. 6.4(c) shows the fitted results for the graphene coated perforated membrane, as well as the graphene coated imperforated counterpart membrane with the same dimensions for comparison purpose. It was obtained that $\sigma_0 = 58$ MPa and $f(v) = 0.32$ for the perforated membrane, while $\sigma_0 = 41$ MPa and $f(v) = 0.65$ for the imperforated one. By using the obtained deflection equations for both of the perforated and imperforated membrane, the ratio of maximum deflection between the perforated and imperforated membrane can be expressed by Eq. 6.6:

$$\frac{d_{\text{perforated}}}{d_{\text{imperforated}}} = 0.533 \times P^{0.08} \quad 6.6$$

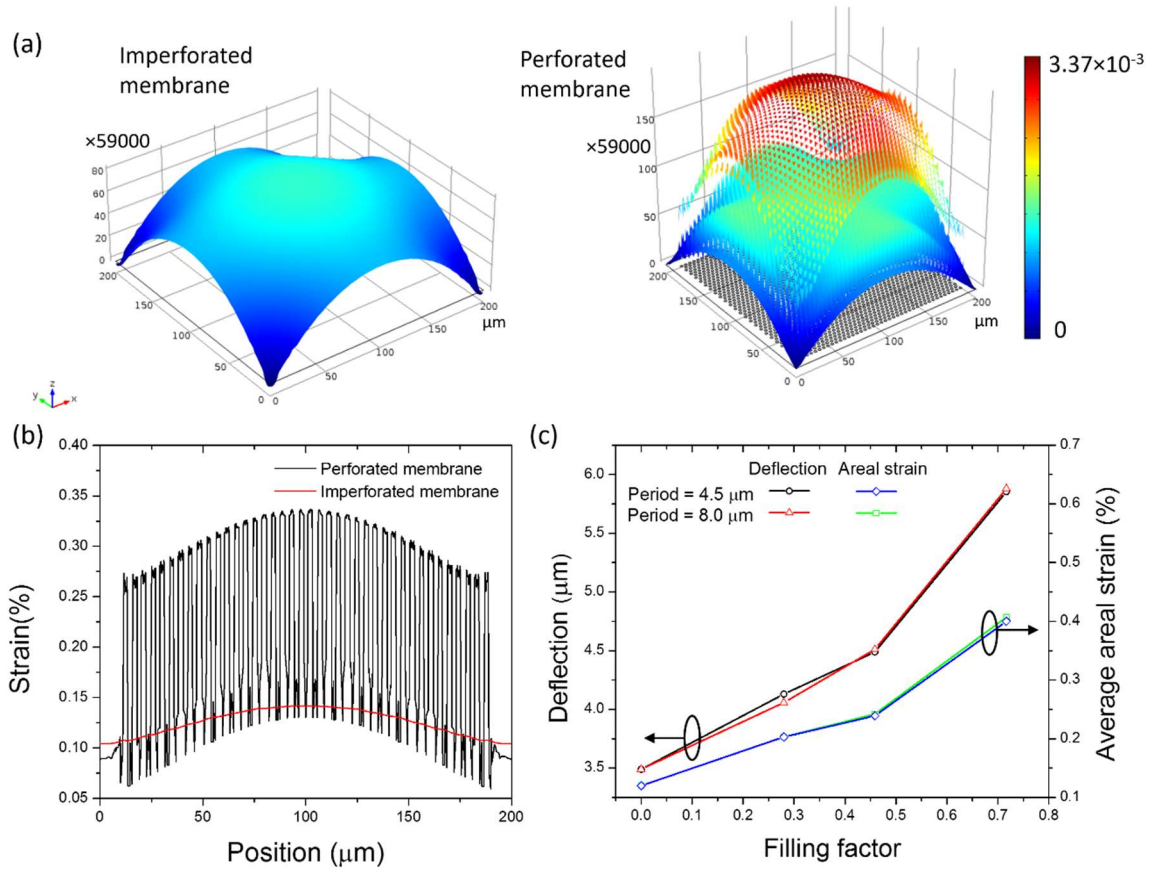


Figure 6.5 (a) Simulated areal strain under a differential pressure of 500 mbar for the imperforated (left) and perforated (right) membranes. The z coordinate and the color scale show the amplitude of the areal strain. (b) The areal strain along the line across the center of the perforated and imperforated membranes. (c) Deflection and average areal strain along the line across the center of the membrane versus different filling factor of the device. The filling factor is defined as the ratio between the area of holes and the membrane. The period of the holes is fixed to be 4.5 μm or 8.0 μm while the diameter of the hole is gradually increased.

Under the differential pressure of 415 mbar, the imperforated membrane with graphene had the maximum deflection of 11.7 μm , which was 2.6 μm less than that the perforated membrane with graphene. The Eq. 6.6 also indicates that further increasing differential pressure will not significantly improve the deflection of the graphene coated perforated membrane compared to the imperforated counterpart membrane, and therefore, will have some but limited effect to improve pressure sensitivity of the device.

Next, we conducted mechanical simulations to illustrate strain distributions in both of the perforated and imperforated SiN_x membranes, each including the ~ 2 nm thick graphene layer. The simulations were carried out through finite element method based commercial package (COMSOL Multiphysics). Limited by computational power, a reduced model of side length 200 μm was calculated for the purpose of illuminating the working mechanism. According to Eq. 6.5, assuming that there is zero initial stress in the SiN_x membrane, the maximum out-of-plane deflection of the membrane will be proportional to $a^{4/3}/t^{1/3}$. Therefore, under the same differential pressure, the strain developed in the SiN_x membrane with the real side length $a = 490 \mu\text{m}$ should be higher than that simulated with the reduced model of side length $a = 200 \mu\text{m}$. While the strain of the membrane can be further increased by using a larger and thinner membrane, the increased strain will also lead to local cracks or even pop-out of the membrane under a low differential pressure, thus lowering the allowed maximum pressure of the sensor. Also, in our device fabrication, when the perforated thin SiN_x membrane had a side length more than 750 μm, the membrane was not able to initially stay flat but tended to bend downward, possibly due to the initial stress of the thin and relatively complex membrane perforated by an array of through holes. Therefore, we set the side length to 500 μm for the membrane, with which the maximum allowed pressure was around 600 mbar. Under 500 mbar differential pressure, the imperforated membrane had the maximum areal strain of 0.14% at the center of the membrane with the deflection of 3.49 μm (Fig. 6.5(a)). For the perforated membrane, a similar strain distribution was observed. In the non-hole areas of the membrane the maximum areal strain was found to be 0.15%, which was only slightly higher than that observed in the imperforated counterpart membrane. However, the maximum areal strain in the graphene layer over the holes reached 0.34% at the center of the membrane with the maximum deflection of 4.13 μm. Therefore, the

maximum strain in the hole areas was as high as 2.27 times that occurred in the non-hole areas of the perforated membrane. Furthermore, the average areal strain along the line across the center of the perforated and imperforated membranes was 0.203% and 0.12%, respectively (Fig. 6.5(c)). Although the maximum deflection of the perforated and imperforated membranes differed only by 18.3% (3.49 μm vs. 4.13 μm), the average strain in the perforated membrane increases by 62.4% (0.203 % vs. 0.12 %) due to the introduction of the through-holes into the SiN_x membrane.

We further investigated the effect of the hole diameter and period on the mechanical properties of the membrane. Here, filling factor is defined as the ratio of the area of all the holes to the area of the whole membrane. As shown in Fig. 6.5(c), given the same filling factor, the period of holes has almost no influence on the deflection and average areal strain of the membrane. As the filling factor or the total hole area increases, the deflection and the average areal strain of the membrane continuously grows. For example, with increasing filling factor from 0.28 (of the present device) to 0.46, the average areal strain only increases from 0.20 % to 0.24 %. A significant increase in areal strain is observed from 0.24 % to 0.40 % as the filling factor increases from 0.46 to 0.72. To achieve the filling factor of 0.72 for the device with the period of 4.5 μm , the hole diameter should increase from the present 2.5 μm to 4 μm . However, two practical issues have played to restrict the hole size. First, the larger size holes may induce more pinholes in the graphene drums when transferring the graphene onto the membrane [23], thus resulting in more air leakage. Second, with the filling factor of 0.72, the distance of two neighboring holes would be only 500 nm, which may lead to easy cracking or even pop-out of the membrane under an applied differential pressure. Therefore, while the sensitivity of the device can be improved further by introducing larger size holes in the SiN_x membrane, the

Table 6.1 Performance comparison among MEMS pressure sensors

Device structure	Dimensions (μm^2)	Sensitivity (mbar^{-1})	Reference
Graphene on 200 nm thick perforated SiN_x membrane	490×490	2.8×10^{-5}	This work
Suspended graphene	6×64	2.96×10^{-6}	Smith et al., Nano Lett. 2013 [7]
Graphene meander on 100 nm thick SiN_x membrane	280×280	6.67×10^{-6}	Zhu et al., Appl. Phys. Lett. 2013 [31]
Graphene on fixed perforated layer on silicon substrate	110×220	0.88×10^{-6}	Hurst et al., Transducers, 2013 [32]
Carbon nanotubes	100×100	1.06×10^{-6}	Hierold et al., Sens. Actuator A, 2007 [44]
100 μm thick polysilicon membrane	100×100	1.5×10^{-6}	Kalvesten et al., MEMS, 1998 [43]
30 μm thick silicon membrane	470×470	3.2×10^{-6}	Zhang et al., IEEE Sens. J., 2007 [45]
4 μm thick polysilicon membrane	400×400	1.29×10^{-6}	Yang, et al., Tamkang J. Sci. Eng., 2005 [46]

current design with 2.5 μm -diameter through-holes is considered safe and conservative and able to compromise the sensitivity and robustness of the device.

Furthermore, as the differential pressure was applied to the graphene coated perforated membrane, the graphene microdrums over the holes also bulged into a curved shape. To illustrate how this bulging factor affected the pressure sensitivity of the device compared to the in-plane membrane strain, let us imagine a state when the strain in the pressurized SiN_x membrane is suppressed, i.e., the holes stay in the plane and maintain the original circular shape with a diameter of 2.5 μm . Simulations showed that, under 500 mbar differential pressure, the graphene microdrum will deflect by 9.1 nm at its center and the average strain of 0.0035% will be obtained over the whole microdrum. The magnitude of this strain is about two orders of magnitude lower than the aforementioned maximum strain of 0.34% in the microdrum. Therefore, the bulging of the pressurized circular graphene had a limited influence on the overall strain change of the microdrum. As a matter of fact, the previously reported graphene-based pressure sensors

employed the bulging effect of the graphene suspended over the wells in the fixed substrate, thus offering relatively low sensitivity [32]. Comparison between the effects of membrane strain and bulging, it is evident that the inhomogeneous membrane strain of the perforated membrane was the key to the improved pressure sensitivity of the device.

Table 6.1 compares our device with the recently reported graphene-based MEMS or NEMS pressure sensors. Generally, the sensitivity of piezoresistive pressure sensors can be calculated using $S = \frac{\Delta R}{R \times P}$. Our sensor has the sensitivity of $2.8 \times 10^{-5} \text{ mbar}^{-1}$ which outperforms most of the reported graphene, silicon, and polysilicon based MEMS/NEMS pressure sensors [7, 31, 32, 38, 43-46]. Specifically, the present sensitivity is higher than $2.96 \times 10^{-6} \text{ mbar}^{-1}$ of the standalone graphene membrane-based sensor [7] and $6.67 \times 10^{-6} \text{ mbar}^{-1}$ of the sensor using the graphene meander patterns on imperforated SiN_x membrane [31]. As mentioned above, another previous pressure sensor used a graphene membrane suspended over the wells made in a SiO_2 layer on the bulk silicon substrate, where the resistance variation only came from the bulging effect of the graphene. The resulting sensitivity of that sensor was about 32 times of magnitude lower compared to our sensor.

6.4 Methods and Experimental Details

6.4.1 Device Fabrication

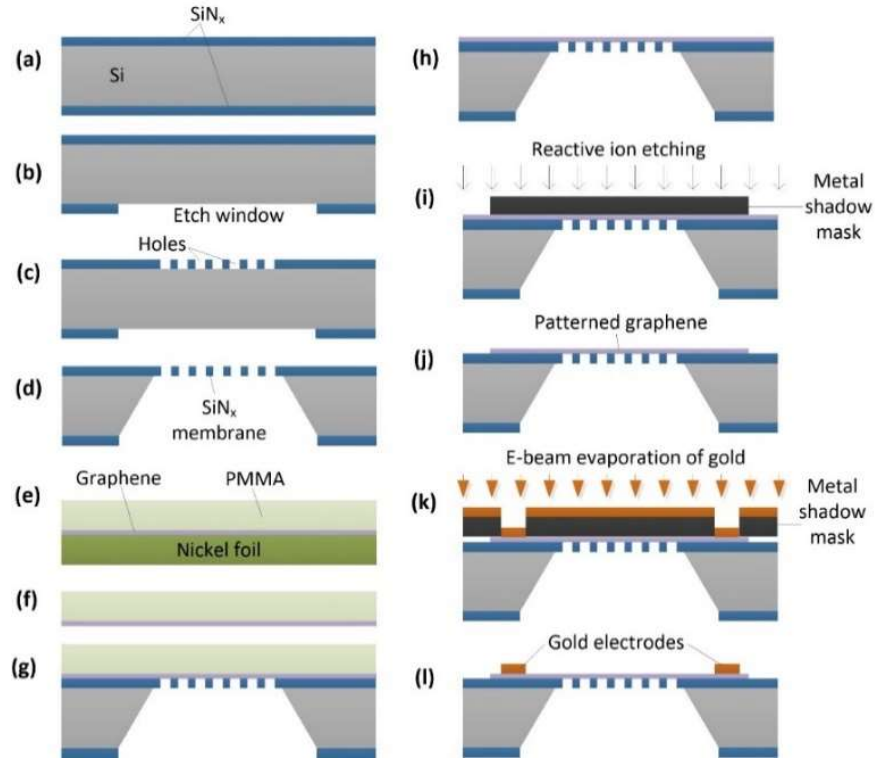


Figure 6.6 Schematic of the fabrication processes for the device.

The device fabrication started with a 3-in double side polished silicon wafer (p-type). A 200 nm thick SiN_x layer was formed on both sides of the wafer by plasmon enhanced chemical vapor deposition (Fig. 6.6(a)). Etch windows were then created on the back side of the wafer with photolithography and reactive ion etching of SiN_x (Fig. 6.6(b)). Subsequently, an array of 2.5 μm diameter holes were patterned in the SiN_x layer on the front side of the wafer with the same method as that used in the last step (Fig. 6.6(c)). After that, an anisotropic etch of silicon substrate with tetramethylammonium hydroxide (20.0 wt %, 78°C, Sigma-Aldrich, St. Louis, MO) was performed to create a suspended nitride membrane ($490 \times 490 \mu\text{m}^2$) (Fig. 6.6(d)). The wafer was then diced into $6 \times 6 \text{ mm}^2$ pieces for the following processes. Commercially available CVD-grown graphene film on a 25 μm thick nickel foil ($1 \times 1 \text{ cm}^2$, University Wafer, Boston, MA) was used as the sensitive material of the device. Only one side of the foil was coated with

graphene. To transfer the graphene film to the suspended nitride membrane, we used the poly(methyl methacrylate) or PMMA based transfer method following the protocol given in Ref. [18]. In this step, the nickel foil with graphene was drop-coated with PMMA (molecular weight ~996 000 by GPC, Sigma-Aldrich, dissolved in chlorobenzene with a concentration of 46 mg/mL) (Fig. 6.6(e)). The foil was then cured at 180 °C for 1 min, followed by etching away the nickel substrate by FeCl₃ solution (0.1 g/ml, Sigma-Aldrich, St. Louis, MO) for 20 hr (Fig. 6.6(f)). After that, the PMMA-graphene stack was picked up and washed with deionized water, and then, was placed on the SiN_x membrane treated with oxygen plasma (Fig. 6.6(g)). Finally, the PMMA substrate of the graphene film was etched by PMMA remover (Nano remover PG, MicroChem, Westborough, MA) (Fig. 6.6(i)). Next, the graphene resistor was patterned in an oxygen plasma etcher with the help of a shadow mask made of aluminum prefabricated by a high-precision milling machine (Supra CNC Mill, CNC Masters, Irwindale, CA) (Fig. 6.6(j)). Then, another aluminum shadow mask was machined and placed on the device to make gold contacts by e-beam evaporation of a 200 nm gold layer (Fig. 6.6(k)). In these shadow mask based patterning, careful alignment between the shadow mask and the device was needed. Finally, the device was realized (Fig. 6.6(l)).

6.4.2 Measurement Setup

The backside of the device was adhered to the outlet of an acrylic glass based microfluidic channel with structural adhesives. Air pressure was applied from the inlet of the air channel using a programmable syringe pump (KDS210P, KD Scientific, Holliston, MA). A commercial differential pressure sensor (MPX5500DP, Freescale Semiconductor, Austin, TX) was used to measure differential pressures applied across the sensing membrane. A feedback circuit was used to enhance stability of the pressure control system. The output voltage signal of

the commercial sensor was recorded by a data acquisition device (DI-245, DATAQ Instruments, Akron, OH) and then was converted to a differential pressure. The graphene sensor was connected into a Wheatstone bridge circuit as shown in Fig. 6.6(a). An input DC voltage of 20 mV was applied across the bridge circuit. The small voltage was applied to avoid excessive heating of graphene. The output voltage from the graphene sensor was recorded with a digital multimeter (34401A, Agilent Technologies, Santa Clara, CA).

6.5 Conclusions

In conclusion, we have demonstrated a graphene based small area MEMS pressure sensor formed by transferring large area CVD-grown graphene onto a suspended SiN_x membrane perforated by an array of through-holes. The large voltage response of the sensor was majorly due to the large strain change of the graphene suspended over the through-holes under applied differential pressure across the membrane. The measured sensitivity has demonstrated that the devised new pressure sensor structure excels in providing high sensitivity that outperforms many other existing graphene based counterpart sensors. Future work includes optimizing fabrication processes to reduce number of pinholes in graphene, improving yield of transferring graphene membrane to suspended nitride membrane, and designing a low-noise electronic readout circuit for the sensor.

6.6 Acknowledgement

This work was supported in part by United States National Science Foundation under Grant #ECCS-0954765 and Iowa Department of Transportation. The authors thank Dr. Ashraf Bastawros for 3D optical profile measurement, and Seval Oren and Dr. Warren Straszheim for SEM imaging.

6.7 References

- [1] Bolotin, K. I. *et al.* Ultrahigh electron mobility in suspended graphene. *Solid State Communications* **146**, 351-355, doi:10.1016/j.ssc.2008.02.024 (2008).
- [2] Morozov, S. V. *et al.* Giant intrinsic carrier mobilities in graphene and its bilayer. *Physical Review Letters* **100**, 016602, doi:10.1103/PhysRevLett.100.016602 (2008).
- [3] Frank, I. W., Tanenbaum, D. M., Van der Zande, A. M. & McEuen, P. L. Mechanical properties of suspended graphene sheets. *Journal Of Vacuum Science & Technology B* **25**, 2558-2561, doi:10.1116/1.2789446 (2007).
- [4] Lee, C., Wei, X. D., Kysar, J. W. & Hone, J. Measurement of the elastic properties and intrinsic strength of monolayer graphene. *Science* **321**, 385-388, doi:10.1126/science.1157996 (2008).
- [5] Poot, M. & van der Zant, H. S. J. Nanomechanical properties of few-layer graphene membranes. *Applied Physics Letters* **92**, doi: 10.1063/1.2857472 (2008).
- [6] Bunch, J. S. *et al.* Impermeable atomic membranes from graphene sheets. *Nano Letters* **8**, 2458-2462, doi:10.1021/nl801457b (2008).
- [7] Smith, A. D. *et al.* Electromechanical Piezoresistive Sensing in Suspended Graphene Membranes. *Nano Letters* **13**, 3237-3242, doi:10.1021/nl401352k (2013).
- [8] Koenig, S. P., Boddeti, N. G., Dunn, M. L. & Bunch, J. S. Ultrastrong adhesion of graphene membranes. *Nature Nanotechnology* **6**, 543-546, doi:10.1038/Nnano.2011.123 (2011).
- [9] Jiang, D. E., Cooper, V. R. & Dai, S. Porous Graphene as the Ultimate Membrane for Gas Separation. *Nano Letters* **9**, 4019-4024, doi:10.1021/nl9021946 (2009).

- [10] Guo, F. *et al.* Graphene-Based Environmental Barriers. *Environmental Science & Technology* **46**, 7717-7724, doi:10.1021/es301377y (2012).
- [11] Klimov, N. N. *et al.* Electromechanical Properties of Graphene Drumheads. *Science* **336**, 1557-1561, doi:10.1126/science.1220335 (2012).
- [12] Yu, Q. K. *et al.* Graphene segregated on Ni surfaces and transferred to insulators. *Applied Physics Letters* **93**, doi: 10.1063/1.2982585 (2008).
- [13] Li, X. S. *et al.* Large-Area Synthesis of High-Quality and Uniform Graphene Films on Copper Foils. *Science* **324**, 1312-1314, doi:10.1126/science.1171245 (2009).
- [14] Reina, A. *et al.* Large Area, Few-Layer Graphene Films on Arbitrary Substrates by Chemical Vapor Deposition. *Nano Letters* **9**, 30-35, doi:10.1021/nl801827v (2009).
- [15] Jiao, L. Y. *et al.* Creation of nanostructures with poly(methyl methacrylate)-mediated nanotransfer printing. *Journal Of The American Chemical Society* **130**, 12612-12613, doi:10.1021/ja805070b (2008).
- [16] Reina, A. *et al.* Transferring and Identification of Single- and Few-Layer Graphene on Arbitrary Substrates. *Journal Of Physical Chemistry C* **112**, 17741-17744, doi:10.1021/jp807380s (2008).
- [17] Kim, K. S. *et al.* Large-scale pattern growth of graphene films for stretchable transparent electrodes. *Nature* **457**, 706-710, doi:10.1038/nature07719 (2009).
- [18] Li, X. S. *et al.* Transfer of Large-Area Graphene Films for High-Performance Transparent Conductive Electrodes. *Nano Letters* **9**, 4359-4363, doi:10.1021/nl902623y (2009).
- [19] Dean, C. R. *et al.* Boron nitride substrates for high-quality graphene electronics. *Nature Nanotechnology* **5**, 722-726, doi:10.1038/nnano.2010.172 (2010).

- [20] Aleman, B. *et al.* Transfer-Free Batch Fabrication of Large-Area Suspended Graphene Membranes. *Acs Nano* **4**, 4762-4768, doi:10.1021/nn100459u (2010).
- [21] Regan, W. *et al.* A direct transfer of layer-area graphene. *Applied Physics Letters* **96**, doi: 10.1063/1.3337091 (2010).
- [22] Kim, K. *et al.* Grain Boundary Mapping in Polycrystalline Graphene. *Acs Nano* **5**, 2142-2146, doi:10.1021/nn1033423 (2011).
- [23] Suk, J. W. *et al.* Transfer of CVD-Grown Monolayer Graphene onto Arbitrary Substrates. *Acs Nano* **5**, 6916-6924, doi:10.1021/nn201207c (2011).
- [24] Ni, Z. H. *et al.* Uniaxial Strain on Graphene: Raman Spectroscopy Study and Band-Gap Opening. *Acs Nano* **2**, 2301-2305, doi:10.1021/nn800459e (2008).
- [25] Pereira, V. M., Castro Neto, A. H. & Peres, N. M. R. Tight-binding approach to uniaxial strain in graphene. *Physical Review B* **80**, doi: 10.1103/Physrevb.80.045401 (2009).
- [26] Lee, Y. *et al.* Wafer-Scale Synthesis and Transfer of Graphene Films. *Nano Letters* **10**, 490-493, doi:10.1021/nl903272n (2010).
- [27] Fu, X. W. *et al.* Strain dependent resistance in chemical vapor deposition grown graphene. *Applied Physics Letters* **99**, doi: 10.1063/1.3663969 (2011).
- [28] Wang, Y. *et al.* Super-Elastic Graphene Ripples for Flexible Strain Sensors. *Acs Nano* **5**, 3645-3650, doi:10.1021/nn103523t (2011).
- [29] Huang, M. Y., Pascal, T. A., Kim, H., Goddard, W. A. & Greer, J. R. Electronic-Mechanical Coupling in Graphene from in situ Nanoindentation Experiments and Multiscale Atomistic Simulations. *Nano Letters* **11**, 1241-1246, doi:10.1021/nl104227t (2011).

- [30] Hosseinzadegan, H. *et al.* Graphene Has Ultra High Piezoresistive Gauge Factor. 2012 *Ieee 25th International Conference on Micro Electro Mechanical Systems (Mems)*, 2012).
- [31] Zhu, S. E., Ghatkesar, M. K., Zhang, C. & Janssen, G. C. A. M. Graphene based piezoresistive pressure sensor. *Applied Physics Letters* **102**, doi: 10.1063/1.4802799 (2013).
- [32] Hurst, A. M. *et al.* in *Solid-State Sensors, Actuators and Microsystems (TRANSDUCERS & EUROSENSORS XXVII)*, 2013 *Transducers & Eurosensors XXVII: The 17th International Conference on.* 586-589 (2013).
- [33] Yao, H. B. *et al.* A Flexible and Highly Pressure-Sensitive Graphene-Polyurethane Sponge Based on Fractured Microstructure Design. *Advanced Materials* **25**, 6692-6698, doi:10.1002/adma.201303041 (2013).
- [34] Tian, H. *et al.* A Graphene-Based Resistive Pressure Sensor with Record-High Sensitivity in a Wide Pressure Range. *Scientific Reports* **5**, doi:b10.1038/Srep08603 (2015).
- [35] Chen, C. W. *et al.* UV ozone treatment for improving contact resistance on graphene. *Journal Of Vacuum Science & Technology B* **30**, doi: 10.1116/1.4754566 (2012).
- [36] Li, W. *et al.* Ultraviolet/ozone treatment to reduce metal-graphene contact resistance. *Applied Physics Letters* **102**, doi: 10.1063/1.4804643 (2013).
- [37] Seo, J., Chang, W. S. & Kim, T. S. Adhesion improvement of graphene/copper interface using UV/ozone treatments. *Thin Solid Films* **584**, doi:10.1016/j.tsf.2015.01.007, 170-175 (2015).

- [38] Smith, A. D., Vaziri, S., Delin, A., Ostling, M. & Lemme, M. C. Strain engineering in suspended graphene devices for pressure sensor applications. *Ultimate Integration on Silicon (ULIS), 2012 13th International Conference on*, 21-24, doi:10.1109/ULIS.2012.6193347 (2012).
- [39] Allen, M. G., Mehregany, M., Howe, R. T. & Senturia, S. D. Microfabricated Structures for the Insitu Measurement Of Residual-Stress, Youngs Modulus, And Ultimate Strain Of Thin-Films. *Applied Physics Letters* **51**, 241-243, doi:10.1063/1.98460 (1987).
- [40] MaierSchneider, D., Maibach, J. & Obermeier, E. A new analytical solution for the load-deflection of square membranes. *Journal Of Microelectromechanical Systems* **4**, 238-241, doi:10.1109/84.475551 (1995).
- [41] Gavan, K. B., Westra, H. J. R., Van der Drift, E. W. J. M., Venstra, W. J. & Van der Zant, H. S. J. Impact of fabrication technology on flexural resonances of silicon nitride cantilevers. *Microelectronic Engineering* **86**, 1216-1218, doi:10.1016/j.mee.2009.03.113 (2009).
- [42] Kovacs, A., Kovacs, A., Pogany, A. & Mescheder, U. Mechanical investigation of perforated and porous membranes for micro-and nanofilter applications. *Sensors And Actuators B-chemical* **127**, 120-125, doi:10.1016/j.snb.2007.07.044 (2007).
- [43] Kalvesten, E., Smith, L., Tenerz, L. & Stemme, G. The first surface of micromachined pressure sensor for cardiovascular pressure measurements. *Micro Electro Mechanical Systems - IEEE 11th Annual International Workshop Proceedings*, 574-579 (1998).
- [44] Hierold, C., Jungen, A., Stampfer, C. & Helbling, T. Nano electromechanical sensors based on carbon nanotubes. *Sensors And Actuators A-physical* **136**, 51-61, doi:10.1016/j.sna.2007.02.007 (2007).

- [45] Zhang, Y. et al. A Novel Pressure Microsensor With 30- μm -Thick Diaphragm and Meander-Shaped Piezoresistors Partially Distributed on High-Stress Bulk Silicon Region. *IEEE Sensor Journal* **7**, doi: 10.1109/JSEN.2007.910298, 1742-1748 (2007).
- [46] Yang, L., Lai, C., Dai, C. & Chang, P. A Piezoresistive Micro Pressure Sensor Fabricated by Commercial DPDM CMOS Process. *Tamkang Journal of Science Engineering* **8**, doi: 10.6180/jase.2005.8.1.09, 67-73 (2005).

CHAPTER 7

A MEMS FLOW SENSOR USING PERFORATED GRAPHENE MEMBRANE

Qiugu Wang, Yifei Wang and Liang Dong

A paper in preparation

7.1 Abstract

This paper reports on a graphene-based piezoresistive air flow sensor by transferring and patterning a large-area graphene on a suspended silicon nitride thin membrane perforated by a periodic array of micro-through-holes. The patterned graphene sheet flows air at the milliliter-scale and transduces the air flow induced mechanical deformation of graphene into the electrical readout. The present sensor is able to detect the flow velocity in the range of 0–40 m/s with a high sensitivity $\sim 1 \times 10^{-6} (\text{mL}/\text{min})^{-1}$.

7.2 Introduction

The gas flowrate measurement is critical in many industrial and commercial applications, such as environmental monitoring, medical instruments, and process control. Small footprint microelectromechanical systems (MEMS)-based flow sensors outperform the conventional ones in low power consumption, better dynamic performance and cost-effectiveness thanks to the compatibility with integrated circuit technologies. MEMS gas flow sensors are generally classified as either thermal or non-thermal [1, 2]. The non-thermal flow sensors are mainly based on the mechanical working principle such as deflection of cantilevers [3, 4], lift-force [5] and differential pressure [6]. Graphene materials are very suitable for MEMS applications owing to their excellent electrical and mechanical properties and strain induced electrical-mechanical coupling in graphene are widely reported. Sophisticated techniques are already developed to allow large-area uniform growth and transfer of graphene sheets onto various substrates [7, 8]. As a result, the prospect of merging graphene with micromachining technologies opens the path

for developing high sensitivity graphene-based sensors and actuators. At present a few MEMS-based graphene pressure sensors have been demonstrated [9-11]. In our recent work, we demonstrated a graphene-based MEMS pressure sensor with a high sensitivity because of the significantly increased strain induced by the micro-through-holes. It outperforms most existing MEMS pressure sensors using graphene, silicon, and nanotubes as sensitive materials [11]. In this paper, we present a MEMS flow sensor based on the piezoresistive effect of perforated graphene sheet.

7.3 Results and Discussion

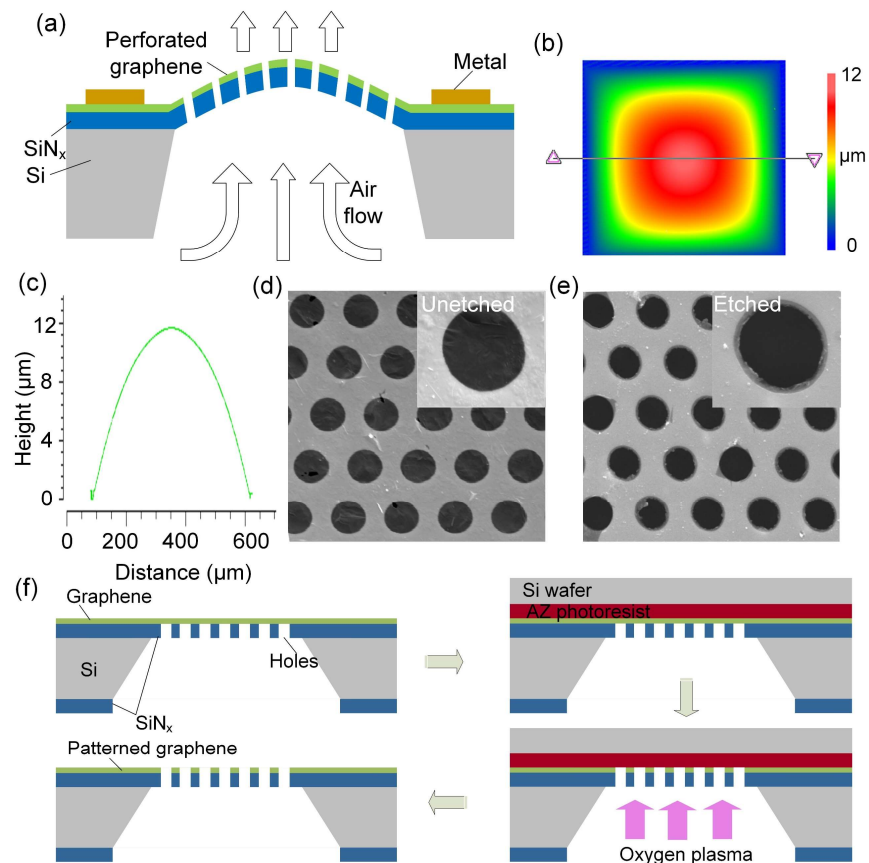


Figure 7.1: (a) Schematic of graphene-based air flow sensor. (b) Surface profiler measurement of the deflection of the membrane at the flow velocity of 35 m/s. The thickness of the membrane is 200 nm and the area is $490 \times 490 \mu\text{m}^2$. (c) Deflection of the membrane at the line marked in (c). (d, e) SEM images before and after oxygen plasma etching. The diameter of holes are 2.5 μm. (f) Fabrication process for patterning graphene sheets.

As illustrated in Fig. 7.1(a), the flow sensor is a few-layered graphene (~ 1 nm) supported by a 200-nm-thick suspended silicon nitride (SiN_x) membrane with perforated micro-through-holes in both layers. Upon the air flow, a pressure drop occurs inside and outside the SiN_x membrane and deflects the membrane. Due to the strain applied on the graphene, the flow rate can be measured from the resistance variations of the deflected graphene using a Wheatstone bridge setup. The surface profiler measurement in Fig. 7.1 (a) and (b) shows that an air volume flow rate of 300 mL/min (i.e., flow velocity of 35 m/s) leads to the 12 μm deflection of the membrane. Fabrication of the graphene flow sensor (Fig. 7.1(f)) starts from a freestanding SiN_x membrane perforated with arrays of microholes covered by a large-area graphene sheet on the top (Fig. 7.1(d)) [11]. To pattern the graphene layer with micro-holes, we use the SiN_x membrane as the shadow mask by adhering topside of the device to a silicon wafer coated with AZ photoresist. After oxygen plasma treatment from the backside of the device, a graphene sheet with perforated micro-holes (Fig. 7.1(e)) is formed.

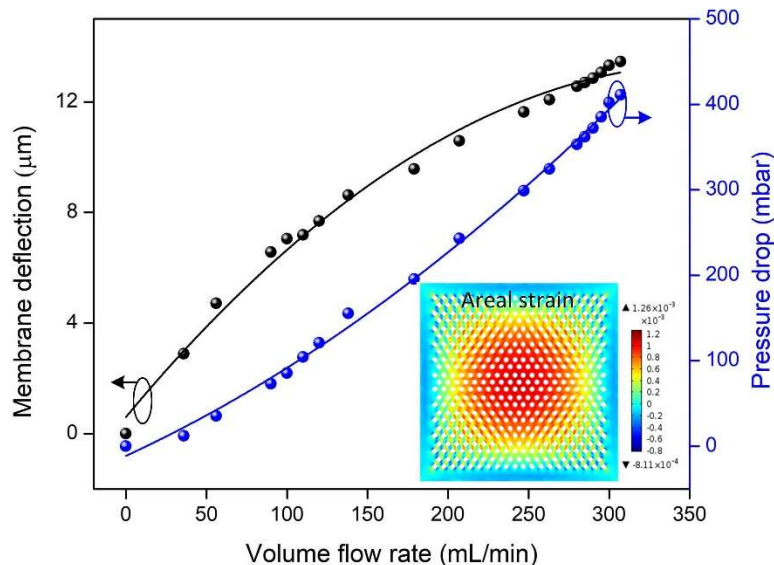


Figure 7.2 Deflection and pressure drop of the membrane as a function of volume flow rate. The black and blue curves are polynomial fitted results. The inset is the simulated areal strain distribution of the membrane under a pressure drop of 400 mbar. The side length of simulated membrane is 200 μm .

We summarize the deflection of the perforated membrane as a function of volume flow rate in Fig.7.2. The membrane deflection approximately follows quadratic growth to the increasing flow rate. To determine the pressure drop across the membrane with air flow, the measured membrane deflection in Fig. 7.2 can be directly converted to pressure drop using the equation in our previous work [11]. For example, at a volume flow rate of 300 mL/min, the membrane deflects 12 μm and causes a pressure drop of 400 mbar. To illustrate the strain distribution of the perforated membrane upon the deflection, mechanical simulations are conducted for a reduced model with side length of 200 μm due to limited computational power. Under 400 mbar differential pressure shown as inset in Fig. 7.2, the membrane had the maximum areal strain of 0.126% at the center of the membrane with the deflection of 3.34 μm .

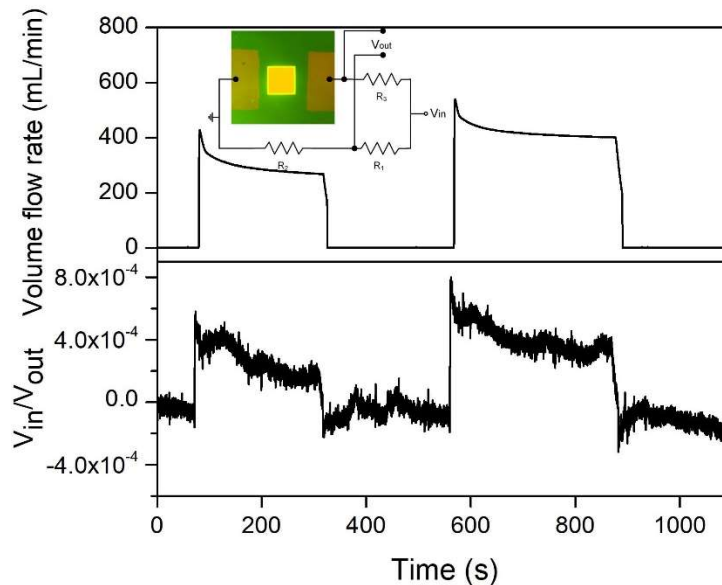


Figure 7.3 Voltage response of the device to different flow rates. The inset shows the optical image of the device and schematic of graphene sensing element connected to the Wheatstone bridge circuit. The central yellowish membrane is the sensing area. $V_{in} = 10\text{ mV}$.

Fig. 7.3 presents the dynamic electrical readout in response to the variations of flow rate. The output voltage rises with increasing rate of air flowing through the perforated membrane. At an increase in step-like volume rate of $\sim 400\text{ mL/min}$, 0.058% relative change is observed for

output voltage. The rapid rise of the output signal indicates an immediate piezoresistive response to air flow through the membrane.

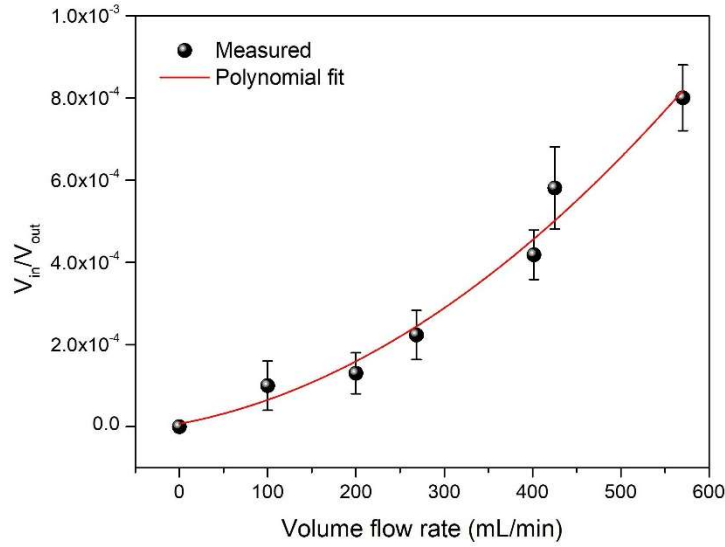


Figure 7.4 The voltage response from the graphene device under different flow velocities, respectively. Back lines are polynomial fitted results.

Fig. 7.4 summarizes the output voltage as a function of the flow rate. Based on the noise floor of the output voltage shown in Fig. 7.2, the noise equivalent pressure resolution of the sensor is 40 mL/min, which can be further improved by optimizing the detection circuit, e. g., using a low-pass filter and a low-noise amplifier. The sensitivity of this piezoresistive flow sensor can be

calculated as $S_v = \frac{\Delta V}{V_{flowrate}} = 1 \times 10^{-6} (mL / min)^{-1}$ or $S_p = \frac{\Delta V}{V P_{drop}} = 3.33 \times 10^{-6} mbar^{-1}$ in terms of the

pressure drop. In contrast to the sensitivity of $2.8 \times 10^{-5} mbar^{-1}$ for our previous pressure sensor with imperforated graphene membrane, the introduction of through-holes in the graphene sheet reduces the sensitivity of the device but are still higher than $2.96 \times 10^{-6} mbar^{-1}$ of the standalone graphene membrane-based sensor [9] and $6.67 \times 10^{-6} mbar^{-1}$ of the sensor using the graphene meander patterns on imperforated SiN_x membrane [10].

Small volume flow rate measurement at $\mu\text{L}/\text{min}$ scale can be realized by fabricating devices with much smaller size and number of through-holes. For the fluid flow through a porous medium with circular holes, volume flow rate (Q) at the given pressure drop (p) can be simplified using the Darcy's law: $Q = \frac{\pi N r_0^4 p}{8 \mu t}$, where N is the number of holes, r_0 is the radius of holes, μ is dynamic viscosity of fluidic medium, t is the thickness of membrane. For example, a freestanding nanohole film with 30×30 arrays of 200-nm-diameter holes has been reported to flow water at the rate of $0.06 \mu\text{L}/\text{min}$.

7.4 Conclusion

In summary, we have developed a small footprint graphene-based MEMS flow sensor. The piezoresistive graphene with perforated micro-holes act as sensing materials to flow air and convert mechanical signals into electrical readout. The present device provides a broad velocity detection range of 0–40 m/s with a sensitivity $\sim 1 \times 10^{-6} (\text{mL}/\text{min})^{-1}$.

7.5 References

- [1] Kuo, J. T. W., Yu, L. & Meng, E. Micromachined Thermal Flow Sensors-A Review. *Micromachines* **3**, 550-573, doi:10.3390/mi3030550 (2012).
- [2] Wang, Y. H. *et al.* MEMS-based gas flow sensors. *Microfluidics and Nanofluidics* **6**, 333-346, doi:10.1007/s10404-008-0383-4 (2009).
- [3] Wang, Y. H., Lee, C. Y. & Chiang, C. M. A MEMS-based air flow sensor with a free-standing micro-cantilever structure. *Sensors* **7**, 2389-2401, doi:10.3390/s7102389 (2007).
- [4] Zhang, Q. *et al.* A self-bended piezoresistive microcantilever flow sensor for low flow rate measurement. *Sensors And Actuators A-physical* **158**, 273-279, doi:10.1016/j.sna.2010.02.002 (2010).

- [5] Svedin, N., Kalvesten, E. & Stemme, G. A new edge-detected lift force flow sensor. *Journal Of Microelectromechanical Systems* **12**, 344-354, doi:10.1109/Jmems.2002.807479 (2003).
- [6] Rajavelu, M., Sivakumar, D., Daniel, R. J. & Sumangala, K. Perforated diaphragms employed piezoresistive MEMS pressure sensor for sensitivity enhancement in gas flow measurement. *Flow Measurement And Instrumentation* **35**, 63-75, doi:10.1016/j.flowmeasinst.2013.12.004 (2014).
- [7] Reina, A. *et al.* Large Area, Few-Layer Graphene Films on Arbitrary Substrates by Chemical Vapor Deposition. *Nano Letters* **9**, 30-35, doi:10.1021/nl801827v (2009).
- [8] Suk, J. W. *et al.* Transfer of CVD-Grown Monolayer Graphene onto Arbitrary Substrates. *Acs Nano* **5**, 6916-6924, doi:10.1021/nn201207c (2011).
- [9] Smith, A. D. *et al.* Electromechanical Piezoresistive Sensing in Suspended Graphene Membranes. *Nano Letters* **13**, 3237-3242, doi:10.1021/nl401352k (2013).
- [10] Zhu, S. E., Ghatkesar, M. K., Zhang, C. & Janssen, G. C. A. M. Graphene based piezoresistive pressure sensor. *Applied Physics Letters* **102**, doi:10.1063/1.4802799 (2013).
- [11] Wang, Q. G., Hong, W. & Dong, L. Graphene "microdrums" on a freestanding perforated thin membrane for high sensitivity MEMS pressure sensors. *Nanoscale* **8**, 7663-7671, doi:10.1039/c5nr09274d (2016).

CHAPTER 8

TAPE-BASED FLEXIBLE METALLIC AND DIELECTRIC NANOPHOTONIC DEVICES
AND METAMATERIALS

A paper published in the 17th International Conference on Nanotechnology (IEEE NANO 2017)

Qiugu Wang, Weikun Han, Yifei Wang, Meng Lu and Liang Dong

8.1 Abstract

This paper describes a multifunctional nanotransfer printing (nTP) method based on a simple stick-and-peel procedure that allows fast production of multiple optical nanodevices using Scotch tape. In addition to the capabilities of forming single- and multi-layer nanopatterned films on a tape, the present technique facilitates the transfer of nanostructures onto unconventional substrates (such as cleaved fiber facets and curved fiber sides) and fabrication of more complex optical devices, including Fabry-Perot cavities. Moreover, our stick-and-peel method can be applicable to various metallic and dielectric structures, including metamaterials with the feature size below 100 nm and TiO₂ nanopatterned films.

8.2 Introduction

Nanotransfer printing (nTP) is a cost-effective and high-throughput technology, which allows manufacturing of large-area nanopatterns [1]. This approach enables the transfer of functional nanopatterned metal or dielectric films from a stamp onto a variety of flexible or stretchable substrates for inexpensive thin-film transistors, integrated circuits, epidermal electronics, surface-enhanced Raman spectroscopy substrates, negative-index three-dimensional (3D) metamaterials, and microelectromechanical devices. Adhesive tapes, often used to exfoliate graphene or MoS₂ monolayers, have also been utilized in many nTP processes as intermediate transfer media or sacrificial layers. Because the adhesion strength of some functional adhesive

materials can be varied using heat [2] or solvents [3], thermal adhesive tapes have been used for transferring nanotube transistors from quartz to plastic substrates, owing to the dramatic decrease in the tape adhesion strength at high temperatures. In addition, the presence of a thin adhesive polymer layer, whose adhesion strength can be controlled by using a plasticizing solvent, can promote high-fidelity replication and on-demand release of Au nanowires onto various supports. Apart from functioning as sacrificial layers, adhesive tapes have also been utilized for planarizing nanopatterned substrates to generate large-area nanogaps [4], and serving as a substrate for the transfer of Al nanohole films from compact discs under a critical temperature [5].

In this work, we present a Scotch tape based nTP process that enables easy transfer of nanopatterned films and cost-effective manufacture of multiple optical nanodevices. Noble metals such as Au and Ag are suitable materials for implementing tape-based nTP process because of the poor adhesion to polydimethylsiloxane (PDMS) or Si. This feature, combined with simple replica nanomolding process using PDMS or Si stamps, makes it possible to build large-area, low-cost and ready-to-use optical devices on flexible tapes.

As illustrated in Fig. 8.1(a), the method of direct tape pasting (stick and peel off) of nanohole films from PDMS stamps forms the basis of other processes. This simple procedure also applies to multi-layer metal-dielectric-metal (MIM) and all-dielectric films as well as metamaterials from Si wafers. In addition, solvents-assisted transfer of Au nanohole films onto optical fibers are presented. In particular, the described taping method also allows fast and more cost-effective generation of advanced optical devices, such as the tape-supported Fabry-Perot (FP) cavities. The resulting tape-supported nanostructures can retain excellent electrical and

optical performance, which can be potentially useful for disposable electronic and optical sensors as well as in ready-to-use microscopic applications.

8.3 Methods

8.3.1 Fabrication of PDMS stamps

During fabrication of PDMS stamps, a soft lithography-based replica molding process [6-8] has been utilized to produce a polymer nanopost array from PDMS elastomer. In this step, a Si template (LightSmyth Technologies Inc., OR, USA) is used as a solid master mold, which is composed of 9 patterns with areas of $8\text{ mm} \times 8\text{ mm}$. The Si mold exhibits the following three pattern types: 1D grating, 2D nanopost arrays, and 2D nanohole arrays. In contrast to the patterns observed for the Si mold, PDMS stamps obtained after replica molding exhibit the inverse structures.

8.3.2 Fabrication of complementary metamaterials

The complementary metamaterial has been fabricated on a SOI wafer. First, the top Si layer of the SOI substrate is thinned down to around 20 nm by thermal oxidation with subsequent wet etching. After that, U-shaped air gaps are patterned on the thinned Si layer surface via e-beam lithography and subsequent reactive-ion etching. The resulting wafer is immersed into a buffered oxide etch solution for 5 min to remove the SiO_2 layer underneath the top Si membrane, while retaining most of the SiO_2 film underneath the frame structure between neighboring c-SRRs. Consequently, the Si c-SRR membrane is suspended above the air cavities. Finally, a 40 nm thick Au film is evaporated onto the device surface to form Au/Si c-SRRs on the top and Au solid SRRs on the bottom of the air wells.

8.3.3 Electron beam evaporation

An electron beam evaporator Temescal (BJD–1800) has been used to deposit single-layer multilayer films with thicknesses of 40 nm onto the stamp surface at an average chamber pressure of around 1×10^{-6} Torr and deposition rate of around 1 Å/s. No additional layers are deposited between the Au and SiO₂ components.

8.3.4 Optical measurements and simulation

Optical spectra of the nanohole arrays on the tape surface or nanodisks embedded into the PDMS layer have been recorded using a spectroscopic measurement setup. The white light emitted from a 150 W quartz halogen lamp is coupled into a multimode fiber collimated by an objective lens and directed onto the sample surface. Reflection spectra of the complementary metamaterials on the tape surface are recorded via Fourier transform infrared spectroscopy (Hyperion 2000, Bruker) under normal incidence of light. Optical simulations have been performed using the finite element method of the COMSOL Multiphysics commercial software [9]. The geometrical parameters used in the simulations are obtained from the SEM images of the studied samples.

8.4 Results and Discussion

8.4.1 Stick-and-peel taping procedure

Fig. 8.1(a) schematically illustrates the taping procedure consisting of sticking and peeling off Au films patterned with nanohole arrays from a PDMS nanostamp. PDMS stamps containing periodic nanowells are generally fabricated from a Si master using a soft lithography-based replica molding process (see the Methods section). After depositing a 40 nm thick Au layer onto a PDMS stamp, quasi-3D plasmonic crystals containing Au nanohole arrays at the top and PDMS-embedded nanodisks are formed. General-purpose transparent pressure-sensitive

adhesive tape (Scotch® Shipping packaging, 3M, MN, USA) is used for peeling off Au nanopatterned films. The tape with a total thickness of 79 μm is composed of 51 μm thick

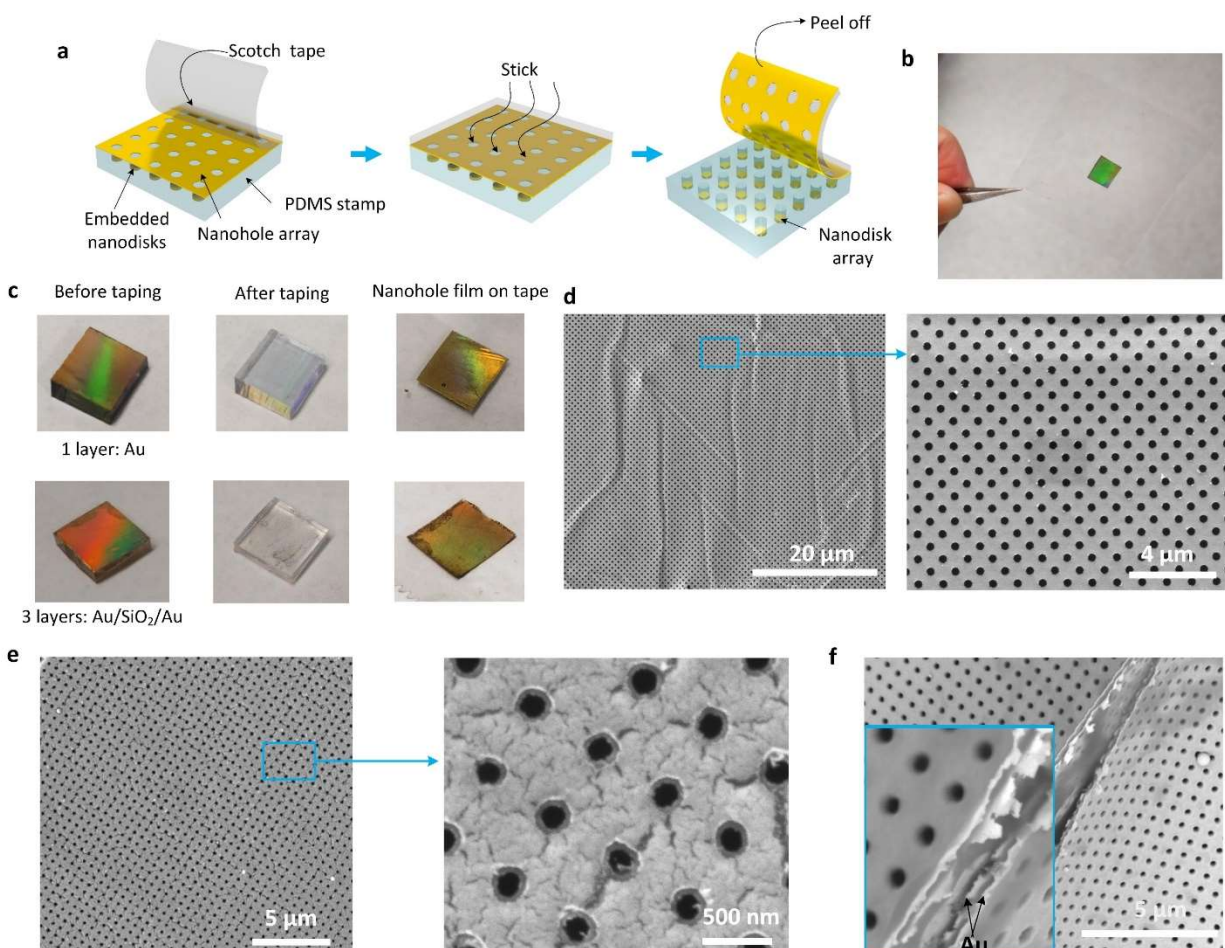


Figure 8.1 Stick-and-peel taping method of producing Au nanopatterned films on the Scotch tape surface. (a) A schematic illustration of the taping procedure utilized for stripping the Au nanohole array from the Au-coated PDMS stamp containing periodic nanowells with depths of 350 nm. (b) A photograph of the stripped Au nanohole array on the tape substrate. The area of the Au film is approximately $8 \times 8 \text{ mm}^2$. (c) Photographs of the 1-layer Au and 3-layer Au/SiO₂/Au films on the PDMS stamp before (left panel) and after (middle panel) taping. The right panel shows the nanohole arrays transferred onto the tape surface. (d) SEM images of the stripped single-layer Au nanohole array on the tape surface. (e) SEM images of the stripped Au/SiO₂/Au films on the tape surface. (f) A cross-sectional view of the 3-layer Au/SiO₂/Au film. The inset shows the magnified cross-sectional image containing the top and bottom Au layers. The nanohole arrays depicted in panels (d)–(f) have a period of 600 nm and are arranged in a square pattern.

biaxially oriented polypropylene backing and 28 μm thick adhesive fabricated from hot-melt rubber resin. At 23 $^{\circ}\text{C}$, a tape piece with dimensions of around $40 \times 40 \text{ mm}^2$ is directly applied to the surface of the Au-coated PDMS stamp and smoothed down with fingertips. Due to the poor adhesion strength between Au and PDMS, the Au nanopatterned films can be easily peeled off from the substrate surface (see inset in Fig. 8.1(a)), while the nanodisks remain embedded into the PDMS bulk. The scanning electron microscopy (SEM) images of the Au nanohole arrays on the tape surface depicted in Fig. 8.1(c) exhibit excellent uniformity over large areas despite the presence of micrometer-scale wrinkles.

To further investigate the ability of the proposed taping method to form multilayers of nanohole arrays, the utilized PDMS stamp has been covered with alternating layers of Au and SiO_2 . In our experiment, a 5-layer film (Au/ SiO_2 /Au/ SiO_2 /Au; 40 nm thick each) is deposited onto the PDMS nanowell arrays without enhancing the adhesion between the Au and SiO_2 layers. As shown in Fig. 8.1(b), the 1-layer and 3-layer films are mostly peeled off from the PDMS substrate. The maximum number of layers that can be peeled off from the tape surface can be determined by the poor bonding strength between the Au and SiO_2 . The 3-layer alternating metal/dielectric film transferred onto the tape surface also exhibits high uniformity, as can be illustrated by Fig. 8.1(d), although its quality is not as good as that of the 1-layer Au film. It should be noted that other types of PDMS stamps as well as 2D periodic nanopost arrays can be used in the taping procedure. However, because the applied mechanical pressure deforms PDMS nanoposts during sticking, some nanodisks are also transferred along with metal films from the bottom of the PDMS stamp to the tape surface.

8.4.2 Solvent-assisted transfer process

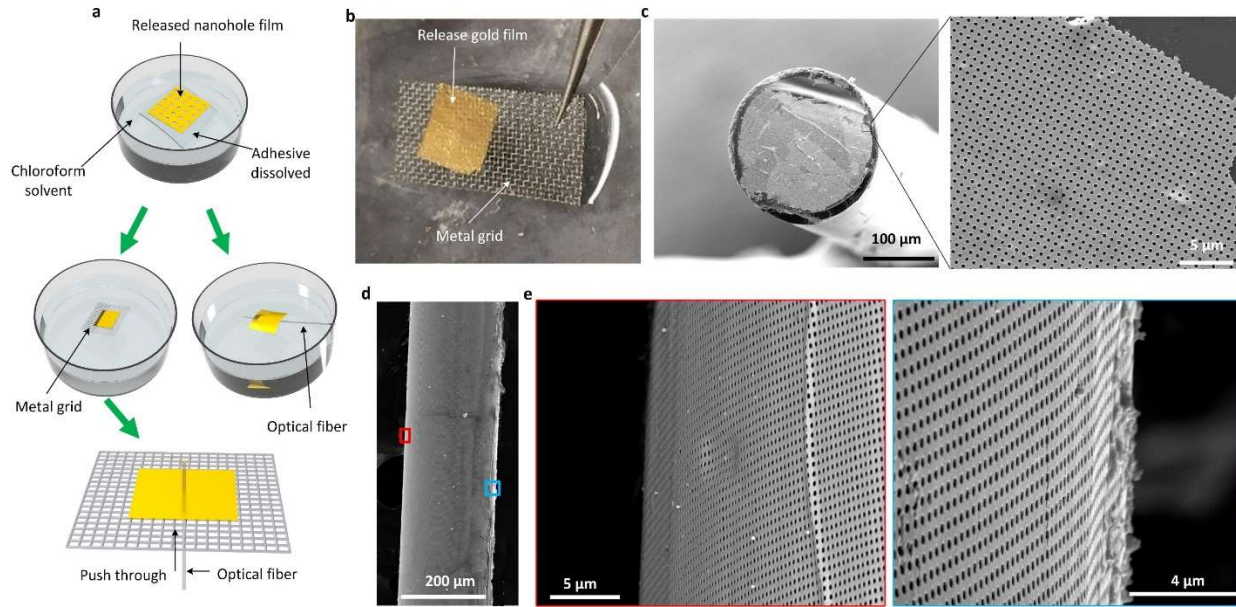


Figure 8.2 Solvent-assisted transfer of Au nanohole arrays from the adhesive tape onto the optical fiber surface. (a) A schematic of the release-and-transfer process of Au nanohole arrays onto the optical fiber surface. Chloroform solution is used to remove adhesives from the tape. The Au nanohole arrays can be transferred onto the fiber tip with a diameter of $210\ \mu\text{m}$ by pushing the fibers through the holes in the metal grid (with dimensions of $500 \times 500\ \mu\text{m}^2$) covered with Au nanohole arrays. Alternatively, the Au nanohole arrays can be directly accommodated by an optical fiber to form a curved nanohole film on its surface. (b) Photographs of the released Au nanohole array and metal grid substrate. (c) SEM images of the Au nanohole array deposited on the fiber facet. (d) SEM images of the curved Au nanohole array on the fiber surface.

One notable advantage of the proposed taping method is that it allows convenient transfer of Au nanopatterned films from the tape surface onto various substrates, which can be realized by wet etching of the tape adhesive with chloroform solvent. In this study, Au nanohole arrays are transferred onto the cleaved facet and curved side of an optical fiber, as schematically illustrated in Fig. 8.2(a). First, the tape containing Au nanohole surface arrays is fully immersed into chloroform until the Au film is completely detached from the tape. The time required for the delamination of the Au film depends on the number of the deposited layers and is equal to 40 s for the single-layer Au film and 2 min for the 3-layer Au/SiO₂/Au film. Afterwards, the suspended Au film is picked by the metal grid with a hole size of $500 \times 500\ \mu\text{m}^2$, as shown in

Fig. 8.2(b). Before the chloroform layer on the metal grid surface completely dries out (in less than 20 s), an optical fiber is directly pushed through the hole covered with the nanopatterned film from the grid downside. As a result, the part of the Au nanopatterned film that is in contact with the fiber tip is transferred onto the fiber surface. Fig. 8.2(c) shows the SEM image of the transferred Au nanohole arrays on the cleaved fiber facet containing a large area of the uniform nanopatterned film.

The majority of the existing patterning techniques directly produce nanopatterns on the fiber facet using lithographical or self-assembly methods, which are expensive or difficult to operate. Nanoskiving [10] is a convenient technique for manually transferring nanopatterns onto the fiber facet using an immersion procedure, the key part of which corresponds to sectioning nanostructures embedded in thin epoxy slabs and is time-consuming. In contrast, the proposed taping method of transferring nanopatterned films is relatively simple and fast. However, while the nanoskiving method uses epoxy slabs for supporting nanostructures, the nanopatterned films fabricated in this work are attached to freestanding metal grids; as a result, the surface tension produced by the chloroform evaporation causes the breakage and stacking of the Au films in some random areas with a yield of around 50%. Thus, the quality of the transferred nanopatterns is slightly lower than that obtained by the nanoskiving method. To reduce surface tension, Au films can be immersed into an ethanol solution immediately after the removal from the chloroform etching solution. Interestingly, after the complete ethanol evaporation, freestanding Au nanohole films with areas of tens of μm^2 supported by the metal grid can be obtained. Another minor problem of the described transfer method is the breakage of fiber edges during pushing through the metal grid holes (Fig. 8.2(c)). Alternatively, the direct lift-up of the Au nanopatterned film supported on the fiber surface enables its attachment to the curved fiber sides.

In contrast to the former process of transferring nanopatterns on the fiber facets (without intermediate attachment to a metal grid), this process allows more uniform formation of nanopatterns on the curved fiber side, as shown in Figs. 8.2(d) and (e).

8.4.3 Electrical and optical characterizations

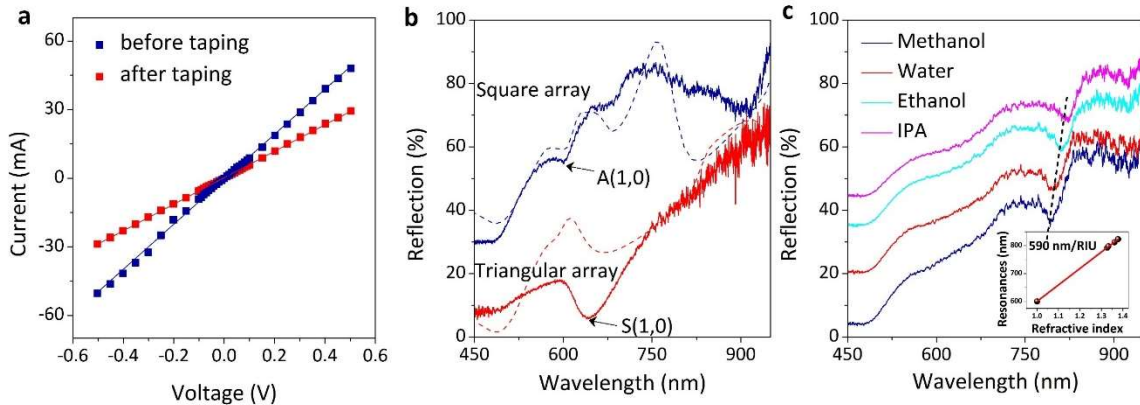


Figure 8.3 Electrical and optical performance of the Au nanohole arrays on the tape surface. (a) I–V curves recorded for the nanopatterned Au film before and after taping. (b) Experimental (solid lines) and simulated (dash lines) reflection spectra obtained for the Au nanohole arrays on the tape surface. Both nanohole arrays have a period of 600 nm and are arranged in square and hexagonal patterns. A(1,0) and S(1,0) denote the (1,0) SPP excitations at the air/Au and tape/Au interfaces, respectively. (c) Bulk refractive index sensitivities measured for the tape-supported square Au nanohole arrays with a period of 600 nm. The inset shows the linear fit of the resonance wavelength plotted as a function of the refractive index.

a) Electrical and refractive index sensitivity measurement

Figs. 8.3(a)–(c) describe the electrical and optical properties of the Au nanohole arrays on the Scotch tape surface. After their transfer, the arrays still exhibit high conductivity with a 40% decrease from 0.1 S to 0.06 S (see Fig. 8.3(a)). Figure 3b shows the experimental and simulated reflection spectra obtained for the tape-supported square and triangular spaced nanohole arrays with periods of 600 nm. The optical resonances of these two arrays correspond to the reflectance dips detected at 600 nm and 637 nm. As indicated by the simulations, the two resonances denoted as A(1,0) and S(1,0) in Fig. 8.3(b) are due to the (1,0) SPP excitations

observed at the air/Au and tape/Au interfaces for the square and triangular spaced nanohole arrays, respectively. The bulk index sensitivity measured for the A(1,0) resonance of the square nanohole array is equal to 590 nm/RIU (see Fig. 8.3(c)), indicating excellent index sensing capabilities of the transferred arrays.

b) Fabry-Perot cavities on the tape surface

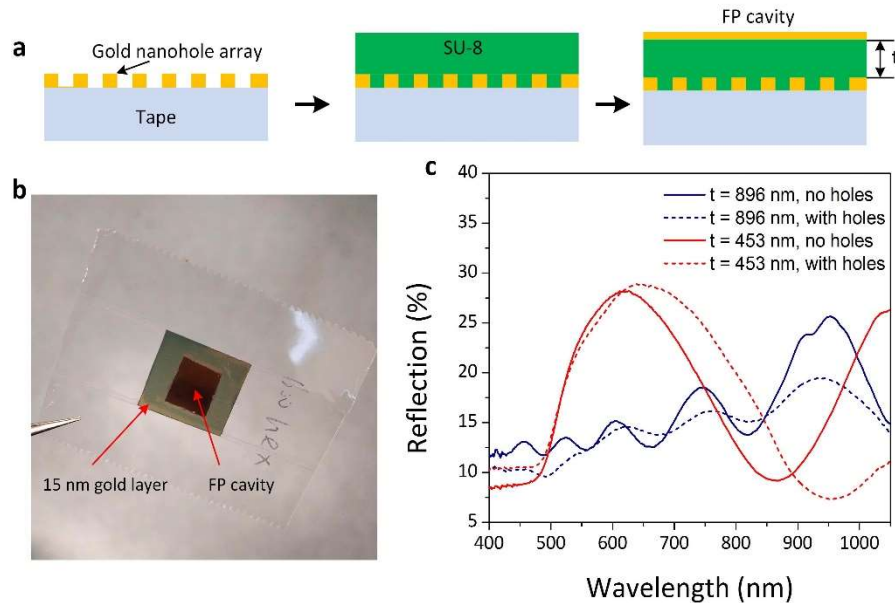


Figure 8.4 Fabry-Perot cavities formed on the tape surface. (a) Fabrication of FP cavities. After transferring Au nanoholes or plain films on the Scotch tape surface, it has been spin-coated with a SU-8 photoresist layer with a thickness t followed by the deposition of a 15 nm thick Au layer. (c) Reflection spectra recorded for the FP cavities on the tape surface with and without nanoholes under normal light incidence. The studied Au nanohole array is arranged into a hexagonal pattern with a period of 600 nm.

In this section, more complex optical structures based on the transferred Au nanohole films such as Fabry-Perot (FP) cavities on the tape surface have been investigated (their fabrication procedure is illustrated in Fig. 8.4(a)). First, a SU-8 photoresist layer with a certain thickness is spin-coated onto the surface of the tape-supported Au nanohole film followed by the deposition of a 15 nm thick Au layer. Figure 4b shows the reflection spectra recorded for the devices with cavity lengths of 896 and 453 nm. For comparison purposes, the devices containing

plain Au films (without nanohole arrays) have been fabricated as well. At a cavity length of 896 nm, the predicted second-order FP mode (which is estimated using the reflection coefficients derived in Ref. [11]) corresponds to a wavelength of 1550 nm, and higher orders of the FP resonance are also observed in the measured wavelength range. However, for the devices with a cavity length of 453 nm, the second-order FP mode is calculated at a wavelength of 850 nm, which agrees well with the observed dip at 860 nm depicted in Fig. 8.4(b). Hence, the devices containing nanohole arrays exhibit optical properties similar to those of the systems without nanohole arrays (with a slight redshift of all FP modes).

8.4.4 Metasurface and dielectric nanohole films on the tap

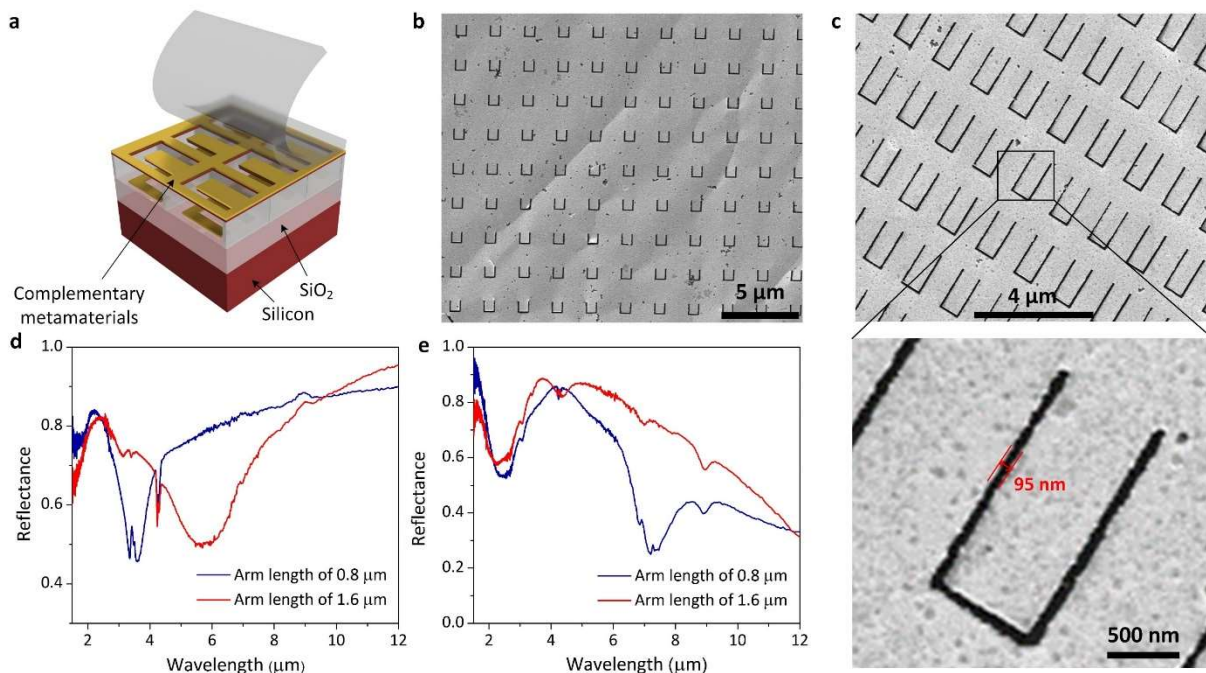


Figure 8.5 Taping method applied to quasi-3D metamaterials and dielectric nanopatterned films. (a) Schematic of a quasi-3D metamaterial. (b, c) SEM images of the tape-supported Au complementary metamaterials. The U-shape of the air apertures of both devices has a width of 500 nm, and 100 nm wide air gaps are arranged in a rectangular pattern. The device depicted in panel (b) possesses an arm length of 800 nm and period of 1.6 μm in both directions, while the device depicted in panel (c) has a 1.6 μm long arm and periods of 1.6 μm and 2.6 μm in two orthogonal directions. (d, e) Reflection spectra recorded for two Au complementary metamaterials.

In addition to peeling off Au films from PDMS stamps, the described taping method can also be applied to stamps made of other materials or dielectric nanopatterned films supported by PDMS stamps. In this work, the following two examples are discussed: quasi-3D metamaterials on silicon-on-insulator (SOI) wafers (Fig. 8.5(a)) and TiO₂ nanohole arrays on PDMS stamps (Fig. 8.5(a)). The utilized quasi-3D metamaterial is composed of an array of Au–Si bilayer complementary split ring resonators (c-SRRs) at the top and an array of Au SRRs at the bottom of the wells with depths of several hundred nanometers formed inside a 1 μm thick SiO₂ layer of the SOI substrate. Each c-SRR unit has an Au–Si nanocantilever surrounded by a U-shaped air gap. After the taping procedure, the top Au c-SRR arrays are transferred onto the tape surface, as shown in Figs. 8.5(b) and (c). The feature size of the air gap of c-SRRs is around 95 nm. The reflection spectra obtained for the c-SRR arrays depicted in Figs. 8.5(d) and (f) exhibit conspicuous resonance dips, which are associated with the excitations of even or odd c-SRR eigenmodes by transverse-magnetic (TM)- or transverse-electric (TE)-polarized fields. For example, under TM polarization, the second order c-SRR excitation mode of the device with an arm length of the U-shape air apertures of 1.6 μm is observed at 6 μm, while the device with a 0.8 μm long arm exhibits the second order c-SRR excitation mode at 3.8 μm. Therefore, this infrared metasurface could be used for sensing of infrared radiation [12].

The TiO₂ nanohole arrays shown in Fig. 8.6(a) exhibit high uniformity, and their transmission spectra contain resonance features depending on the array period. In contrast to peeling off alternating metal and dielectric films, all-dielectric 5-layer TiO₂/SiO₂/TiO₂/SiO₂/TiO₂ films with enhanced bonding strengths between TiO₂ and SiO₂ can be easily removed from PDMS stamps. This stack of alternating index-contrast materials demonstrates clear thin-film

destructive interference at a wavelength of 400 nm (see the transmission spectra depicted in Fig. 8.6(c)), confirming the complete transfer of the 5-layer film onto the tape surface.

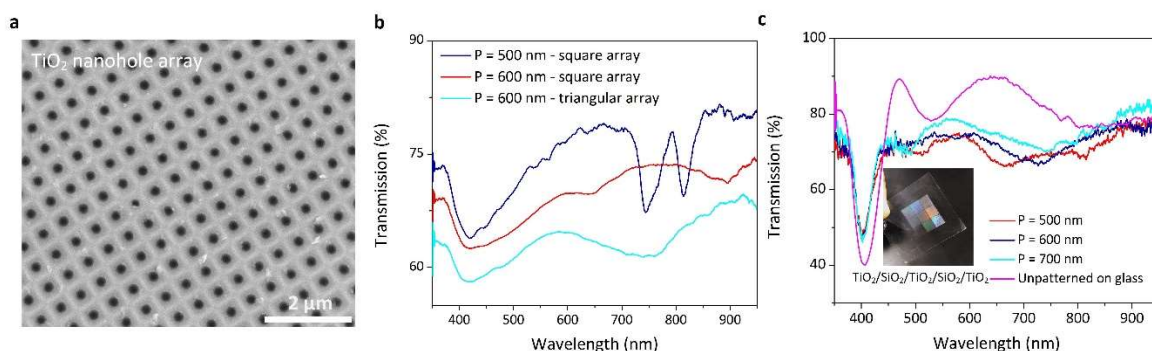


Figure 8.6 (a) An SEM image of the single-layer TiO₂ nanohole array transferred onto the tape surface. (b) Transmission spectra recorded for the TiO₂ nanohole arrays with different periods arranged in square and triangular patterns. (c) Photographs of the 5-layer TiO₂/SiO₂/TiO₂/SiO₂/TiO₂ nanohole film on the tape surface. (d) Transmission spectra recorded for the transferred 5-layer TiO₂/SiO₂/TiO₂/SiO₂/TiO₂ film with different periods and 5-layer film directly deposited on the glass slide. The transmission dip observed at 400 nm clearly indicates thin-film destructive interference.

8.5 Conclusions

In summary, a series of nanotransfer processes utilizing general adhesive tapes have been successfully demonstrated. Using a straightforward stick-and-peel method, both the 3-layer Au/SiO₂/Au and 5-layer TiO₂/SiO₂/TiO₂/SiO₂/TiO₂ nanohole films can be directly transferred from PDMS stamps onto the adhesive tape surfaces. In addition, wet etching of adhesives allows convenient transfer of the nanopatterned films onto unconventional substrates, while the nanoparticle-containing stamps remained after taping quasi-3D materials can also be used as tunable optical devices.

8.6 Acknowledgement

This work was supported by the U.S. National Science Foundation under Grant # ECCS-0954765.

8.7 References

- [1] Carlson, A., Bowen, A. M., Huang, Y. G., Nuzzo, R. G. & Rogers, J. A. Transfer Printing Techniques for Materials Assembly and Micro/Nanodevice Fabrication. *Advanced Materials* **24**, 5284-5318, doi:10.1002/adma.201201386 (2012).
- [2] Lee, C. H., Kim, D. R. & Zheng, X. L. Fabricating nanowire devices on diverse substrates by simple transfer-printing methods. *Proceedings Of The National Academy Of Sciences Of The United States Of Ame* **107**, 9950-9955, doi:10.1073/pnas.0914031107 (2010).
- [3] Jeong, J. W. *et al.* High-resolution nanotransfer printing applicable to diverse surfaces via interface-targeted adhesion switching. *Nature Communications* **5**, doi: 10.1038/ncomms6387 (2014).
- [4] Chen, X. S. *et al.* Atomic layer lithography of wafer-scale nanogap arrays for extreme confinement of electromagnetic waves. *Nature Communications* **4**, doi: 10.1038/ncomms3361 (2013).
- [5] Barrios, C. A. & Canalejas-Tejero, V. Compact discs as versatile cost-effective substrates for releasable nanopatterned aluminium films. *Nanoscale* **7**, 3435-3439, doi:10.1039/c4nr06271j (2015).
- [6] Wang, Q. G., Han, W. K., Liu, P. & Dong, L. Electrically Tunable Quasi-3-D Mushroom Plasmonic Crystal. *Journal Of Lightwave Technology* **34**, 2175-2181, doi:10.1109/Jlt.2016.2526634 (2016).
- [7] Liu, P. *et al.* Tunable meta-atom using liquid metal embedded in stretchable polymer. *Journal Of Applied Physics* **118**, doi: 10.1063/1.4926417 (2015).

- [8] Yang, S. *et al.* From Flexible and Stretchable Meta-Atom to Metamaterial: A Wearable Microwave Meta-Skin with Tunable Frequency Selective and Cloaking Effects. *Scientific Reports* **6**, 21921, doi:10.1038/srep21921 (2016).
- [9] Wang, Q. G. *et al.* Tunable Optical Nanoantennas Incorporating Bowtie Nanoantenna Arrays with Stimuli-Responsive Polymer. *Scientific Reports* **5**, 18567, doi: 10.1038/Srep18567 (2015).
- [10] Lipomi, D. J. *et al.* Patterning the Tips of Optical Fibers with Metallic Nanostructures Using Nanoskiving. *Nano Letters* **11**, 632-636, doi:10.1021/nl103730g (2011).
- [11] Huang, C. P. *et al.* Deep subwavelength Fabry-Perot-like resonances in a sandwiched reflection grating. *Physical Review B* **85**, doi: 10.1103/PhysRevB.85.235410 (2012).
- [12] Dong, L., Yue, R. F., Liu, L. T. & Su, X. Design and fabrication of single-chip a-Si TFT-based uncooled infrared sensors. *Sensors And Actuators A-physical* **116**, 257-263, doi:10.1016/j.sna.2004.04.030 (2004).

CHAPTER 9

CONCLUSIONS AND OUTLOOK

9.1 Conclusions

In this thesis, we introduced the concepts of plasmonics, MEMS technologies, nanotransfer printing fabrications. The importance of acquiring tunability in optical devices and the emerging field of plasmonics and MEMS platform was discussed. We also reviewed recent literature on active media and MEMS-based tunable plasmonics, graphene materials-based MEMS device and non-lithographical nanopattern transfer techniques. Based on these case studies, we have gained insights regarding the cons and pros for each technology and proposed the solutions to make full use of current technologies.

In Chapter 2, we developed a LC-based electrically tunable quasi-3D plasmonic crystal. A low operating electric field is required to align the LC molecules from partially to fully homeotropic state. The experiment and simulation results confirmed the coupled SPP-RA resonance, where its field is predominantly normal to the surface of the plasmonic nanostructure and penetrates into the surrounding LC which making the resonance sensitive to the molecular reorientation of the LC. Possible applications of the device are LC display, sensors and optical signal processing.

In Chapter 3, we developed a temperature-responsive device by coating the plasmonic nanobowtie array with a thin layer of thermo-responsive hydrogel. The wettability of the hydrogels is varied under different temperature and thus changes the water content of hydrogel, resulting in the refractive index changes of hydrogel. We found that the hydrogels-coated BNAs, a 16.2 nm of resonance shift was observed with a temperature increase of 15 °C, compared to a 3 nm shift for the uncoated bare BNAs, due to the large field enhancement of the plasmonic modes

confined in the gaps of the BNAs. Our study suggests the possibility of making environmental-sensitive optical sensing devices via combining the plasmonic nanostructures and environmental-responsive materials.

In Chapter 4, we developed an easy-to-implement and compact NEMS-enabled tunable IR metamaterials operating by electrostatically actuating the nanocantilevers embedded in the c-SRR units. The present device can provide fast electro-optic modulation at frequencies of several tens of MHz. Possible applications of the device include optical modulators, infrared sensors, and transformation optics.

In Chapter 5, based on the same process flow introduced in Chapter 4, we further developed a NEMS thermo-mechanically tunable IR metamaterial by actuating the biomaterial asymmetric SRR structures. By increasing the temperature, the difference in thermal expansion coefficient of the two materials results in the deflection of slimmer arms of SRRs and modulate the optical properties of the metamaterials. The device provides up to 90% optical signal modulation at a wavelength of 3.6 μm .

In Chapter 6, we developed a graphene-based small footprint MEMS pressure sensor formed by transferring large area CVD-grown graphene onto a suspended SiN_x membrane perforated by an array of through-holes. The measured sensitivity provides high sensitivity that outperforms many other existing graphene based counterpart sensors.

In Chapter 7, based on the high sensitivity graphene MEMS pressure sensor in Chapter 6, we developed a flow sensor by selectively etching the graphene suspended over the holes region to allow air flow through. The present sensor is able to detect the high velocity in the range of 0–40 m/s with a high sensitivity $\sim 0.039 \mu\text{V}/(\text{mL}/\text{min})$.

In Chapter 8, we developed a nanotransfer process utilizing general adhesive tapes. Using a straightforward stick-and-peel method, metallic and dielectric photonic devices and metamaterials were transferred onto the tape while retaining their excellent optical properties. The ability of further transferring onto other unconventional substrates such as optical fibers were also demonstrated. Possible applications of present techniques include wearable electronic and optical sensors.

9.2 Outlook

The general future aspects of tunable plasmonic devices include the search of appropriate applications for each developed tuning method, improving the sensitivity of the devices and integrating NMES-based device with IC technologies. For LC-based electrically tunable device, further improvement can be made towards a high-contrast switching performance with a low power consumption. For hydrogel-based tunable device, future work can emphasize on the application aspect by developing a variety of sensing devices, such as biosensors and chemical sensors. For NEMS-based tunable devices, improvements include the optimization of the structural design to achieve better sensitivity at a low operating voltage or low temperature, the design of new actuating method to further shrink working wavelength.

For the graphene-based MEMS pressure sensor, future work includes packaging with IC wire bonding techniques to stabilize the signal detection, optimizing fabrication processes to reduce number of pinholes in graphene, and improving an electronic readout circuit to reduce the noise level. For the graphene-base flow sensor, aside from the aspects mentioned in pressure sensors, future work includes the μL scale volumetric gas flow by further reducing the diameter or the number of holes. Future tape-based nTP process can focus on applications in wearable and flexible nanophotonic devices for biochemical sensors.

APPENDIX LIST OF PEER REVIEWED JOURNALS

- [1] Liu, P., Yang, S. M., Jain, A., Wang, Q. G., Jiang, H. W., Song, J. M., Koschny, T., Soukoulis, C. M. & Dong, L. Tunable meta-atom using liquid metal embedded in stretchable polymer. *Journal Of Applied Physics* **118**, doi: 01450410.1063/1.4926417 (2015).
- [2] Wang, Q. G., Liu, L. J., Wang, Y. F., Liu, P., Jiang, H. W., Xu, Z., Ma, Z., Oren, S., Chow, E. K. C., Lu, M. & Dong, L. Tunable Optical Nanoantennas Incorporating Bowtie Nanoantenna Arrays with Stimuli-Responsive Polymer. *Scientific Reports* **5**, 18567, doi: 1856710.1038/Srep18567 (2015).
- [3] Wang, Q. G., Han, W. K., Liu, P. & Dong, L. Electrically Tunable Quasi-3-D Mushroom Plasmonic Crystal. *Journal Of Lightwave Technology* **34**, 2175-2181, doi:10.1109/Jlt.2016.2526634 (2016).
- [4] Wang, Y. F., Liu, L. J., Wang, Q. G., Han, W. K., Lu, M. & Dong, L. Strain-tunable plasmonic crystal using elevated nanodisks with polarization-dependent characteristics. *Applied Physics Letters* **108**, doi:07111010.1063/1.4942454 (2016).
- [5] Ali, M. A., Hong, W., Oren, S., Wang, Q. G., Wang, Y. F., Jiang, H. W. & Dong, L. Tunable bioelectrodes with wrinkled-ridged graphene oxide surfaces for electrochemical nitrate sensors. *Rsc Advances* **6**, 67184-67195, doi:10.1039/c6ra09621b (2016).
- [6] Wang, Q. G., Hong, W. & Dong, L. Graphene "microdrums" on a freestanding perforated thin membrane for high sensitivity MEMS pressure sensors. *Nanoscale* **8**, 7663-7671, doi:10.1039/c5nr09274d (2016).

- [7] Yang, S. M., Liu, P., Yang, M. D., Wang, Q. G., Song, J. M. & Dong, L. From Flexible and Stretchable Meta-Atom to Metamaterial: A Wearable Microwave Meta-Skin with Tunable Frequency Selective and Cloaking Effects. *Scientific Reports* **6**, 21921, doi:10.1038/srep21921 (2016).
- [8] Wang, Q. G., Mao, D. P., Liu, P., Koschny, T., Soukoulis, C. M. & Dong, L. NEMS-based infrared metamaterial via tuning nanocantilevers within complementary split ring resonators. *Journal of Microelectromechanical Systems*, doi: 10.1109/JMEMS.2017.2746688 (in press)
- [9] Wang, Q. G., Mao, D. P. & Dong, L. Thermomechanically tunable infrared metamaterials using asymmetric split-ring resonators. *Journal of Microelectromechanical Systems*, doi: 10.1109/JMEMS.2017.2764054 (in press)